

caesar



center of advanced
european studies
and research

Systematic evaluation of techniques for the study of the supramolecular architecture of rhodopsin

Inaugural-Dissertation

Zur

Erlangung des Doktorgrades

der

MATHEMATISCH-NATURWISSENSCHAFTLICHE FAKULTÄT

der

UNIVERSITÄT ZU KÖLN

vorgelegt von

Anne Viktoria Schulze

aus Berlin



Berichterstatter: Prof. Dr. E. Behrmann
Prof. Dr. U. Baumann
weiterer Gutachter Prof. Dr. U. B. Kaupp

Abstract

The eye is outstanding in its sensitivity: it can react to single photons due to the rod photoreceptor, in particular its outer segment. This thesis investigates experimental approaches to study the higher-order structure of the outer segment's crucial constituent: rhodopsin. The oligomeric state and organization of rhodopsin within disk membranes has been discussed intensively due to its fundamental meaning. The method of choice to analyze rhodopsin in its close-to-native state so far has been cryo-electron microscopy of vitreous sections (CEMOVIS). To analyze one illumination state of rhodopsin (dark state), CEMOVIS was sufficient. However, CEMOVIS has the disadvantage to be time-consuming and error-prone. To analyze different illumination states, CEMOVIS is not efficient enough. The main part of this thesis treats alternative techniques to overcome the disadvantages of CEMOVIS. Additionally, studies of rhodopsin's temporal bleaching behaviour were carried out.

In more detail: First, we aim to analyze the bleaching of intact retinas. This was done quantitatively via UV-VIS-spectroscopy. We could see an exponential bleaching within the short time scale (in the range of ms). Second, alternative techniques to substitute CEMOVIS were considered and their applicability investigated and evaluated. Dual-axis tomography for tomogram acquisition of samples produced via CEMOVIS turned out to be suboptimal. A ROS solubilization prior to cryo-fixation was accompanied by the same disadvantages like CEMOVIS of high-pressure-frozen retinas. The retinal misplacement and thereby the oblique fractioning of ROS during freeze-fracture experiments with retinal cryo-samples impeded direct imaging of exposed ROS disk membranes. Samples for cryo-ET can also be produced with the focused-ion beam (FIB). Tomography is sped up by using the Fib, due to superior sample quality. However, this way to produce samples is again suboptimal and time-consuming at the present. The most promising approach was to reduce dimensionality of the sample via isolation of ROS disks. ROS disks can subsequently be used for vitrification (plunge-freezing) and subsequent cryo-

ET or analyzed via atomic force microscopy (AFM). AFM however, does not allow the investigation of close-to-native state samples. Nevertheless, it has the advantage of being a technique with a greater effectiveness – what we aimed for. A future optimization of this technique will allow for further investigations of, for example, rhodopsin's supramolecular structure upon illumination. Finally, a tomogram was simulated and compared to real data.

Zusammenfassung

Die Sensitivität des Auges ist einmalig: dank der Stäbchen, insbesondere ihrer Außensegmente, kann es bereits auf einzelne Photonen reagieren. Diese Arbeit befasst sich mit verschiedenen Methoden, um die Organisation des wichtigsten Bestandteils des Außensegmentes zu untersuchen: dem Rhodopsin. Die Frage nach der Oligomerisierung und Organisation von Rhodopsin wurde aufgrund seiner grundlegenden Bedeutung weithin untersucht und diskutiert. Kryoelektronenmikroskopie von Gefrierschnitten (CEMOVIS) ist die Methode der Wahl, um Rhodopsin in seinem nativen Zustand zu untersuchen. Für die Untersuchung eines Belichtungszustandes von Rhodopsin war CEMOVIS geeignet. Doch hat CEMOVIS den Nachteil, zeitaufwendig und fehleranfällig zu sein. Um verschiedene Belichtungszustände zu untersuchen, war CEMOVIS aufgrund der geringen Effektivität nicht geeignet. Der Hauptteil dieser Doktorarbeit befasst sich mit alternativen Techniken, um die Nachteile von CEMOVIS zu überwinden. Zusätzlich wurde das zeitliche Verhalten von Rhodopsin beim Bleichen durch Lichteinwirkung untersucht. Im Detail: Als Erstes wurde das Bleichen der intakten Retina untersucht. Dies wurde quantitativ mittels UV-VIS-Spektroskopie gelöst. Für kurze Belichtungszeiten (im ms-Bereich) zeigte sich ein exponentielles Bleichen von Rhodopsin. Als Nächstes wurden alternative Techniken als Ersatz für CEMOVIS hinsichtlich ihrer Machbarkeit betrachtet und bewertet. Die Tomographie über zwei Achsen von CEMOVIS-Proben stellte sich

als unpraktikabel heraus. Wenn die Außensegmente vor der Kryofixierung isoliert wurden, brachte dies die gleichen Nachteile wie CEMOVIS mit kryofixierten Retinas mit sich. Während der Gefrierbruch-Experimente zeigte sich, dass die Retinen nicht eben liegend eingefroren waren. Dadurch waren die Membransäckchen der Außensegmente durch die schiefen Gefrierbrüche nicht analysierbar. Proben für die Tomographie lassen sich auch über die Ionenfeinstrahlanlage herstellen. Die Tomographie beschleunigt sich dadurch, weil die Probenqualität höher ist. Auch die Etablierung dieser Methode zeigte schwerwiegende zeitliche Nachteile auf. Vielversprechend war der Ansatz, die Dimensionalität der Probe durch Isolation der Außensegmente und anschließend der enthaltenen Membransäckchen zu reduzieren. Diese lassen sich kryofixieren und tomographieren oder über ein Rasterkraftmikroskop analysieren. Dies lässt sich jedoch nicht mit dem nativen Zustand der Probe vereinbaren. Dennoch bringt das Rasterkraftmikroskop den Vorteil einer höheren Effektivität mit sich – das Ziel der Arbeit. Eine zukünftige Optimierung der Technik kann weitere Untersuchungen ermöglichen, z.B. die supramolekulare Struktur von Rhodopsin unter Belichtung. Schließlich wurde ein Tomogram simuliert und mit den aufgenommenen Realdaten verglichen.

Contents

1. Introduction and theoretical background	1
1.1. G protein-coupled receptors	1
1.2. Rhodopsin, signaling, and the visual cycle	3
1.2.1. Disk membranes within the rod outer segment	3
1.2.2. Rhodopsin signaling	4
1.2.3. The visual cycle and spectroscopic measurements	5
1.3. Rhodopsin and the question of its oligomeric state	8
1.3.1. Biochemical studies	8
1.3.2. Spectroscopic measurements	13
1.3.3. Biophysical studies	15
1.3.4. Collision coupling vs. precoupling	20
1.3.5. Rhodopsin is organized as double-rows of dimers	24
1.4. Aim of the thesis	28
2. Materials and Methods	31
2.1. Materials	31
2.2. Software	33
2.3. Mice	33
2.4. Experimental overview	35
2.5. Retina dissection	36

2.6. Solubilization of rhodopsin	38
2.6.1. SDS-PAGE and Western Blot	40
2.6.2. Different detergents tested	42
2.6.3. Illumination quantification achievable with high-power LED	42
2.6.4. Optical measurement of solubilized rhodopsin	44
2.6.5. Analysis of rhodopsin spectra	45
2.7. Isolation of rod photoreceptors and outer segments	45
2.8. Isolation of ROS disk membranes	46
2.9. Cryo-fixation	48
2.9.1. High-pressure freezing	49
2.9.2. Plunge-freezing	51
2.10. Cryo-sectioning and processing of the grids	53
2.11. Cryo-electron microscopy and tomography	55
2.11.1. Transmission electron microscope	57
2.11.2. Dual-axis tomography	59
2.12. Data-processing	59
2.13. Simulation of ROS volume	62
2.14. Freeze-fracture and scanning-electron microscopy	64
2.15. Focused-ion beam	66
2.16. AFM on isolated ROS disk membranes	68
3. Results	71
3.1. Investigation of the bleaching behaviour of rhodopsin	71
3.1.1. Preliminary experiments	71
3.1.2. Quantification of the bleaching of Rh within the intact retina	74
3.2. Cryo-electron microscopy of vitreous sections (CEMOVIS)	78
3.2.1. Cryo ultramicrotomy	78
3.2.2. Single-axis cryo electron tomography	79

3.2.3. Dual-axis electron tomography	82
3.2.4. Cryo electron tomography of isolated ROS	85
3.3. Alternative approaches for investigation of rhodopsin's higher-order structure	86
3.3.1. Freeze fracture	86
3.3.2. Production of TEM specimens using FIB	87
3.3.3. Influence of HPF carrier surface morphology on sample quality .	89
3.3.4. Atomic-force microscopy	91
3.4. Simulation of a cryo electron tomogram	92
4. Discussion	95
4.1. Rhodopsin's bleaching behaviour - a prerequisite to analyze illuminated retinas	95
4.2. CEMOVIS is less effective and error-prone	98
4.3. Using ROS solutions reduces dimensionality	100
4.4. Freeze-fracture experiments were stopped due to misorientation of ROS	100
4.5. Impact of ROS sample concentration on FIB-assisted thinning	101
4.6. Pattern on disk surface detected by AFM	102
4.7. Tackling the problem of artifacts: possible approaches	103
4.7.1. Do we reach the technical limit?	104
4.8. What happens with rhodopsin's higher-order structure upon illumination?	106
4.9. Alternative techniques - worth to be performed	109
4.9.1. Localization of transducin bound to dark-state rhodopsin	109
4.9.2. Light microscopy as an upcoming alternative technique	110
4.10. Outlook	111
Bibliography	117
A. Danksagung	133

B. Eidesstattliche Erklärung	135
C. Curriculum Vitae	137

List of Abbreviations

AFM	Atomic force microscope
AO-OCD	Adaptive Optics Optical Coherence Tomography
β AR	β -Adrenergic receptor
CCD	Charge Coupled Device
CEMOVIS	Cryo electron microscopy of vitrified sections
CHO	Chinese hamster ovary (cells)
cGMP	cyclic-guanosine monophosphate
CLEM	Correlative Light Electron Microscopy
CMOS	Complementary metal-oxide-semiconductor
CNG	Cyclic nucleotide-gated (channel)
Da	Dalton (atomic mass unit, $1u = 1Da$)
DDM	n-Dodecyl β -D-maltopyranoside
DHA	Docosahexaenoic acid
dk	donkey
DQE	Detective quantum efficiency
DSC	Differential scanning calorimetry

e^-	Electron
ECL	Electrochemical luminescence
EELS	Electron energy-loss spectroscopy
e.g.	exempli gratia
EHT	Electron high tension
EM	Electron microscope
EPR	Electron spin resonance spectroscopy
FD-AFM	Force-distance curve-based AFM
FDA	Food and Drug Administration
FF	Freeze-fracture
FIB	Focused ion beam
GARP2	Glutamic acid- rich protein 2
GDP	Guanosine diphosphate
GIF	Gatan imaging filter
GIS	Gallium ion source
GRK	G-protein coupled receptor kinase
GTP	Guanosine triphosphate
h	hours
Hb	Hemoglobin
HDM	n-Hexadecyl- β -D-maltoside
HEPES	2-[4-(2-Hydroxyethyl)piperazin-1-yl] ethansulfonic acid

HPF	H igh- p ressure f reezing
$h\nu$	Photon energy
i.e.	i d e st
kDa	k ilo D alton
KO	K nock- o ut
λ	Wavelength
LED	L ight e mitting d iode
M	M arker
MI	M etarhodopsin I
MII	M etarhodopsin II
MIII	M etarhodopsin III
min	m inute
mPIC	m ammalian P rotease I nhibitor C ocktail
ms	m illisecond
PBS	P hosphate- b uffered s aline
PBST	P hosphate- b uffered s aline with t ween
PC	P hosphatidyl c holine
PDB	P rotein d ata b ase
PDE	P hosphodiesterase
PIE-FCCS	P ulsed- i nterleaved e xcitation f luorescence c ross- c orrelation s pectroscopy
px	P ixel

rb	rabbit
Ret. sp.	Retinaldehyde species
Rh	Rhodopsin
RIS	Rod inner segment
ROI	Region of interest
ROS	Rod outer segments
RPE	Retinal pigment epithelium
rpm	rotations per minute
s	second
SDS-PAGE	Sodium decyl sulphate-polyacrylamide gel electrophoresis
SEB	Scanning electron microscope beam
SEM	Scanning electron microscope
Σ	Sum
SNR	Signal-to-noise ratio
TDM	n-Tetradecyl- β -D-maltoside
TEM	Transmission electron microscope
TM	Transmembrane
TMV	Tobacco mosaic virus
UV	Ultraviolet
vs.	versus
WD	working distance

WT **Wild type**

z.B. **zum Beispiel**

1. Introduction and theoretical background

This chapter serves as an introduction to the field of rhodopsin research and will give you the background necessary for the consideration of the upcoming experiments. The chapter is divided as follows. First, an introduction into the G protein-coupled receptors (GPCRs) is given. Common properties are discussed as well as differences of the distinct GPCR members. Afterwards, we will focus on rod outer segments and rhodopsin itself (section 1.2). In section 1.3 previous biochemical (subsection 1.3.1), spectroscopic (subsection 1.3.2), or biophysical (subsection 1.3.3) studies to rhodopsin's functional unit or oligomeric state are referred to. Section 1.3 is of very high importance to the subject of this thesis - it discusses the presence of higher-order structures of rhodopsin within the disk membranes of rod outer segments (ROS). Section 1.4 concludes this chapter by giving the aim of the studies that are the subject of this thesis.

1.1. G protein-coupled receptors

Rhodopsin is the best studied and founding member of the rhodopsin family (class A) of G protein-coupled receptors (GPCRs) (Fredriksson et al., 2003). GPCRs represent the largest family of receptors and are involved in many different signaling cascades. GPCRs are also the targets of many drugs – another indication of its importance. Understanding the basic principles of GPCR signaling leads to drug improvement and is, therefore, of pharmacological interest. Consequences for drug development may ensue our basic research. In fact also structural and functional details leads to drug development (Yang

et al., 2021). In fact, Yang et al. (2021) report that for GPCRs drug design is more based on knowledge instead of random ligand screening, nowadays. They summarized that 527 Food and drug administration (FDA)-approved drugs target 165 GPCRs within various indications - ranging from hypotension, through migraine to malignancies. According to the authors, this population is becoming more and more due to further progresses in research. GPCRs are membrane proteins and share the basic structure of seven transmembrane α -helices with three extracellular and at least three intracellular loops (Palczewski et al., 2000). An amphiphilic, eighth helix is located at the cytosolic face of the receptor and may facilitate interactions with heterotrimeric GTP-binding proteins (G proteins) like transducin (Palczewski et al., 2000). The N-terminus is located on the extracellular and the C-terminus on the intracellular side.

Among the class A GPCRs, but also among other GPCR classes, are several orphan receptors, for which no ligand has been identified, yet. During the past years, constant attempts to identify ligands of orphan GPCRs lead to their partial deorphanization (Davenport et al., 2013). Cheminformatics approaches may help ligand identification for orphan drugs or drug development for all GPCRs (Basith et al., 2018). Nanobodies may also help studying GPCRs (Daibani and Che, 2021). According to Daibani and Che (2021) they can act as chaperones to ease receptor crystallization or biosensors to identify receptors or to monitor their activation within immunohistochemistry analyses. The research of GPCRs is going deeper and deeper and the basic research of rhodopsin is a part of it. Owing to the high similarity among GPCRs, mechanistic and structural studies using rhodopsin are likely to extend our knowledge about other GPCRs in general, as well. Insights from research on rhodopsin may bring other projects forward due to structural similarities to other GPCRs in general or other opsins in special. This also applies for implications on the mechanism of signaling resulting from any structural organization of rhodopsin.

1.2. Rhodopsin, signaling, and the visual cycle

1.2.1. Disk membranes within the rod outer segment

This section is concerned with the structure of a rod outer segment (ROS), which harbours the rhodopsin molecules. In the course of the section, also the downstream signaling of rhodopsin comes into view. The ROS consists of a stack of about a thousand disks. The rhodopsin molecules are located in these disk membranes. Each disk has an infolding (incisure), which is oriented similarly over hundreds of disks. Disks are anchored to the plasma membrane via the disk rim regions. Cytoplasmic filaments between disks and between cell membrane and disks may contribute to the stacking of disks (Gilliam et al., 2012).

Within their micrographs, Gilliam et al. found some densities between the disks of the rod outer segment, which have not been reported before. These inter-disk densities were located in the middle between two neighbouring disks. Because of this spacing of 7.81 nm, Gilliam et al. speculate that these inter-disk densities are composed of microtubules (tubulin dimer repeat within the microtubule is 8 nm) and that they are responsible for regulating the disk spacing in the outer segment (Gilliam et al., 2012). Pöge et al. (2021) used the same technique, however came to slightly different results. Even Pöge et al. (2021) found connectors, which has been unknown so far. These connectors connect adjacent disks and seem to have an important role for the arrangement of disks during ROS morphogenesis (Pöge et al., 2021). Pöge et al. distinguishes between connectors at the disk rim region and connectors between disks, which are outside the disk rim region (interior connectors). Different from Gilliam et al., Pöge et al. speculate that these connectors are not tubulin molecules, but glutamic acid-rich protein 2 (GARP2; at the disk rim) or phosphodiesterase 6 (PDE6) molecules (interior connector). Furthermore, the distances Pöge et al. (2021) found are also slightly different,

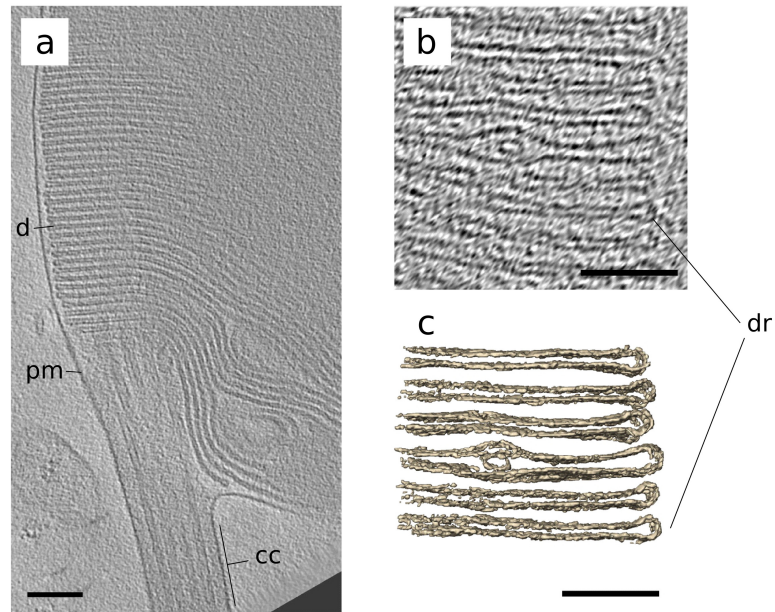


Figure 1.1.: Inter-disk densities visible between neighbouring disks within the ROS (adapted from Gilliam et al. (2012))

a) Cryo-Electron micrograph of the base of ROS showing the stack of disks and the connecting cilium (scale bar = 0.2 μm). b) Tomogram of a ROS disk stack in detail (scale bar = 0.1 μm). Gilliam et al. (2012) used disks from the tomogram to measure the diffraction pattern and the Fourier transform was calculated to have a measure for all the contained distances. Comparing different samples, Gilliam et al. found the following parameters: The thickness of the disk membrane (bilayer) is 5.01 nm. Distance to inter-disk densities was measured to be 7.81 nm. Intradiscal space is 6.36 nm. Neighbouring disks are separated by 15.56 nm. c) Segmented disks of the tomogram in (b) (scale bar = 0.1 μm).

cc: connecting cilium; d: disk; dr: disk rim; pm: plasma membrane

but in the same range. The bilayer was measured to be 7 nm. The intradiscal space was 4 nm. Neighbouring disks were separated by 14 nm (interior) or 8 nm at the disk rim.

1.2.2. Rhodopsin signaling

Upon illumination, 11-*cis*-retinal, the chromophore of rhodopsin, isomerizes to all-*trans*-retinal (Pugh and Lamb, 2000). This photoisomerization causes extensive structural rearrangements inside rhodopsin via several intermediates, leading to the release of

the chromophore. The rhodopsin intermediate, which is able to activate transducin, the G protein in retinal rods, is metarhodopsin II. Activation of transducin leads to the dissociation of the GTP-bound G_{α} subunit, which in turn modulates the activity of the downstream effector molecule, the cyclic GMP-hydrolysing phosphodiesterase (PDE) (Pugh and Lamb, 2000). The ensuing decrease of the cGMP concentration leads to the closure of cyclic nucleotide-gated (CNG) channels in ROS, Ca^{2+} - and Na^{+} - influx stops. Because K^{+} efflux is still ongoing, through channels in the rod inner segment (RIS) – another component of the rod cell – the rod hyperpolarizes. The electrical signal is subsequently processed, enhanced, and transmitted to the brain.

1.2.3. The visual cycle and spectroscopic measurements

In the following, we will discuss why spectroscopic measurements are convenient to address rhodopsin's motility and organization. Also, the prerequisites for such measurements are discussed.

A study of the retina exposed to low illumination levels, as it is part of this work, is of high interest for the analysis of any putative organization of rhodopsin. The question arises, whether any organization of rhodopsin may change or fall apart upon illumination. To get to know what low levels of light for the intact retina means, the bleaching of rhodopsin first had to be quantified (see also section 1.4 and chapters 2.5 and 2.6). Nothing but spectroscopic measurements could be more convenient to analyse the bleaching of rhodopsin. Rhodopsin has its absorbance maximum at 500 nm. Fig. 1.2 shows the visual cycle as adapted from Ernst et al. (2014). Only the – for this study – most important intermediates and products are displayed.

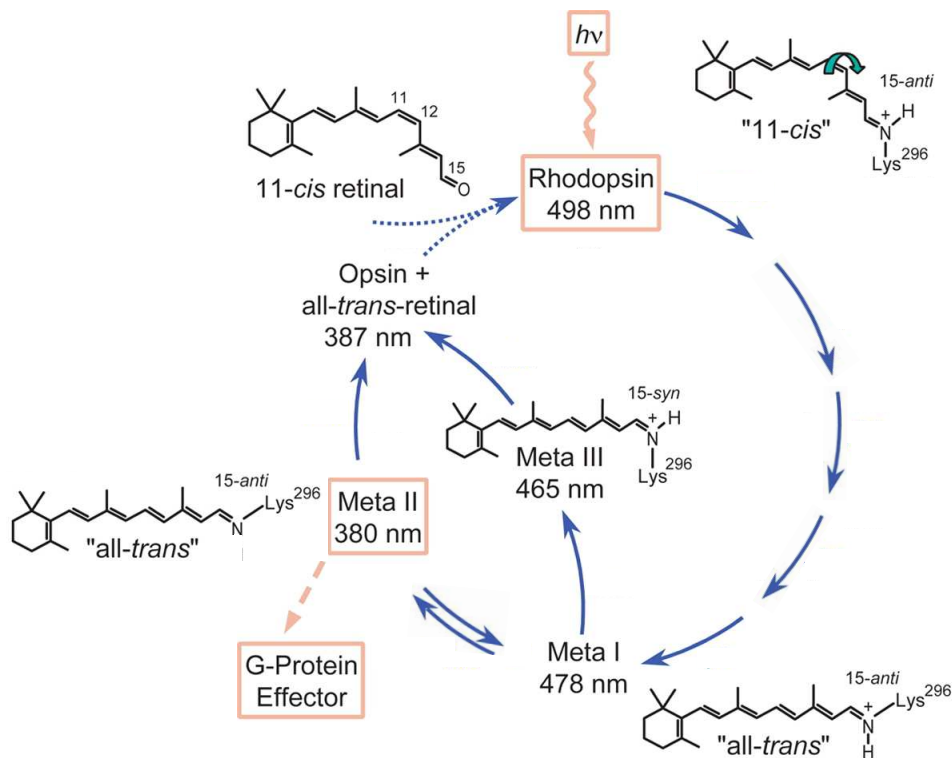


Figure 1.2.: The visual cycle (adapted from Ernst et al. (2014))

After illumination or bleaching, rhodopsin runs through several intermediates (photoisomerization). Each one of these can be distinguished by the absorption wavelength. During photoisomerization (green arrow) 11-*cis*-retinal converts to all-*trans*-retinal. The first intermediates of the visual cascade are very short-lived (Rando, 1996; Ernst et al., 2014) and therefore not depicted here. Metarhodopsin I (MI or Meta I) is the first stable conversion product. It absorbs light of 478 nm and is in equilibrium (Chabre and Breton, 1979) with metarhodopsin II (MII), absorbing mainly at 380 nm. Because of this blue-shift, the formation of MII can easily be distinguished via absorption measurements. Furthermore, MII is the active state of the photoreceptor and is able to interact and activate the G protein transducin. Opsin – the chromophore-free apoprotein – and all-*trans*-retinal are the direct decay products of MII. Metarhodopsin III (MIII) results from thermal isomerization of MI. MIII is again absorbing light of higher wavelengths than MII (465 nm). It can therefore hinder the spectroscopic quantification of the bleaching of rhodopsin, which with its absorption maximum of 500 nm absorbs in the same range than MIII. The formation of MIII should therefore be excluded. This can be done via shifting the equilibrium between MI and MII towards MII by a constant reduction of the amount of MII (Le Chatelier's principle). For this reason, hydroxylamine is used. The apoprotein opsin is replenished by the retinal pigment epithelium (RPE) to form again photoactivable rhodopsin. Microvillitis from the RPE are surrounding and nourishing the photoreceptor cells (resupply of 11-*cis* retinal). Absorption maxima correspond to bovine rhodopsin intermediates.

$h\nu$: photon energy

Within the visual cycle (Fig. 1.2) every intermediate shows another maximum peak. Nevertheless, the absorbances still are close to each other. In the visual cycle MII stands out - it is the active state of rhodopsin and the first intermediate, which is more stable. It absorbs light of 380 nm. Upon illumination, the absorbance of a retinal extract is changing, from 500 to 380 nm. However, this is only the case when avoiding blue light and under the presence of hydroxylamine. Ernst and Bartl showed that green light leads to photolysis of MII (Bartl, Ritter, and Hofmann, 2001; Ernst and Bartl, 2002). MIII ($\lambda_{max} = 465$) and P500 ($\lambda_{max} = 500$) are the photoproducts of this photolysis. Using a lamp, which only emits light above 420 nm, should successfully avoid photolysis of MII. Hydroxylamine disrupts the equilibrium between MI and MII and acts in two ways (Fig. 1.3).

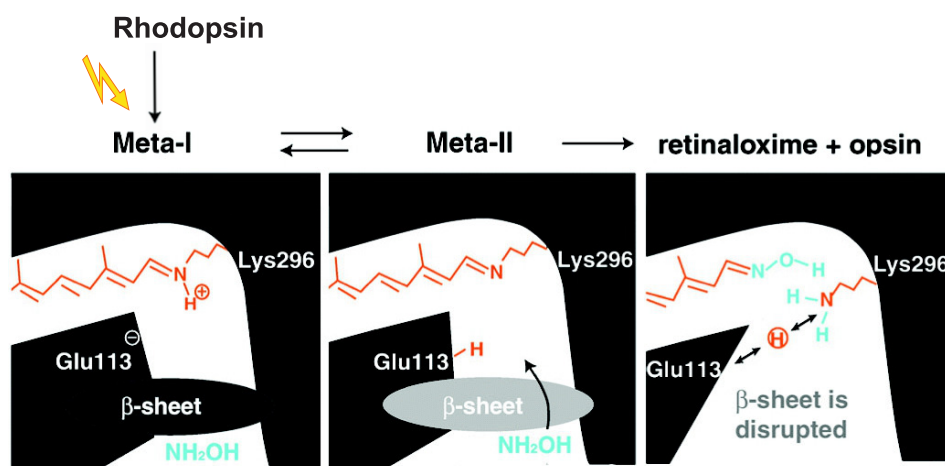


Figure 1.3.: Effect of hydroxylamine on rhodopsin intermediates (adapted from online abstract of Katayama, Furutani, and Kandori (2010))

Upon illumination (yellow arrow), a physiological equilibrium is established between MI and MII. A zoom-in into the retinal binding pocket shows the lysine residue (Lys296) which is responsible for the Schiff base linkage and the β sheet which covers the binding pocket. In the MI state, hydroxylamine cannot enter the pocket and, thereby, MI is not affected by hydroxylamine. In the MII state, the protein structure has changed, already. The β sheet has moved. Hydroxylamine can enter the binding pocket and release the chromophore as retinal oxim. The MI-MII equilibrium got thereby disrupted.

First, it is a moderate base, which can catch released protons and, thereby, affect the pH-dependent equilibrium between MI and MII. Secondly, it can enter the binding pocket of MII and release the chromophore. As a consequence, the visual cycle stops at MII. Spectroscopic signals at 500 nm can clearly be identified as emerging from MII – an overlap with MIII signals was avoided. Only by using hydroxylamine and green light, spectroscopic measurements make the rhodopsin bleaching comprehensible.

1.3. Rhodopsin and the question of its oligomeric state

The oligomeric state of rhodopsin has been a matter of research, as well as an issue for scientific discussions already for a long time. This section provides all necessary basics of historic experiments, arguments of the mentioned discussions about rhodopsin's oligomeric state, and more recent investigations that are required in the main part. Oligomerization of rhodopsin was investigated by various biochemical (section 1.3.1), spectroscopic (section 1.3.2), and biophysical techniques (section 1.3.3). Due to the nature of these experiments, corresponding publications are discussed in separate sections. Then, section 1.3.4 sets the classical view of the interaction of phototransduction proteins via collision coupling in contrast with the precoupling model. And finally, section 1.3.5 concludes with previous studies using electron microscopy (EM).

1.3.1. Biochemical studies

The first crosslinking experiment with rhodopsin in native disk membranes was performed by Downer et al. using glutaraldehyde. She could find crosslinked oligomers (Downer, 1985). However, due to the tendency of glutaraldehyde to form polymers of different sizes (Downer, 1985; Hermanson, 2013), these crosslinking results have been considered as originated from random collisions within the disk membrane. Later on,

other, more conclusive experiments have been done by Medina et al. (Medina, Perdomo, and Bubis, 2004) and Suda et al. (Suda et al., 2004), to mention two examples. Both, Medina et al. and Suda et al. used specific crosslinking chemicals and rather mild isolation procedures. They could mainly find dimers of bovine rhodopsin.

In contrast, Edrington et al. state that rhodopsin only forms dimers because of the crosslinking process itself and that rhodopsin in native disk membranes is monomeric (Edrington, Bennett, and Albert, 2008). Edrington et al. used bovine native and cross-linked disk membranes for the differential scanning calorimetry (DSC) study – dark-adapted and partially bleached disk membranes. DSC is a method to analyse thermal denaturation by heating up the sample from 20°C to 85°C (Edrington, Bennett, and Albert, 2008). Rhodopsin and opsin show different temperatures of irreversible thermal denaturation (Edrington, Bennett, and Albert, 2008). It's therefore possible to distinguish between these two proteins within the same sample. Edrington et al. found less than 5% of dimeric rhodopsin in native disk membranes. In this study the authors state, that cross-linking with DSP (dithiobis[succinimidylpropionate]) caused dimerization. – this crosslinking agent also has been in use by Suda et al. (Suda et al., 2004). However, if the crosslinked samples of Edrington et al. have been treated with the reducing agent TCEP (Tris(2-carboxyethyl)phosphine hydrochloride), all rhodopsin dimers vanished. This raises the assumption, that the dimers found are only preparation artifacts.

Jastrzebska et al. mainly found monomers of rhodopsin using DDM (Jastrzebska et al., 2004). Dimers were only observable if using DDM concentrations lower than 3 mmol/l (Jastrzebska et al., 2004). Using CHAPS (3-[(3-cholamidopropyl)dimethyl-ammonio]-1-propanesulfonate), Jastrzebska et al. state, that the rhodopsin oligomers (mostly dimers) are better preserved and less dissociated instead of using DDM. The authors further state, that the rhodopsin oligomers are more active – transducin activation constants

were measured to be 3 times higher than for the monomer (Jastrzebska et al., 2004). Thus, downstream effector activation assays may be influenced by the oligomeric state of the receptor and thereby by the choice of detergent used for the solubilization of the receptor molecules (Jastrzebska et al., 2004).

Other criticism on the work done by Medina et al. comes from Chabre and le Maire. Chabre and le Maire state, that Medina et al. have used experimental methods, which are proven to be not suitable for the purpose and that they handled wrong calculations and conclusions in the paper (Chabre and Maire, 2005). However, according to Chabre and le Maire, also Jastrzebska et al. are wrong talking about rhodopsin oligomers. They state, that Jastrzebska et al. could find dimers and higher oligomers of rhodopsin only due to the fact that solubilization, for both DDM and CHAPS, was incomplete (Chabre and Maire, 2005). Furthermore, Chabre and le Maire argue that dimerization among GPCRs mostly occurs for class C GPCRs (e.g. GABA receptors) and less for class A (e.g. rhodopsin) GPCRs (Chabre and Maire, 2005). Chabre and le Maire further state, that dimerization seems to be necessary only for trafficking of the receptor molecules to the corresponding membrane and has no functional role (Chabre and Maire, 2005).

In 2006, Kota et al. (2006) showed that opsins form dimers and furthermore which amino acids are responsible for dimerization.

In contrast, Ernst et al. could prove that dimerization is not necessary for the function of rhodopsin. Ernst et al. used rhodopsin, which was achieved by solubilization of bovine rod outer segments (Ernst et al., 2007). The authors of this study claim, that in fact monomeric rhodopsin is fully functional and not only able to couple with transducin, but also to activate 46 transducin molecules per second and rhodopsin molecule (Ernst et al., 2007). Ernst et al. also state that the reaction is nearly limited by the diffusion limit. That makes further acceleration of the transducin activation by oligomerization of

rhodopsin, as Jastrzebska et al. proposed earlier (Jastrzebska et al., 2004), rather unlikely.

These biochemical experiments indicate that rhodopsin is functioning as a monomer. Thus, dimerization is not essential for the function of rhodopsin within the phototransduction cascade (Chabre and Maire, 2005; Ernst et al., 2007).

Later on, fluorescent (FRET) and bioluminescent (BRET) resonance energy transfer studies demonstrated dimerization for different class A and class C GPCRs (Maurel et al., 2008). However, because of the experimental procedure (overexpression), it is not clear whether these results represent the native state. In fact, Jastrzebska et al. (Jastrzebska et al., 2006) showed that the oligomeric state of rhodopsin depends on the detergent used during preparation. According to their results not only monomeric rhodopsin, but even dimers or rows of dimers are able to activate transducin. The rate of transducin activation was highest for tightly packed rows of rhodopsin dimers (Jastrzebska et al., 2006).

With fluorescence binding assays, Bayburt et al. could further show that even monomeric rhodopsin embedded in nanodisks with a diameter of 10 nm is fully functional when it comes to activation of transducin (Bayburt et al., 2007) or deactivation via phosphorylation by the rhodopsin kinase (GRK1) or arrestin-1 binding (Bayburt et al., 2010). Chen et al. (2021) could recently resolve complexes of rhodopsin and its GPCR kinases (GRK1) after their reconstitution in nanodisks. Phosphorylation by GRK is the prerequisite for arrestin binding. The authors identified residues responsible for the interaction between GPCRs and kinases. According to Chen et al. (2021) these residues are highly conserved between GRKs and class A and B1 GPCRs. The use of nanodisks may be fruitful when analyzing rhodopsin and its interaction partners.

Becirovic et al. performed a coimmunoprecipitation study, which supports again oligomerization of rhodopsin (Becirovic et al., 2014). Among complexes composed of CNGB1a, rhodopsin, and peripherin-2, Becirovic et al. could also pull down dimers, trimers, and tetramers of rhodopsin by using the anti-rhodopsin antibody. These oligomers persisted under reducing conditions and are, therefore, true and not preparation induced oligomers (Becirovic et al., 2014).

Mishra et al. (2016) found by FRET imaging of CHO cells (which were modified to express fluorescently tagged opsin) that oligomerization is concentration dependent. The more opsin is present the more oligomers are formed. The authors found dimers, tetramers, and even higher-order oligomers (Mishra et al., 2016).

Even though dimerization happens, Jastrzebska et al. could show via blocking of putative dimer contacts that dimerization or coupling may not be necessary for the function of rhodopsin. Blocking was performed with synthetic peptides, derived from transmembrane (TM) domains; hence, the proteins are named TM1 to TM7, which are capable for self-assembly to the functional receptor (Jastrzebska et al., 2015). Jastrzebska et al. could detect via BRET that dimerization in presence of TM1, TM2, TM4, and TM5 was reduced. However, even if dimerization was blocked thereby, activation of transducin and signaling was still possible (Jastrzebska et al., 2015). Jastrzebska et al., therefore, speculate that dimerization might be needed for the stabilization of the rhodopsin-transducin complex or the organization of dark-adapted rhodopsin (Jastrzebska et al., 2015).

Recently, Kumar et al. (2018) could inhibit rhodopsin dimerization by subretinal injection of syntetic peptides into the living mouse eye and subsequent immunohistochemistry. These synthetic peptides were from the transmembrane region of GPCRs (Kumar et al.,

2018). Understanding the role of oligomerization of rhodopsin may lead to establish interventions to cure retinopathies in future.

Mallory et al. (2018) could show in their more recent BRET study, that the V209M and F220C mutations in transmembrane helix 5 (TM5) of rhodopsin rather cause a misfolding and mistrafficking than that they were dimerization-deficient. Dimerization seems to be a key function of rhodopsin.

Thus, the oligomeric state of rhodopsin and its arrangement appear to be dependent on the preparation.

It seems that there were two camps on the field of GPCR or rhodopsin science in the past. One camp was for and the other against oligomerization of rhodopsin. One can summarize, that biochemical studies are ambivalent on the oligomerization issue. However, during the last decade more papers were published, which support dimerization/oligomerization and organization of rhodopsin. Oligomerization also seems to be dependent on the environment, in which rhodopsin was examined. Nevertheless, the field of research dealing with GPCRs in general and rhodopsin in detail is huge and only some papers could be discussed, here.

1.3.2. Spectroscopic measurements

In the early seventies Cone, Liebman, and Entine showed by using spectrophotometric approaches that rhodopsin is highly mobile in disk membranes (Cone, 1972; Liebman and Entine, 1974; Poo and Cone, 1974). Thus, early spectroscopic measurements neglect oligomeric state for rhodopsin. This was commonly agreed by the scientific community. Later on, Govardovskii and his colleagues went out to address the question whether rhodopsin embedded in the disk membrane is motile or not. Spectroscopic measure-

ments of the lateral movement of rhodopsin within the intact rod cell by Govardovskii et al. showed that rhodopsin is motile, even if there would be a higher-order organization. The paracrystalline arrays of rhodopsin dimers, which Fotiadis et al. could find (Fotiadis et al., 2003), were difficult to reconcile with motile rhodopsin. That was the reason for Govardovskii et al. to readdress the question of rhodopsin's high lateral diffusion constant (Govardovskii et al., 2009). Govardovskii et al. used amphibian rods for their microspectrophotometric analyses. Like Cone, Liebman, and Entine before, Govardovskii et al. compared the absorbances of rhodopsin of one bleached half of ROS to the corresponding other half, which was not bleached. Different new insights were gained by these studies.

First, it was found out that metarhodopsin III might have interfered in the absorbance measurements of Cone, Liebman, and Entine. This is possible because metarhodopsin III has similar absorbance properties as rhodopsin. Therefore, its formation could simulate diffused rhodopsin.

Second, Govardovskii et al. identified highly varying fractions of immobile and mobile rhodopsin molecules in the disk membrane (Govardovskii et al., 2009). According to Govardovskii et al. , this is an indication that there is not only monomeric rhodopsin embedded in rod disk membranes.

Later on, Comar et al. used pulsed-interleaved excitation fluorescence cross-correlation spectroscopy (PIE-FCCS) to measure the oligomerization of rhodopsin in living cells in a time-resolved manner (Comar et al., 2014). PIE-FCCS enables the experimenter to track and quantify for example the total receptor amount of a living, fluorescing cell with a high precision and sensitivity (Comar et al., 2014; Müller et al., 2005). For the analysis, it does not matter if receptors oligomerize or diffuse – they are tracked anyway. Opsin, therefore, was expressed heterologously in COS7 cells (Comar et al., 2014). Comar et al. found half of the opsin, expressed in cultured cells, in dimeric complexes. They further state, that – in concentrations similar to living ROS cells – 87%

of the contained rhodopsin must be dimerized (Comar et al., 2014). However, Comar et al. used overexpression of opsin and it is not clear in which extent these results resemble rhodopsin within the native ROS.

Nevertheless, spectroscopic measurements indicate that dimerization is naturally occurring for rhodopsin.

1.3.3. Biophysical studies

In 1975, Hubbel published a freeze-fracture study on rhodopsin, embedded in synthetic membranes. Freeze-fraction electron microscopy takes advantage of the fact that within a frozen biological sample the cells break along their plasma membrane or one of their organelle membranes (see also review Severs (2007) and section 2.14). This method can uncover membrane proteins still embedded in their native environment. In fact, Hubbel found some particles with a diameter of 110 Å within the membranes, whereas monomeric rhodopsin should only have around 40 Å in diameter (Hubbell, 1975). However, he did not consider any organization of rhodopsin. Hubbel considered a preparational artefact (here, the platinum shadow could be thicker than usual) or associations of rhodopsin or lipids. Fotiadis et al. published the first AFM experiment, which already showed an ordered organization for rhodopsin (Fotiadis et al., 2003; Liang et al., 2003; Filipek et al., 2004). The results from previous AFM studies on ROS disks, found in the literature, are depicted in figure 1.4. Figure 1.4(A) and (B) represents the results from Fotiadis et al. , who detected paracrystalline arrays of rows made by rhodopsin dimers. Botelho and coworkers calculated that ROS membrane parameters like composition, energetics, and curvature not only allow but also support the rhodopsin organization (Botelho et al., 2006). Since then the presence of paracrystalline arrays in analysed ROS disks was challenged by various groups.

The data obtained by Buzhynskyy et al. (Fig. 1.4(C) and (D)) unveiled a loosely packed

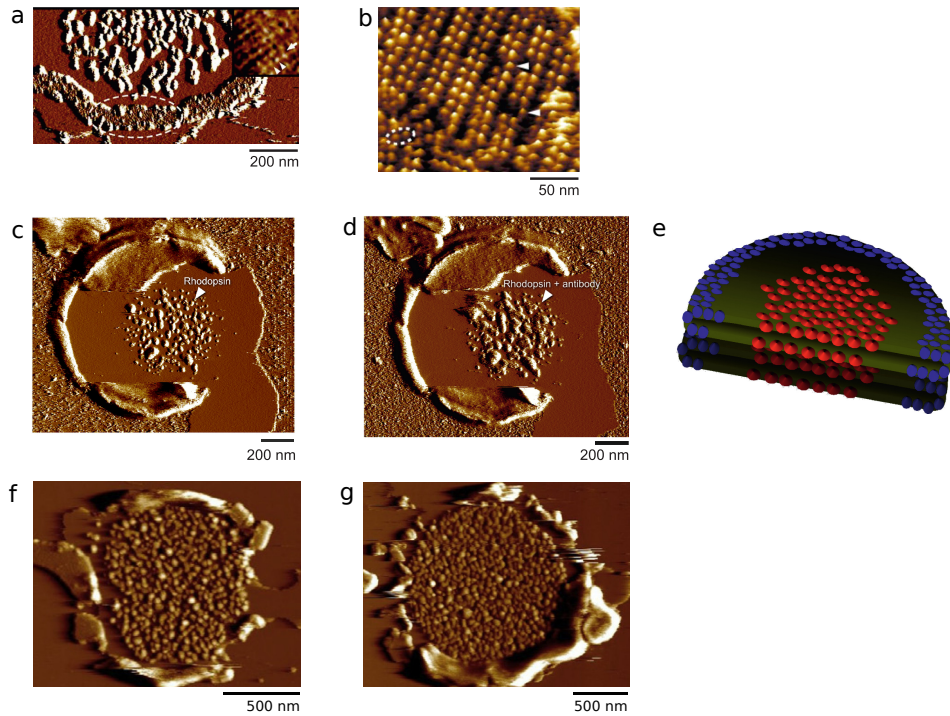


Figure 1.4.: Previous studies using Atomic-force microscopy (AFM) (each adapted from its original publication)

AFM allowed the identification of two different higher-order structures of rhodopsin in disk membranes. Disk membranes obtained from mammalian ROS has been adsorbed to mica prior to imaging. (A) and (B) Deflection images from Fotiadis et al. (2003). Rhodopsin dimers form randomly orientated rows. Here, mouse ROS were used for the preparation. (B) Paracrystalline arrays of rhodopsin are visible in the detailed view. (C) and (D) Deflection images from Buzhynskyy, Salesse, and Scheuring (2011), with and without use of anti-Rhodopsin antibodies, respectively. (E) Corresponding model (Buzhynskyy, Salesse, and Scheuring, 2011), showing a central aggregation of rhodopsin within bovine disk membranes. (F) and (G) Deflection images from Whited and Park (2015), showing rhodopsin nanodomains in human and mouse ROS disks, respectively.

area in the middle of each disk membrane which turned out to be mainly formed by rhodopsin as indicated by the detection of monoclonal anti-rhodopsin antibodies (Buzhynskyy, Salesse, and Scheuring, 2011). According to Buzhynskyy et al. , this central area of the disk is supposed to be bounded by a protein-free girdle formed by lipids. The disk rims, here, contain a huge amount of peripherin-2 (Buzhynskyy, Salesse, and Scheuring, 2011).

These findings from Buzhynskyy et al. , who used bovine eyes for the isolation of ROS disks, are completely contradictory to the AFM study of Fotiadis and his colleagues, who used mouse ROS disks. One could speculate that the differences in both proposed organizations of rhodopsin (Fotiadis *versus* Buzhynskii) would also have a different impact on the downstream signaling in the phototransduction cascade.

The different results obtained by Fotiadis et al. and Buzhynskyy et al. might also be preparation artifacts, because the ROS disks were isolated prior to the adsorption to mica surfaces (Fotiadis et al., 2003; Buzhynskyy, Salesse, and Scheuring, 2011; Blankenship and Lodowski, 2015; Bosshart, Engel, and Fotiadis, 2015).

Another study supporting the dimerization of rhodopsin was published in 2006. Jastrzebska et al. wrote again, that rhodopsin is more active in its oligomeric form (Jastrzebska et al., 2006). They used several detergents with sugar (*i.e.* polar) headgroups and various alkyl chain lengths (DDM and its longer derivatives TDM and HDM). With HDM they could find the highest degree of oligomerization and could already observe arrays of rhodopsin dimers in TEM images of negatively stained rhodopsin solubilisates (Jastrzebska et al., 2006). Jastrzebska et al. state that the higher the amount of oligomerization, the faster the activation of transducin (Jastrzebska et al., 2006). They further state that monomeric rhodopsin has lost its capability for efficient transducin activation (Jastrzebska et al., 2006).

Whited and Park involved in their AFM studies (see Fig. 1.4F and G) ROS disks obtained from human eyes (Whited and Park, 2015). They drew the comparison to mice, as well, and found similar rhodopsin nanodomains as Buzhynskyy et al. Whited and Park report the size of the rhodopsin nanodomains to be 1109 nm (human) or 1245 nm (mouse) (Whited and Park, 2015).

Rakshit and Park (2015) could show via AFM that in four week-old heterozygeous rhodopsin knock-out (KO) mice the rhodopsin amount in the ROS, the size of nanodomains, and the diameter of ROS disks is reduced compared to wild-type mice. Interestingly, the authors could show that there is an adaptive mechanism – as the structural consequences, they saw for the four week-old KO mice, disappear with increasing age (Rakshit and Park, 2015). Thus, the amount of rhodopsin has influence on ROS morphogenesis.

Recently, AFM was used as a control experiment showing that a docosahexaenoic acid (DHA-) deficient diet for mice results in impaired vision, but does not affect oligomerization of rhodopsin or alters the disk structure (Senapati et al., 2018; Senapati and Park, 2018). Senapati et al. could show in 2019, that it is possible to distinguish between active and inactive rhodopsin via AFM (Senapati et al., 2019). They used Force-distance curve-based AFM (FD-AFM) on isolated ROS disks with which even binding kinetics should be possible to be analysed (Senapati et al., 2019).

Sechrest et al. (2020) analysed *Prcd*-KO mice with impaired vision. Via TEM of conventionally fixed retinas and light microscopy they could show, that disk morphology was altered. Sechrest et al. also used AFM as a control experiment showing that the amount of rhodopsin nanodomains was reduced in *Prcd*-KO mice disk membranes. The authors state that the exact role of PRCD remains unknown so far (Sechrest et al., 2020). In summary, it can be said that there are AFM studies, performed with mouse (Fotiadis et al., 2003; Liang et al., 2003; Suda et al., 2004; Whited and Park, 2015; Rakshit and Park,

2015; Senapati et al., 2018; Senapati and Park, 2018; Senapati et al., 2019; Sechrest et al., 2020), bovine (Buzhynskyy, Salesse, and Scheuring, 2011), and human (Whited and Park, 2015) ROS, showing that there is present a nanodomain organization of rhodopsin. This could be an indication, that nanodomain organization might be a feature of rhodopsin across species or maybe among class A GPCRs in general.

Publications where non-native samples were used to examine rhodopsin's oligomerization are detailed in the following.

Zhao et al. (2019) could recently successfully reconstitute rhodopsin dimers in nanodisks and perform a single-particle analysis. They could show dimerization within the nanodisks and hypothesize that the rhodopsin dimer can easily form a complex with either two G proteins or two arrestins, or form a heterogenous complex with one of each (Zhao et al., 2019). Zhao et al. (2019) postulate that movement and function should not be restricted by complex formation. Gao et al. (2019) performed single-particle cryo-EM with purified bovine ROS membranes and could reconstruct rhodopsin-transducin complexes with or without nanobodies. This publication gives more insight about the nucleotide exchange within transducin (Gao et al., 2019). The work done by Zhao et al. and Gao et al. also point towards oligomerization and formation of precomplexes.

Besides these EM studies mentioned above, there were several new structures published in the PDB within the last years – derived from X-ray diffraction of crystals or single-particle analysis. For GPCRs in general, but also for class A GPCRs and especially rhodopsin. And due to the technical achievements, many more will come. Basith et al. (2018) even speaks about a "golden age for GPCR structural biology". Chen et al. (2021) for example published recently the structure of the complex of rhodopsin and its GRK (PDB: 7MTB). Sander et al. (2022) published several X-ray structures of Arrestin-1 in complex with different phosphoinositols, which seem to be guiding arrestin-1 to the

outer segment (PDB: 7JSM, 7JTB, 7JXA, 7MOR, 7MP0, 7MP1, 7MP2). Both papers are expanding our knowledge about desensitization of activated rhodopsin.

It has to be stressed that all these AFM, EM, and X-ray studies needed further isolation processes and pretreatments of the ROS sample. Nevertheless, these biophysical studies point towards supramolecular organization for rhodopsin. For cryo-electron microscopy of vitrified sections (CEMOVIS) the samples are directly frozen after tissue preparation without any prior isolation or pretreatment. The consequence of this important difference is that the native state of the cellular and molecular organization should be maintained best with CEMOVIS. CEMOVIS was applied by Gunkel (2013) and Gunkel et al. (2015) and will be of focus in section 1.3.5.

CEMOVIS was also used by Pöge et al. (2021) to analyse retinal sections. The authors could on the one hand gain resolution and contrast by using the *Volta phase plate* and on the other hand identify connectors at the disk rim region, which have been discussed in section 1.2.1. However, whereas Pöge et al. (2021) focused on the disk rim, we want to focus on the supramolecular structure of rhodopsin within the disk membranes.

1.3.4. Collision coupling vs. precoupling

Any structural organization of rhodopsin would require an underlying interaction between the rhodopsin molecules. Maybe, an organization is necessary for the function of rhodopsin. On the other hand, the interaction with phototransduction factors like transducin or PDE might be more effective. This section focusses on the kind of underlying interaction between photoactivated rhodopsin and transducin. Both, a more random (e.g. collision coupling) or previously arranged (e.g. precoupling) interaction, seems possible at first. However, any higher-order organization of rhodopsin could be a hint towards an underlying precoupling mechanism.

For a long time, collision coupling was the only model considered for the interaction between a GPCR and its G protein (Oldham and Hamm, 2008; Hein and Bünemann, 2009). The model of collision coupling describes stochastic interactions between an active receptor and the G protein. Thus, the proteins interact with each other whenever they come in contact.

However, could there be a model for interactions that is less relying on stochastic events? A model which seems to be more effective? The proteins could accumulate at a certain spot and interact faster than just by stochastic interaction? Several factors could already assemble before the cascade is activated. A precoupled state, therefore, seems likely, in which rhodopsin, transducin, and the PDE are already in close proximity to each other. The following explains how a precoupled state could be formed.

Lefkowitz and his coworkers proposed a ternary complex model for β -adrenergic receptors (β AR) – another class A GPCR – composed of three components (agonist, receptor, and a GTP-hydrolysing component) (De Lean, Stadel, and Lefkowitz, 1980) and which culminated then in a 3D structure of the complex (Rasmussen et al., 2011). Lefkowitz' group further suggested that the GTP-hydrolysing “additional component”, now known to be the activated G protein, is transducing the signal to the corresponding effector molecule, the adenylate cyclase (De Lean, Stadel, and Lefkowitz, 1980).

Coupling of receptor and G protein was demonstrated for activated receptors but the question remains unclear how it looks like for not-activated receptors. Do receptor and G protein precouple prior to receptor activation? What might be the functional significance?

Ianoul et al. investigated the β -adrenergic receptor, as well. They reported from nanometer domains of about 140 nm in diameter, they found on heart myocytes (Ianoul et al., 2005). Ianoul et al. used near-field scanning optical and fluorescence microscopy and could find these domains mostly in or in the vicinity of caveolae. They contained huge amounts of β -adrenergic receptor complexes forming functional signalosomes (Ianoul

et al., 2005). The authors speculate that these nanodomains or signalosomes enable myocytes to respond effectively to stimuli. Signalosomes seem to be set up and ready for signal transmission. One can further speculate, that receptor organization may be a common feature among GPCRs and, in fact, play a functional role.

There is evidence for the formation of stable complexes between a receptor and its G protein before receptor activation. To name a few examples, Lachance et al. demonstrated the interaction between the β_2 -adrenergic receptor and the corresponding G_i via coimmunoprecipitation in the absence of the agonist (Lachance et al., 1999), whereas Alves et al. showed – using plasmon-waveguide resonance spectroscopy – that transducin is coupling to dark-state rhodopsin (Alves et al., 2005).

BRET and FRET studies (reviewed in Eidne, Kroeger, and Hanyaloglu (2002)) using fluorescently labeled receptors and G proteins provided evidence for precoupling of receptor and G protein (Gales et al., 2006). However, these studies were performed in a non-native environment, because interaction partners had to be overexpressed in heterologous cell systems to reach a sufficient signal strength for detection. Coimmunoprecipitation studies performed in the presence and absence of agonist suggested precoupling for β_2 - and α_2A -adrenergic and δ -opioid receptors (Hein and Bünemann, 2009). However, for somatostatin receptors, it was shown that the receptor only interacts with G_{α_i} in the presence of somatostatin (Gu and Schonbrunn, 1997). All four of these receptors are members of the rhodopsin family of GPCRs and belong either to the α -group (adrenergic receptors) or the γ -group (opioid and somatostatin receptors) (Fredriksson et al., 2003). Thus, coupling of receptor and G protein seems to differ even among rather closely related GPCRs. In 2011, Dell’Orco and Koch proposed a dynamic scaffolding mechanism for interactions between dark-state rhodopsin and transducin (Fig. 1.5).

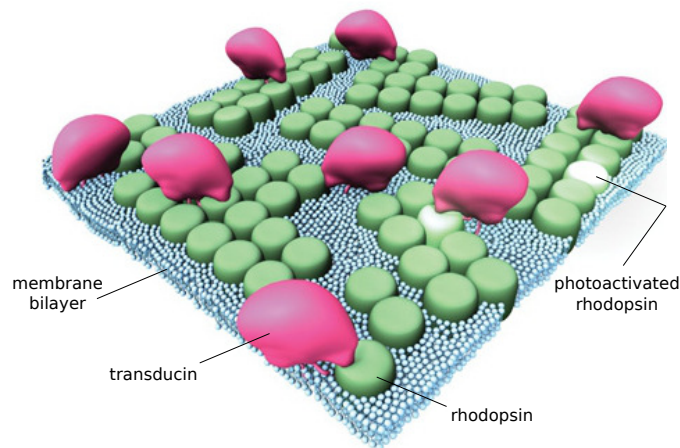


Figure 1.5.: Rhodopsin and transducin interact in a dynamic scaffolding mechanism (adapted from Dell’Orco and Koch (2011))

Within the dynamic scaffolding mechanism, rhodopsin dimers (green balls) are arranged in paracrystalline arrays to which 25 % of all transducins (pink spheres) are dynamically precoupled (Dell’Orco and Koch, 2011). White rhodopsin molecules have been activated by photoisomerization.

According to their Monte Carlo simulations, 25 % of the transducin molecules are precoupled to rhodopsin (Dell’Orco and Koch, 2011). Nevertheless, if precoupling exists, the dissociation rate has to be high to maintain an advantage compared to the collision coupling model. Only a high dissociation rate of precoupled and of activated transducins can serve for the given transducin diffusion rate (Dell’Orco and Koch, 2011) and a fast visual transduction cascade in which one single activated rhodopsin molecule activates several G proteins within a short period of time (Gunkel et al., 2015; Koch and Dell’Orco, 2015).

Becirovic et al. did some coimmunoprecipitation experiments in 2014. Using anti-CNGB1a antibodies, they could pull down the receptor rhodopsin together with its most downstream effector molecule, the cyclic nucleotide-gated (CNG) channel (Becirovic et al., 2014). Whereas rhodopsin is embedded in the disk membranes, the CNG channel is a membrane protein of the plasma membrane. However, at the disk rim both come in contact. With this study, Becirovic et al. proved that in fact rhodopsin, peripherin-2, and

CNGB1a are located in the same complex at the disk rim.

How can precoupling be achieved within the ROS?

For answering this question, we have to take the detour via subcompartmentalization. The more proteins come in contact, the more transient interactions as in signaling cascades are likely. This assumption is supported by the idea of fence pickets by Ritchie et al. (2003). Here immobilized proteins act as fence pickets restraining lipids and thereby limiting their free diffusion (Ritchie et al., 2003). Even diffusion of membrane proteins might be limited by cytoskeletal elements like microtubules and thereby concentrated locally. You can even call it subcompartmentalization (Jaqaman et al., 2011). There are hints in the electron micrographs that cytoskeletal filaments are covering the membrane between two tracks. In this way a confinement zone for transducin could be established. The higher-order structures of rhodopsin, Gunkel et al. could identify, may similarly enhance the likelihood of the activation of transducin if its diffusion is limited to e.g. the space between two rows of dimers of one track. Gunkel et al. not only proposed that rhodopsin is forming a higher-order structure but also raised the idea that these supramolecular structures of rhodopsin are acting as traps for signaling molecules like the subcompartmentalization proposed by Jaqaman et al. (2011) for CD36.

All the aforementioned studies indicate, that there is a higher organization of rhodopsin. In 2015, Gunkel et al. could draw a more precise picture of this organization (Gunkel et al., 2015), which will be detailed in the next section.

1.3.5. Rhodopsin is organized as double-rows of dimers

In the context, whether oligomerization is caused by the sample preparation, the results of Gunkel et al. (Gunkel, 2013) with cryo-fixed retinas represent an important advance because they are obtained under close-to-native conditions without any detergent-assisted

solubilization. Neither an isolation of ROS was necessary prior to cryo-fixation, nor the sample had to be dehydrated. Furthermore, the oligomeric state of rhodopsin might be necessary for the putative precoupling of phototransduction proteins (Section 1.3.4). Precoupling means that phototransduction proteins, as transducin and maybe even the PDE, are preassembled to rhodopsin or rhodopsin oligomers to form a unit, ready for an effective signal transduction after the perception of light.

Via analysing cryo-sections of the retina by electron tomography (CEMOVIS), Gunkel *et al.* could detect a unique pattern of higher-order structures of rhodopsin in the disk membrane (Fig. 1.6A).

According to their results, rhodopsin dimers form paired rows, so-called tracks, with a distance of 5.7 nm. Tracks which are oriented parallel to the incisure are separated by 15 nm. A rhodopsin density of around 20,000 molecules per μm^2 was calculated, which is in line with previous data obtained by Nickell *et al.* ($24,102 \mu\text{m}^{-2}$) (Nickell *et al.*, 2007).

It cannot be excluded that in addition to oligomeric rhodopsin also monomeric rhodopsin exists. Non-associated, monomeric rhodopsin molecules would be filtered out by the subsequent data analysis. This is because monomeric rhodopsin is distributed stochastically over the disk membrane, whereas rhodopsin tracks are arranged in a similar manner and spread over the whole disk membrane. Thus, the real rhodopsin density may be higher than the 20,000 molecules per μm^2 , found by Gunkel *et al.*

In general, fast diffusion, as it was reported for rhodopsin, seems not possible for areas which are highly ordered. However, an effective precoupling mechanism could circumvent the necessity of fast diffusion to ensure a fast signal transduction (Gunkel *et al.*, 2015; Koch and Dell'Orco, 2015). Ramirez and Leidy (2018) also performed Monte Carlo

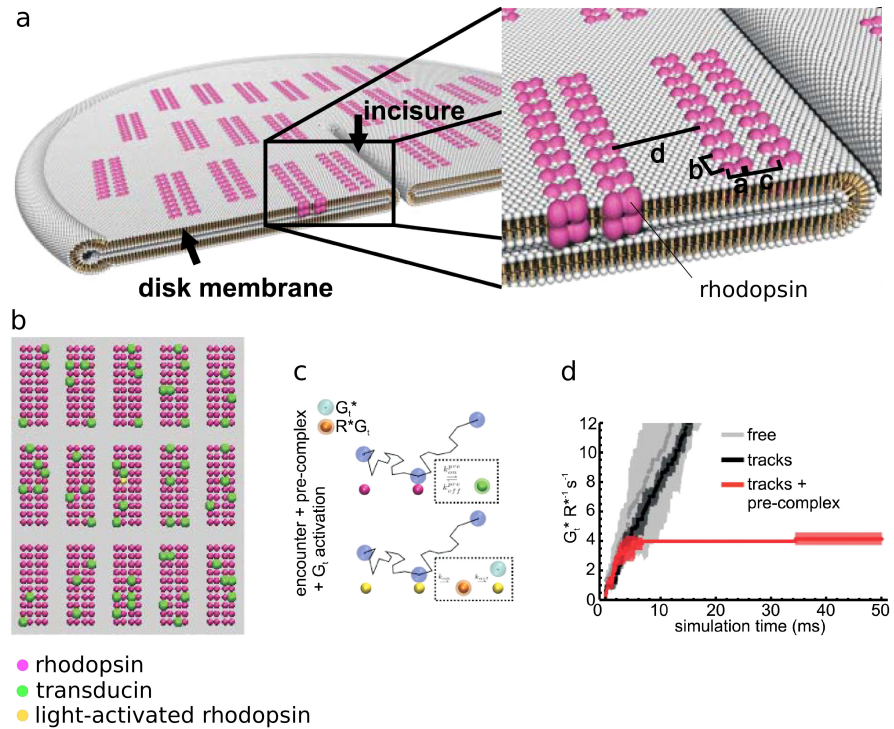


Figure 1.6.: **Model for rhodopsin organization and simulation of precomplex formation with transducin (G_t) [adapted from Gunkel et al. (2015)]**

a) Model for higher-order architecture of rhodopsin in dark-adapted native rod disk membranes (Gunkel et al., 2015). Paired rows of rhodopsin dimers (magenta), also called tracks, are arranged parallel to the disk incisure. They found the following parameters of the unique architecture: Rh monomers within one dimer are located 4.3 nm apart from each other (a), whereas Rh dimers within the row are separated by 5.5 nm (b). The two rows of one track are 5.7 nm apart (c). The next Rh tracks comes in 15 nm distance (d). b, c) simulation setup with a disk membrane patch. Physiological densities of Rh and G_t are displayed. One rhodopsin molecule got activated by light (yellow). b) In this setup G_t and Rh are forming precomplexes. Transducin is moving along the rhodopsin rows, scanning for activated rhodopsins. c) Precomplexes can be either inactive (Rh bound G_t) or active (G_t bound to activated Rh; orange). d) The presence of inactive and active precomplexes suggest biphasic kinetics. After 50-100 ms, all transducin molecules trapped in one track got activated. New inactive G_t molecules first must be recruited from neighbouring tracks before signaling can go on.

G_t : Transducin; R^*G_t : G_t bound to light-activated Rh; Rh : Rhodopsin

simulations to find out similar results – the association rates between rhodopsin and transducin are higher in the static organization than diffusing as monomers (Ramirez and Leidy, 2018).

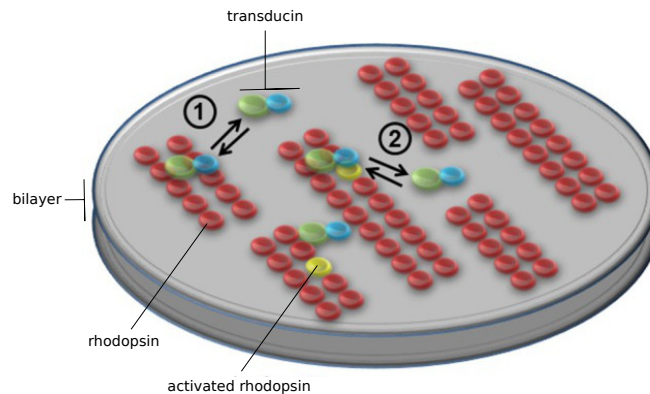


Figure 1.7.: Model for organization of rhodopsin and interaction with transducin (adapted from Koch and Dell’Orco (2015))

Rhodopsin is organized as tracks within the disk membrane. Dark-state rhodopsin is able for precoupling of transducin (formation of complex ①). This is a fast interaction – transducin hops on rhodopsin and off again quickly. Formation of complex ② – the interaction between light-activated rhodopsin (*i.e.* MII) and transducin lasts longer – thereby, transducin can be activated. The dissociation rate of complex ① is more than 300-fold faster than of complex ② (Koch and Dell’Orco, 2015).

Transducin could scan along a row of rhodopsin dimers. With a hopping on and off-mechanism, which is carried out fast, the efficiency for activation of transducin might be enhanced.

The understanding of the processes involving rhodopsin requires further studies on this field of research. A possible question may be: what advantages are given by an organization and maybe even by a coupling of phototransduction factors? The next step towards understanding of this organization can be to break it off. And in fact, in preliminary experiments with retinas that had been illuminated prior to cryo-preservation, Gunkel could not detect rhodopsin tracks in the tomograms anymore, which leads Gunkel et al. to the assumption that rhodopsin rows might dissociate upon illumi-

nation (Gunkel, 2013). Nevertheless, first we have to focus on the reproducibility of the structural analyses (see section 1.4).

1.4. Aim of the thesis

With this thesis it was intended to take a closer look at the astonishing higher-order architecture of rhodopsin found by Gunkel (2013) and Gunkel et al. (2015) and to pave the ground for experiments with the illuminated retina. As a preparation for the structural analysis of illuminated retinas, the bleaching effect on rhodopsin needed to be evaluated and quantified. Therefore, experiments to illuminate native retinas, their subsequent lysis, and quantification of the bleaching needed to be implemented in the lab (first aim).

The technique of CEMOVIS, Gunkel et al. used, needed to be revised and replaced by alternative techniques. The reason for this was that this technique was no longer feasible for studies including the analysis of different conditions. CEMOVIS was the method of choice to investigate the higher-order structure of rhodopsin for one single illumination state (dark state). However, to analyze and compare different illumination states, this technique turned out to be too time-consuming. Structural information should be gained in a timely manner. For this reason, different techniques needed to be set up and compared (second aim).

Keeping the demand for the alternative technique for the structural analysis of rhodopsin in mind, one can pose further requirements. This alternative technique needs to be reproducible, fast compared with CEMOVIS, reliable, and little error-prone. Only then, it will be possible to analyse the impact of different illumination conditions on the photoreceptors. Several electron microscopy techniques will be compared for feasibility and output. The following list gives an overview of the technical modifications.

- Cryo-sectioning

-
- Acquisition method of tomography
 - Rod outer segment solubilization as a source of samples for vitrification and subsequent tomography
 - Freeze fracture as a source of samples for tomography
 - Focused-ion beam as a source of samples for tomography
 - Atomic-force microscopy on isolated disk membranes

Finding the method of choice for the structural analysis of the higher-order structure of rhodopsin and quantification of the bleaching of rhodopsin in the native retina are the two prerequisites for further analysing the consequences that follow the illumination of rhodopsin and its putative changes of the higher-order structure. With further research concerning the issue of rhodopsin dissociation upon illumination, one could gain profound knowledge about the mechanisms behind phototransduction.

The intention of this work was to quantify the bleaching of rhodopsin after illumination of the intact retina. The second aim was to find an alternative technique to investigate a putative change of the higher-order structure of rhodopsin instead of CEMOVIS.

2. Materials and Methods

This chapter shows how the experiments were performed, beginning with mentioning all materials (section 2.1), software (section 2.2), and other resources (section 2.3) used. Section 2.4 gives an overview about the experimental workflow. Section 2.6 starts by providing details about the experimental procedure of the solubilization of the mouse retina, which dissection is described in section 2.5. All further experiments follow. Wherever necessary, background information is added.

2.1. Materials

The companies and their headquarters from which material was purchased are named, but no details are given. Additional product details are written in the following chapters corresponding to the experiments.

Chemicals were purchased from Sigma-Aldrich Co. LLC (St. Louis), Carl Roth GmbH (Karlsruhe) and Anatrace (Maumee).

General lab equipment was ordered at Carl Roth GmbH (Karlsruhe), VWR International LLC (Radnor), Merck Millipore (Billerica), Macherey-Nagel GmbH & Co. KG (Düren), B. Braun Melsungen AG (Melsungen), Abbvie Inc. (North Chicago), and Hellma GmbH & Co. KG (Müllheim).

Mixing during retinal solubilization was done with devices from Eppendorf AG (Hamburg) and LMS Co (Hongou).

Centrifuges were purchased from Beckman Coulter Inc. (Brea), and Heraeus GmbH

(Hanau).

Any additional equipment necessary for the retina dissection and solubilization were purchased from Nikon (Tokyo), Ismatec (Wertheim), Gossen-Metrawatt GmbH (Nürnberg) and Branson Ultrasonics Corp. (Danbury).

Light-emitting diodes (LEDs) and accessories, used for the bleaching experiments, were ordered from OSRAM Licht AG (München) and Thorlabs Inc. (Newton).

Spectroscopic Measurements were done with equipment bought from Ocean Optics, Inc. (Dunedin) and Varian Inc. (Palo Alto).

General electron microscopy (EM) accessories, like forceps, knives, grids, and other specimen supports were bought from Plano GmbH (Wetzlar), Quantifoil Micro Tools GmbH (Großlöbichau), DiS-Galetzka (Weinheim), Science Services GmbH (München), and Diatome AG (Biel).

For high-pressure freezing (HPF) the EM HPM100 from Leica Microsystems GmbH (Wetzlar) was used. Accessories needed for HPF and post-processing of specimens, like specimen carriers, Protein A gold and evidots were ordered from Engineering Office M. Wohlwend GmbH (Sennwald), Cell Microscopy Core – CMC from the University Medical Center (Utrecht), and Evident Technologies Inc. (Troy).

For polishing of carriers the grinding/polishing device LaboPol-1 (Struers, Ballerup) with polishing disks P500, P1000, and P2000 was used. The focused-ion beam (FIB) from Carl Zeiss AG (Oberkochen) has been used in this study.

Glow discharging of specimen supports prior to sectioning and sputtering of FIB samples has been carried out with instruments from Bal-Tec AG (Balzers) and Balzers Union AG (Balzers).

The atomic-force microscope was purchased from JPK Instruments AG (Berlin).

All solutions and buffers were prepared with double-distilled water and, if necessary, autoclaved (20 min at 121°C, 2.5 bar). Therefore, the Systec Varioklav 500 E from Systec GmbH (Wettenberg) was used.

2.2. Software

The software programs, which were used within this thesis, are listed in Tab. 2.1.

2.3. Mice

All animals were handled according to the relevant guidelines and regulations (Landesamt für Natur, Umwelt und Verbraucherschutz, LANUV; reference number 84-02.04.2012.A192). For solubilization experiments – and also for experiments in which the intact retina was high-pressure frozen – only C57Bl/6NR_j mice were used. These mice are referred to as wild type (WT) mice in the following. C57Bl/6NR_j mice were either obtained from Jackson laboratory (Bar Harbor) or bred in the in-house animal facility. The age of WT mice used for the mentioned experiments varied from six to 27 weeks.

In the beginning, as experiments needed to be set up, like the retinal extraction or isolation of rod outer segments (ROS), also transgenic mice were used due to the high amount of mice necessary for these experiments. These transgenic mice belonged to the strains mICNBD-FRET/C57Bl6NR_j, bPAC/C57Bl6NR_j, or Ai36-GCamp3-LoxP/C57Bl6NR_j. Nevertheless, none of these transgenic mice should develop a defect in the visual system. In fact, all of these strains had a C57Bl/6 NR_j background. For the optimization of the plunge-freezing process, a putative age-related decrease in the length of single photoreceptors does not matter, thereby also the average age (eight to 62 weeks) of these transgenic mice was higher than for the WT mice.

Unless stated otherwise, the mice were dark-adapted preferably over night or for at least 4 hours.

Table 2.1.: Software programs used in this study

Name	Version	Developer	Note	Reference
Cary WinUV	3.0	Agilent Technologies	Spectrophotometric scan application	
Chimera	1.11.2	Resource for Biocomputing, Visualization, and Informatics; University of California	Software for Visualization of structures or alignments	(Pettersen et al., 2004)
CorelDraw X6	16.1.0.843	Corel	Vector graphics editor	
Digital Micrograph	3	Gatan	Image processing and manipulation program	(Mitchell and Schaffer, 2005)
EMAN2	2.12	Baylor College of Medicine	Image processing software	(Tang et al., 2007)
FEI tomography	4	FEI	Program for tomogram acquisition	
IMOD	4.7.15	Boulder Laboratory for 3-Dimensional Electron Microscopy of Cells; University of Colorado	Software package for tomographic reconstruction and modelling	(Mastronarde, 1997)
ImageJ	1.49d	National Institutes of Health (NIH)	Image processing platform	
Inspect3D	4	FEI	Tomography post-alignment and reconstruction module	
JPK DP	4.3	JPK Instruments	AFM data processing software	
OOIBase32		Ocean Optics, Inc.	Spectrometer Operating Software	
OriginPro	9.0.0G	OriginLab	Software for scientific graphs and data analysis	
PeakFit™	4.12s	Systat Software Inc.	Peak analysing software package from SigmaPlot	
Python	2.7	Python Software Foundation	Programming language	
SerialEM	3.6	Boulder Laboratory for 3-Dimensional Electron Microscopy of Cells; University of Colorado	Software package for automated tilt series acquisition	(Mastronarde, 2005)

2.4. Experimental overview

During this study, different techniques were compared or repeated with a different kind of sample. An overview of these experiments is depicted in Figure 2.1.

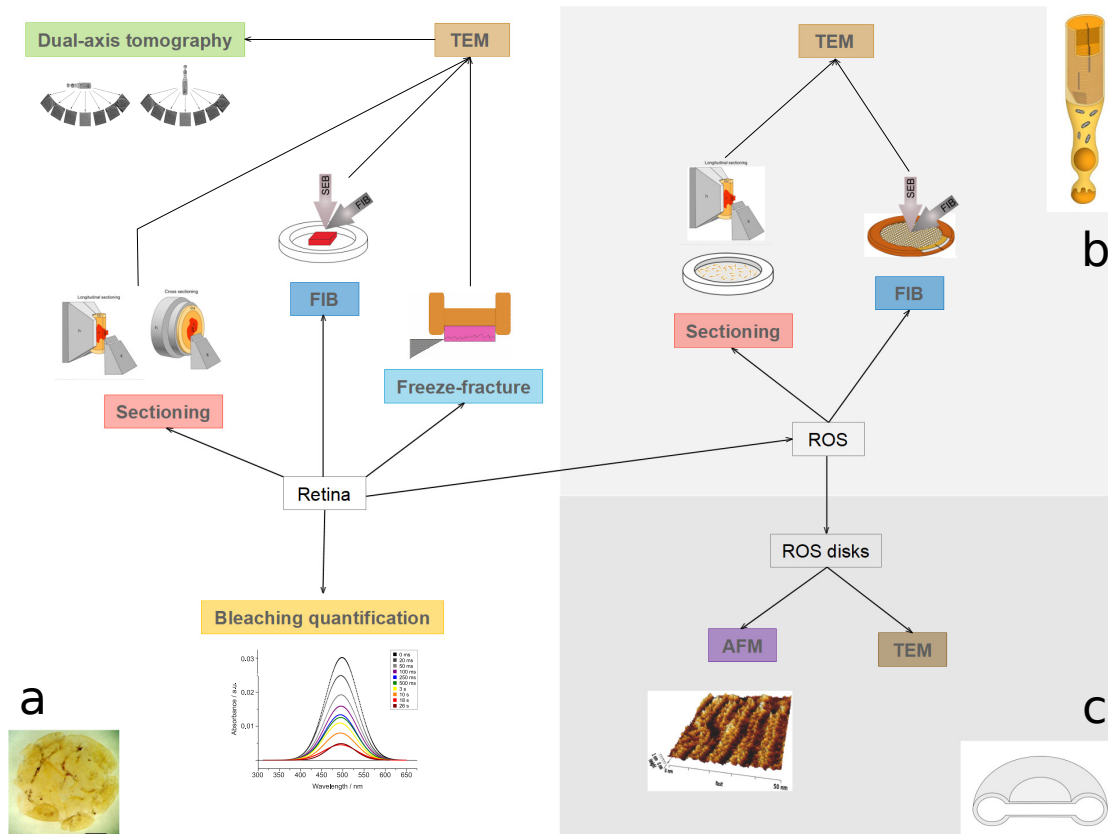


Figure 2.1.: **Experimental overview**

a) Investigations with the native retina. Sectioning illustration was adapted from Gunkel (2013). The illustration of tomogram acquisition was inspired from Lučić, Förster, and Baumeister (2005). b) Investigations at the isolated rod outer segment. The illustration of the ROS is taken from Gunkel (2013). The illustration of thinning vitrified ROS via FIB is adapted from Rigort et al. (2012). c) Investigations with isolated ROS disk membranes.

AFM: Atomic force microscopy; FIB: Focused-ion beam; ROS: rod outer segment; TEM: Transmission electron microscopy

2.5. Retina dissection

If not stated differently, all experiments regarding retinal dissection and ROS isolation were carried out in the dark. Also mice for illumination experiments were dark-adapted beforehand. This ensured that only a certain amount of light, which was controlled carefully with the experimental conditions, hit the retina. Due to the absence of night vision goggles, the preparation was done with the help of red light bulbs. The emission spectra of these dissection bulbs were measured with the help of Dr René Pascal. For this purpose the spectrometer S1024DW (Ocean Optics) was used. The resulting spectra are plotted in Fig. 2.2.

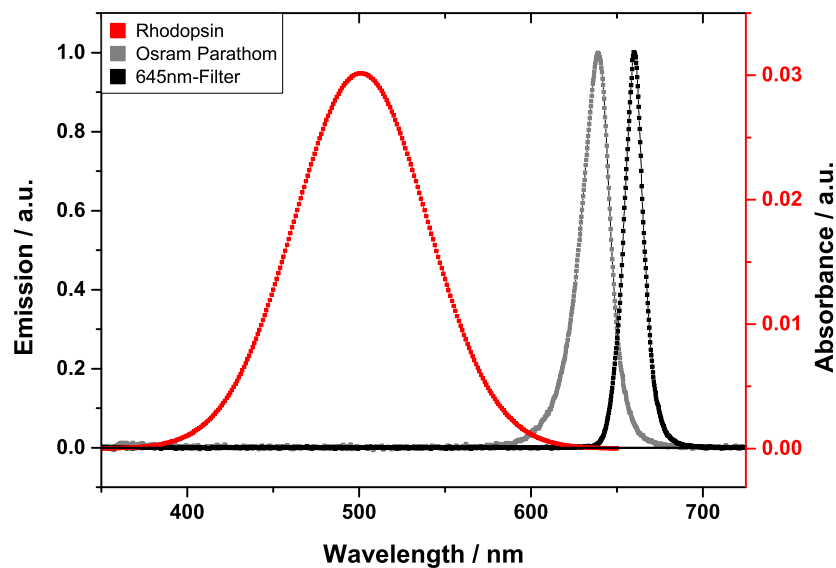


Figure 2.2.: **Emission spectra of dissection lamps**

The commercially available light bulb Parathom (OSRAM; grey dotted line) has its emission maximum at 640 nm, whereas the custom-build lamp, equipped with an optical filter at 645 nm, has a dominant wavelength of 660 nm (black dotted line). For a better comparison, the absorbance spectrum of dark-adapted rhodopsin is also plotted (red dotted line). The spectra of the Osram bulb and rhodopsin overlap. The spectral overlap between the custom-build lamp (645 nm cut-off filter) and rhodopsin is only 8% of the overlap between the Osram bulb and rhodopsin.

Rhodopsin absorbs light around 500 nm (Wald and Brown, 1953), in the range of green light. Using red light for the preparation of samples containing rhodopsin diminishes its bleaching. The lamp equipped with the Osram Parathom light bulb has a dominant wavelength of 640 nm, where dark-adapted rhodopsin still absorbs a small amount of light. Because of that, this red light lamp was only used for indirect room lighting and avoided for direct handling of the retina. For the handling of the eye or the retina, only the custom-build red-light lamp was used. Due to the marginal overlap between the emission spectrum of the lamp and the absorbance spectrum of dark-adapted rhodopsin, any bleaching effect of the illumination during preparation can be ruled out.

After a short sedation with isofluran (Forene; Abbvie), the mice were killed by cervical dislocation. The eyes were removed using fine scissors and placed in phosphate-buffered saline (PBS) or in case of experiments in Ringer's buffer. For solubilization of rhodopsin, the PBS was supplemented with 20 mmol/l hydroxylamine.

Table 2.2.: Content of the phosphate-buffered saline (PBS)

Concentration	Component
137 mM	NaCl
2.7 mM	KCl
10 mM	Na ₂ HPO ₄
2 mM	KH ₂ PO ₄
pH 7.4	

The retina dissection was carried out using a binocular microscope (C-PS, Nikon). The mouse eye was held with tweezers and punctuated with a Sterican needle (24G, B. Braun) to release the natural pressure of the eye. The eye was opened by cutting equatorial along the *ora serata*. The lens was removed and the eye cup inverted. As a result, the retina was set free and could be easily removed with the help of forceps. It was taken

Table 2.3.: Content of the Ringer's buffer

Concentration	Component
130 mM	NaCl
3.6 mM	KCl
2.4 mM	MgCl ₂
1.2 mM	CaCl ₂
10 mM	HEPES
20 nM	EDTA
pH 7.4	

care to remove the retina intact and completely. To facilitate further handling it was cut four times, like a cloverleaf.

2.6. Solubilization of rhodopsin

The retina was dissected in PBS, supplemented with 20 mmol/l hydroxylamine (438227, Sigma-Aldrich). If illuminated retinal samples were analysed, the illumination of the intact retina was done before doing the actual solubilization. Illumination was carried out in a way that the ganglion cell layer of the retina faced the incident light, like in the living eye. The dissected retina, swimming in buffer, has a natural curvature of the tissue.

To flatten the retina, it was necessary to cut it at four to six positions, somehow like a cloverleaf. The cut retina still curls if it stays without any support. To flatten it and to keep it flattened, it was first transferred to a mixed cellulose membrane filter (HATF, 0.45 µm pore size, Merck Millipore). After transfer, secondly, the retina was gently vacuumed and thereby fixed onto the filter. It was taken care that the retinas did not dry out during this procedure, depicted in Fig. 2.3. This gentle suction on the retina was performed with a peristaltic pump (Reglo Digital, Ismatec). Excess of filter paper surrounding the retina was cut away with a scalpel (type 22, Braun).

The retina on the filter paper was illuminated. For illumination, the retina piece

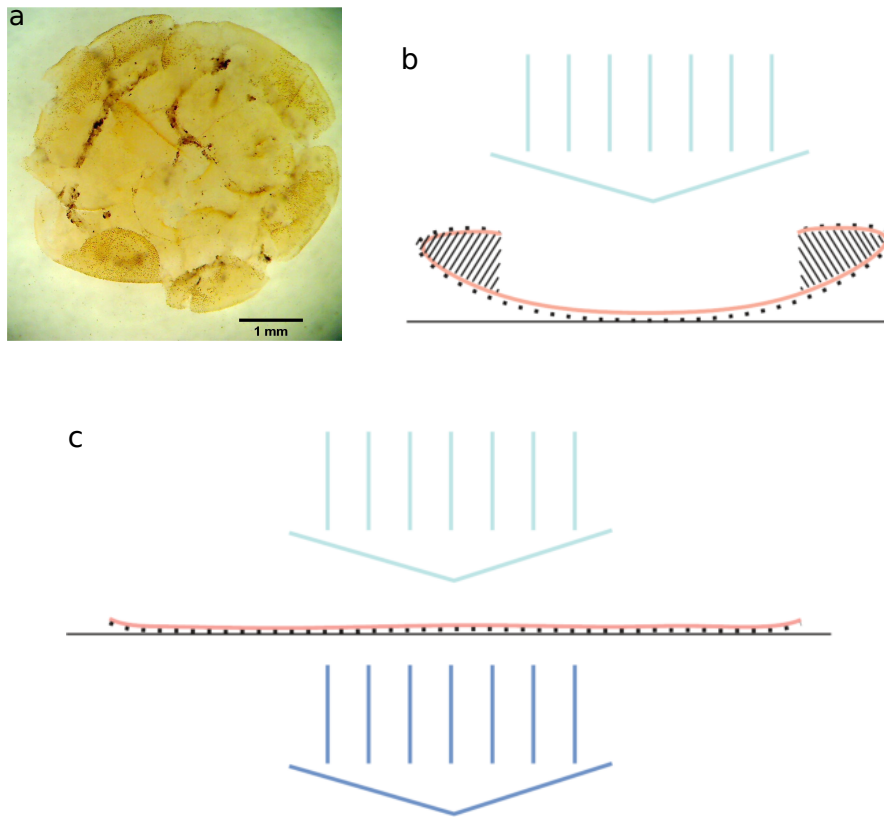


Figure 2.3.: Flattened retina as a prerequisite for illumination

a) Without further processing, the dissected retina stays curved. b) The remains of RPE (black dots) on the outside of the retina (pink) block incoming light (cyan). Hatched areas indicate this shadowing effect. The retina is then as a consequence not evenly exposed to the illumination. A reliable quantification would not be possible. c) Gentle suction (blue) was applied to the retina to flatten it.

was held by forceps on a custom-made forceps stand with a distance of 2 cm to the lamp. Any excess of buffer was taken up with a filter paper (type MN 615, Macherey-Nagel) before the retina was shock frozen in liquid nitrogen.

For specifications of the illumination lamp, see section 2.6.3. Illumination times are collected in Tab. 2.4. For solubilization of dark-adapted samples, the detailed procedure of the retina handling was kept the same – except for the illumination step.

Table 2.4.: Illumination times used to quantify the bleaching of rhodopsin

<u>Illumination time</u>
0 ms
20 ms
50 ms
100 ms
250 ms
500 ms
3 s
10 s
18 s
26 s

Until use, the frozen retinas were kept, wrapped light-tight with aluminum foil, at -80°C . The frozen retina was thawed on ice and supplemented with $500\ \mu\text{l}$ of solubilization buffer. Solubilization was done by successive steps of sonification and shaking. After a first sonification (3 min, on ice; sonifier 450, Branson), the sample was shaken for 5 min at 4°C on the thermomixer comfort (Eppendorf). The second sonification was followed by a shaking period of 15 min. Subsequently, the retinal extract was centrifuged (20 min at $100.000\ \text{g}$, 4°C ; Optima MAX-XP Ultracentrifuge with rotor TLA-55, Beckman Coulter), to pellet any cell debris, organelle or filter paper residue. The supernatant contained the solubilized rhodopsin and one could proceed with the spectroscopic measurement of the rhodopsin content (see section 2.6.4).

2.6.1. SDS-PAGE and Western Blot

The retinas were dissected as previously described. $250\ \mu\text{l}$ solubilization buffer was added and samples sonified for for in total 120 s. At the timepoints 0 s, 15 s, 30 s, 45 s, 60 s,

Table 2.5.: Content of the solubilization buffer

Concentration	Component
10 mM	HEPES
0.5 mM	EDTA
20 mM	NH ₂ OH
1%	DDM
1/500	mPIC
	mammalian Protease Inhibitor Cocktail (Sigma Aldrich)
	pH 7.4

90 s, and 120 s, 15 μ l aliquots were taken to subsequently load two SDS-PAGE gels. Prior to loading, 4x loading buffer was added and the aliquots incubated at 95°C and 1000 rpm for 5 minutes. Electrophoreses with two 5-10% SDS-PAGE gels were performed (30 - 40 mA, runtime 1.5 h). Protein marker VI (10-245 kDa, A8889, AppliChem) was among the samples loaded. For coomassie staining of one SDS-PAGE colloidal coomassie was used (lab intern recipe). Destaining was performed by adding 1% acetic acid, the coomassie gel was boiled up (45 - 60 s) and cooled down (at 4°C), repetively. At the beginning of each destaining round, old destain was discarded and fresh acetic acid added. Destaining was performed for about 1,5 hours. The second SDS-PAGE was used for the semidry transfer (Western Blot) to a PVDF membrane (Immobilan P, Merck Millipore). Blotting was done at 170 mA for 40 min (2.4 mA/cm). The PVDF membrane was incubated in 2.5% milk powder (in PBST). PBST is PBS supplemented with 1% Tween 20 (9127.1, Carl Roth GmbH). After rinsing the membrane in PBST, it was incubated with polyclonal antibody rabbit α Rhodopsin (H-300, sc-20139, Santa Cruz Biotechnology) with a dilution 1:200 in PBST. After two rounds of washing in PBST (each 10 min, shaking) the membrane was incubated with donkey α rb-HRP 1:5000 in PBST. Another four rounds of washing in PBST (each 10 min, shaking) were followed by a 3 min incubation with ECL Western Blotting detection reagent (AppliChem). Chemiluminescence was detected with KODAK BioMax

light film (Kodak).

2.6.2. Different detergents tested

Digitonin and Triton X-100 were used for preliminary experiments, but they were considered as not suitable (see section 3.1.2). DDM is better suited for the solubilization of membrane proteins than Triton X-100 (Fong et al., 1982), because it keeps lipid-protein interactions intact. Rhodopsin, solubilized with DDM, is thought to be less destabilized than prepared with a rather harsh detergent like Triton X-100 (personal communication with Prof. Pere Garriga; Seddon, Curnow, and Booth (2004)).

2.6.3. Illumination quantification achievable with high-power LED

For the illumination of the retina samples, a high-power LED (M505D2, Thorlabs) was chosen to minimize the time needed to get a full-bleached state of initially dark-adapted rhodopsin. The emitted light has a cyan color to match with rhodopsin's absorbance wavelengths. The emission spectrum of the cyan high-power LED is shown in Fig. 2.4.

As Fig. 2.4 shows, the emission spectrum of the high-power LED nicely overlaps with the absorbance spectrum of rhodopsin.

Parallel illumination over a range of 2.5 cm was ensured by attaching a convex lens to the LED. During the illumination experiments, the high-power LED was cooled passively, mounted on a solid metal block. Mounting and assembly of the lamp was carried out with the help of Dr René Pascal. The LED was triggered by a voltage of 4.9 V, but limited to a current of 950 mA by using an interconnected constant current transmitter (Konstanter SSP 240-20; Gossen-Metrawatt). Overheating of the LED would lead to an altered current, therefore, these parameters were checked intensively before and after

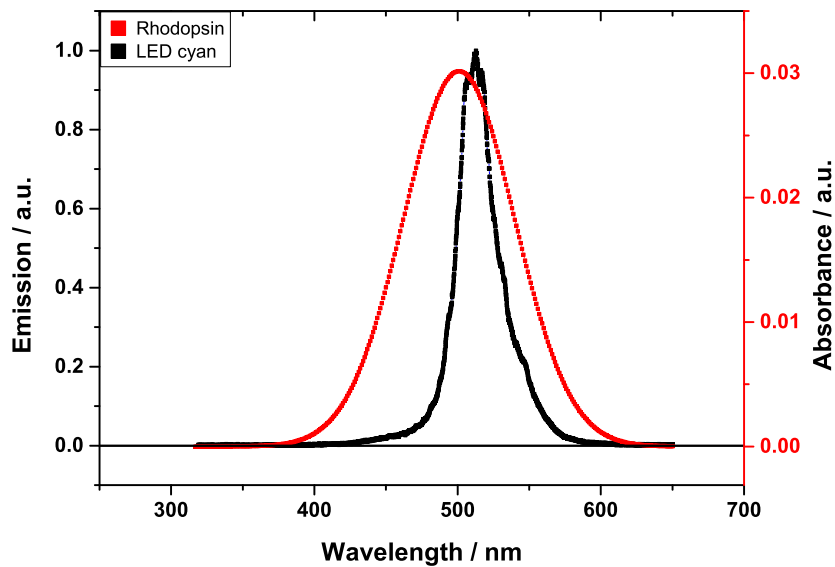


Figure 2.4.: Emission spectrum of the cyan high-power LED and absorption of dark-adapted rhodopsin

The cyan high-power LED has a dominant peak at 505 nm and entirely emits in the spectral range, where rhodopsin absorbs photons and thereby bleaches. The wavelength, where rhodopsin absorbs at most is 500 nm. Thorlabs provides the emission spectrum of the LED M505D2 online. For comparison, also the absorbance spectrum of dark-adapted rhodopsin was plotted.

each measurement. This custom-built lamp, equipped with the high-power LED and a high-speed timer, enabled a full-bleaching of the rhodopsin, still embedded in its native environment, within a comparable short time (see also Tab. 2.4). To keep the handling time of the retina as short as possible, diminishes the risk of degradation of rhodopsin. Fig. 2.5 shows the experimental setup.

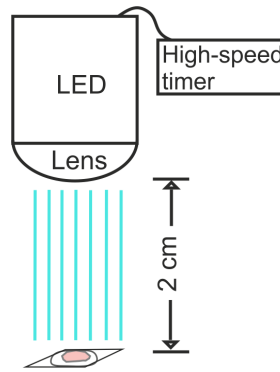


Figure 2.5.: **Experimental setup for illumination with high-power LED and high-speed timer**

The retina (pink), which was sucked flat on filter paper (white; see also section 2.6) were placed in a two centimeter distance below the high-power LED. The high-power LED was equipped with a high-speed timer to allow even short illumination times in the millisecond-range.

2.6.4. Optical measurement of solubilized rhodopsin

Upon illumination, rhodopsin isomerizes several times within the visual cascade. Each of the involved intermediates shows a different absorbance (a nice overview is given in Palczewski (2006)). The knowledge of this behaviour is a prerequisite for the optical measurement of the bleaching effect on rhodopsin.

The spectrophotometric measurement was carried out with the spectrophotometer Varian Cary 5000, which is capable of doing spectrophotometry in the UV, visual, and near-infrared range of light. 200 μl of the supernatant were pipetted into an absorption quartz cuvette (Z600318, Hellma) and measured using the WinUV-function *Scan*. The absorbance by the retinal extract was measured ranging from 300 to 650 nm, in the range from UV to deep red light. As a reference solution, the pure solubilization buffer was used. Baseline absorbance was subtracted. It was taken care that the measuring window of the cuvette matches with the beam path.

2.6.5. Analysis of rhodopsin spectra

Deconvolution and peak separation of the measured spectra was carried out using the software PeakFit.

The following procedure was applied: To minimize subjective influence by the experimenter the auto function *peak autoplacement for local maxima and residuals* was used. The option Savitzky-Golay smoothing (4.8%) allows to filter out noise caused by the spectrophotometer. Since, proteins absorb light at the dominant wavelength of 280 nm, any value below 315 nm was cut off. An exponential baseline with both tolerance and threshold set to 2% was chosen. Peak widths have not been changed. Two iterative fits were done.

By this procedure, PeakFit automatically fitted the baseline and recognized three peaks in every data set (see Fig. 2.6). Baseline was fitted exponentially. The nature of the three pigments causing these three main peaks will be discussed in section 3.1.2.

2.7. Isolation of rod photoreceptors and outer segments

Ten retinas were dissected according to the above mentioned procedure and placed in 100 μ l Ringer's buffer. ROS were liberated by successive vortexing and centrifugation steps. For this purpose, the retinal extract was gently vortexed (Mixer Uzusio VTX-3000L; LMS) for 1 min and centrifuged (Biofuge fresco; Heraeus) for 1 min at 380 g. The supernatant prepared that way mostly contains pure rod photoreceptors, but a lot of rods still remained in the pelleted tissue. Adding 100 μ l of buffer to the pellet,

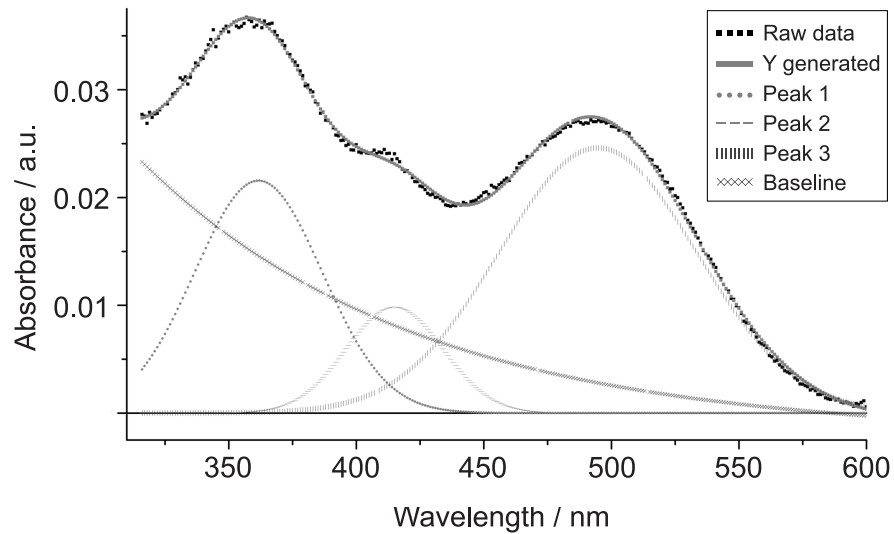


Figure 2.6.: **Deconvolution and peak separation with PeakFit**

Raw absorbance spectrum of a solubilized dark-adapted retina (black dots). PeakFit automatically separates the raw spectrum in three main peaks (grey dotted and dashed lines). The exponentially fitted baseline is plotted, as well (grey crosses). For details of the components causing the three different peaks, see the section 3.1.2.

vortexing, and pelleting was repeated eight times to further release rods or ROS out of the tissue. The supernatants were collected and ROS sedimented by centrifugation (5 min, 1000 g). The ROS pellet was mixed with either 20 μl dextran (40 kDa, Carl Roth) for high-pressure freezing (see section 2.9.1) or 100 μl Ringer's buffer to reach a cell concentration of about $2 \cdot 10^9$ ROS/ml for plunge-freezing (see section 2.9.2). ROS were counted using a hemocytometer (type Neubauer), as exemplarily shown in Fig. 2.7. In this way, ROS suspensions of $5 - 6 \times 10^5$ ROS/ μl could be achieved. For reference see Bader, MacLeish, and Schwartz (1978) and (RN Lolley and Racz, 1986).

2.8. Isolation of ROS disk membranes

The isolations of ROS disk membranes for subsequent AFM experiments were carried out by Dr Christoph Brenker. Isolation of ROS disks and subsequent examination by

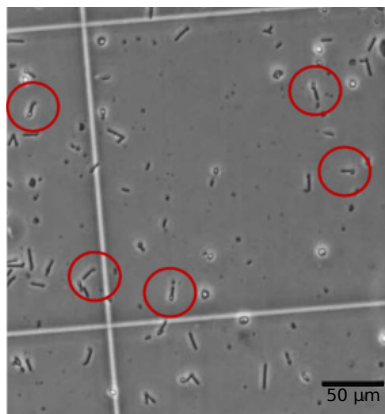


Figure 2.7.: **Counting of ROS after isolation**

Isolated ROS are counted using a Neubauer hemocytometer, imaged at 100x magnification. Individual ROS were circled as examples for better illustration.

AFM is intended as a repetition of the AFM experiments performed by Liang et al. (2003) and Liang et al. (2004).

20 Retinas, collected in 120 μ l 8% Optiprep (Sigma Aldrich) in Ringer's buffer, have been mildly vortexed for 1 min. The retinal extract was centrifuged (200 g, 1 min) and the ROS containing supernatant collected. Adding of 120 μ l 8% Optiprep/Ringer's buffer, vortexing, and centrifuging was repeated six times. Supernatants were pooled and any cell debris sedimented by centrifuging at 500 g (3 min). Only the supernatant was processed further. After centrifuging and thereby sedimenting the ROS (30 min, 26,500 g), the ROS were burst osmotically. Therefore, the pellet got dispensed in 2 ml of 2 mmol/l Tris/HCl (pH 7.4) and incubated over night at 4°C. The ROS extract was pelleted (full speed) and dissolved in PBS. Isolated ROS disks were used directly for AFM studies or frozen at -20°C until use. This experiment was intended as a preliminary test, therefore preparation time was kept short. One can additionally purify the disk suspension via an optiprep gradient, if needed. Isolated ROS disks can also be used for High-pressure freezing or plunge-freezing.

2.9. Cryo-fixation

In the field of electron microscopy, there are many possibilities to fix and harden the sample of interest for subsequent ultramicrotomy. Using fixatives (glutaraldehyde or paraformaldehyde) together with dehydration and resin embedding (acrylates or epoxy resins) causes preparational artifacts and structural alterations within the sample. To preserve the native state of a tissue, cell, or the protein of interest, the best choice is to cryo-fix it.

For cryo-preservation, a tissue sample can be frozen under pressure to allow vitrification, using a technique called high-pressure freezing (HPF). HPF was established by Moor and co-workers (Moor and Hoehli, 1970; Moor et al., 1980).

During vitrification, an aqueous solution will become amorphous instead of forming crystalline ice. HPF is capable of vitrifying a sample up to a thickness of 200 μm , with less yield even 250 μm . The vitrification depth depends on the kind of tissue that is frozen. Additionally, also the composition of the cryo-protectant used matters. The cryo-protectant helps to get the sample vitrified homogeneously. Sartori and co-workers had good results using 20% sucrose, mannose, or dextran as a cryoprotectant for freezing catalase crystals (Sartori, Richter, and Dubochet, 1993). However, a sample with an intrinsic cryo-protective activity may even partially vitrify up to 500 μm (Studer, Michel, and Müller, 1989; Lučić, Rigort, and Baumeister, 2013). These feasibility constraints allow us to use high-pressure freezing to vitrify intact retinas with a tissue thickness of about 200 μm . Subsequently to the cryo-fixation, an ultramicrotome is used to create ribbons of ultrathin sections, which can be transferred to and imaged in the transmission electron microscope (TEM).

A sample which is thinner than 10 μm (cell suspensions, viruses, or isolated proteins) can be vitrified via plunge-freezing (Dubochet et al., 1988). The sample can directly be applied to EM support grids. A plunge-frozen sample does not require further ultrami-

crotoomy and can be directly imaged in the TEM or further thinned with the focused-ion beam (FIB). This cryo-fixation method is suitable for ROS suspensions.

The vitrified sample must always be kept below a temperature of -137°C to avoid devitrification (thawing) (Dubochet et al., 1988; Al-Amoudi, Dubochet, and Studer, 2002).

2.9.1. High-pressure freezing

The procedure to vitrify the intact retinal tissue by high-pressure freezing was established in our lab by Dr Monika Gunkel (Gunkel et al., 2015). The work was done in the dark. In the following the experimental procedure of the current study, based on previous findings, is described in detail. The dissected retina was cut into smaller pieces ($0.5\text{-}1\text{ mm}^2$), transferred to a drop of cryoprotectant, and incubated for 5 min. The cryoprotectant contained 20% dextran (40 kDa, Carl Roth) and 5% sucrose (Carl Roth). Sucrose is osmotically active. One needs to add sucrose to the cryoprotectant to get the inner layers of the tissue preserved, as well as the outer layers. Subsequently, the retina piece was layered into a HPF carrier (either type 665 or 662, Engineering Office M. Wohlwend). These carriers are gold coated copper specimen supports for the freezing process. The first carrier was covered by placing a second carrier on top of it (type 663 or 662). The second carrier was coated with 0.5% phosphatidylcholine (P3556, Sigma Aldrich) solubilized in chloroform to facilitate the later splitting of both carriers. Samples for cryo-sectioning were frozen in type 665 carriers. These carriers have equal indentations ($150\text{ }\mu\text{m}$) on both of their sides. They have been covered with the flat side of type 663 carriers (one side flat, one side with $300\text{ }\mu\text{m}$ indentation); see also Fig. 2.13a)). Not only samples for cryo-ultramicrotomy were frozen, but also samples designated for

freeze- fracture experiments. These samples, meant for doing freeze fracture experiments, were frozen in 662 type carriers (200 μm and 100 μm indentation respectively), forming a carrier sandwich. For placing the retina piece inside, as well as for covering, the 100 μm indentation has been used – that results in a total space of 200 μm inside the carrier sandwich (see also Fig. 2.13b)).

Any intended illumination was applied onto the retina piece already placed inside the lower carrier. The distance between the retina piece and the illumination lamp was 2 cm, like for rhodopsin solubilization experiments described above. Carriers for freeze-fracture were not illuminated. After transfer of the carrier sandwich to the sample cartridge of the high-pressure freezer EM HPM100 (Leica Microsystems), the freezing process was started. With a cooling rate of 25-30,000 $^{\circ}\text{C}/\text{s}$, the retina sample was vitrified within ms by flushing of pressurized liquid nitrogen into the sample cartridge. The frozen carriers subsequently were punched out of the sample cartridge middle plates and stored in liquid nitrogen until use.

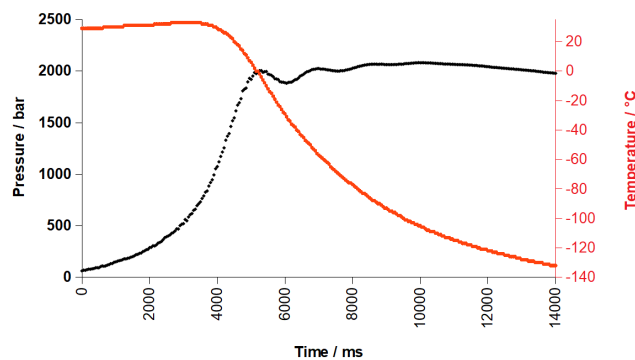


Figure 2.8.: **Freezing parameters during HPF**

During high-pressure freezing of retinal samples, the pressure (black) rises), whereas the temperature decreases (red).

Usually, ROS samples were plunge-frozen, because they are thin enough for this cryo-fixation method. Thereby, as elongated cells the ROS will usually be oriented parallel to the grid support – giving us a longitudinal view of the contained disks. However,

to get a cross view on the surface of one disk within the intact ROS, ROS samples got high-pressure frozen and sectioned at the cryo-ultramicrotome, as well. To high-pressure freeze isolated ROS, the cellular pellet was resuspended in an equal volume of 40% dextran (yielding a cellular concentration of about $5 \cdot 10^9$ ROS/ml) and pipetted directly into the lower HPF carrier. Sucrose within the cryoprotectant is not needed, as well as any additional incubation time.

2.9.2. Plunge-freezing

Instead of high-pressure freezing, isolated ROS can also be vitrified via a process called plunge-freezing (McDowall et al., 1983; Adrian et al., 1984).

For freezing, either the plunger Vitrobot Mark IV (FEI) or EM GP (Leica Microsystems) was used. In table 2.6 typical settings for plunge-freezings are collected.

Table 2.6.: Typical settings for plunge-freezing ROS

Parameter	Vitrobot	EM GP
Humidity	100%	80%
Temperature	4-22°C	22°C
Blotting force	15	sensor
Blotting time	> 7 s	7-10 s
Blotting type	backside	backside
	pre-wetted grid	
Blotting paper	Whatman type 4	Whatman type 2

Grids for plunge-freezing were glow-discharged for 2 min (MED010, Bal-Tec) before use to make them more hydrophilic. Per grid 3 – 5 μ l of the ROS extract ($0.3 - 1 \cdot 10^9$ ROS/ml) were applied on the front side of the grid (carbon film side). During the blotting process, filter papers (type 2 and 4, Whatman) touch the grid and absorb any excess of liquid, leaving a thin aqueous film on the grid. Whatman filter paper type 4 absorbs liquid very fast (20 μ m pores, rate: 37 s/100 ml, according to the sigma aldrich catalogue), whereas

type 2 paper absorbs liquid much slower (8 μm pores, rate: 240 s/100 ml, respectively), which is much more suitable for the reproducibility of the blotting process. During this study, the type of filter paper has been changed for that reason. Backside-blotting means that only a filter paper on the backside of the grid was used. This procedure is more gentle than touching the front side of the grid with blotting papers – the chance the fragile film stays intact is higher for backside blotting. For backside blotting the grid needs to be pre-wetted with buffer to allow liquid transport to the filter paper. In the following step, the grid will be plunged in liquid ethane. Here, again, the sample is vitrified within ms.

With these settings, I achieved the creation of a thin ice film with sufficiently homogeneously spread cells. However, ROS typically have a diameter of one μm . This thickness is much too high for analysing it with a TEM – the vitrified sample cannot be imaged directly and needs to be thinned further with a FIB (see section 2.15).

Plunge-freezing of isolated ROS disks was performed solely with the Vitrobot Mark IV. At this time, the plunge-freezer was located in a normal lab, which is not a designated dark room. The lab was darkened as much as possible, however not every illumination source could be ruled out, though. Therefore, the samples are considered to be retrieved at low-light conditions. Even, if they are not perfectly dark-adapted, they can serve to find the optimal preparation conditions. 45 μl of the ROS disk sample got mixed with 5 μl Protein A gold (Cell Microscopy Core – CMC; University Medical Center Utrecht) and plunge-frozen in low-light conditions. The protein A gold served as fiducial markers, which facilitates the processing of a tomogram after acquisition. For light microscopy, these fiducials are fluorescent. For electron microscopy, these fiducials are round, small (1-20 nm) metal particles with a high electron density. For this function, the protein A tag on the gold particles does not matter – a pure gold solution would have been sufficient. However, a gold chloride solution was not used, because its tendency for clumping.

The parameters used for blotting are given in table 2.7.

Table 2.7.: Typical settings for plunge-freezing ROS disks

Plunge-freezer	Vitrobot
Humidity	100%
Temperature	4°C
Blotting force	0
Blotting time	> 9 s
Blotting type	two-side
Blotting paper	Whatman type 4

For blotting, two filter papers (one on every side of the grid) were used.

Plunge-frozen samples were stored in liquid nitrogen until use.

2.10. Cryo-sectioning and processing of the grids

To obtain samples, sufficiently thin for analysis with TEM, the HPF carrier was sectioned with an ultramicrotome (UC6 or UC7; Leica Microsystems), equipped with a cryo chamber (FC6 or FC7; Leica Microsystems), set to -160°C. Again, the procedure to section retinal samples and to apply fiducial markers onto the sections was initially established in our lab by Dr Monika Gunkel (Gunkel et al., 2015).

In the following, the sectioning procedure is described in detail. The carrier was placed in the flat specimen holder (Leica Microsystems; modified by in-house workshop to have a carrier slot). The first sectioning step was the trimming of a pyramidal sample block suitable in size to section a long ribbon of ultrathin sections. For the trimming, a diamond trimming knife (Cryo-trim knife 20, angle 45°; Diatome) was used. Parameters for trimming were the following: If trimming copper parts of the carrier, a feed (section thickness) of 250 nm and the maximum speed (100 mm/s) was set. For trimming of dextran or tissue, the feed and speed were reduced (down to 60 nm at 60 mm/s). A

clearance angle (angle between knife and sample block) of 6° was set.

The knife edge of the diamond sectioning knife (cryo immuno knife, angle 35°; Diatome) is sharper than for the trimming knife. One has to pay more attention to not demolish the knife edge. Sections were usually made with 40-50 nm feed and 1 mm/s speed. If the ribbon had a length of 1-2 mm, it was attached to a holey carbon filmed copper or gold grid (R2/1; Quantifoil) with the help of an ionisator (Crion antistatic device; Leica Microsystems).

Due to the sectioning process, sections are prone to many artifacts (Al-Amoudi, Studer, and Dubochet, 2005). First, knife marks resulting from minor variances at the knife edge. These artifacts are oriented in the cutting direction. Second, friction of the block on the knife edge leads to crevasses on the top side of the section. Compression, as another artefact, is caused by the bending of the section while it's being sectioned. Friction of the section on the knife surface also increases compression. At last, thickness variations of sections are called chatter. Presence and amount of cutting artifacts are influenced differently by the sectioning parameters. The above mentioned sectioning parameters are a good compromise to obtain sections which are affected least by artifacts.

Here, as well as for the plunge-freezing of disk membranes, fiducial markers were placed onto the grids. The specialty in this case was, that the fiducial labelling had to be done below the critical devitrification temperature (-137°C, Dubochet et al. (1988) and Al-Amoudi, Dubochet, and Studer (2002)) to avoid thawing of the sample. Furthermore, an aqueous solution with gold particles for example would be hardened at this temperature and could not be used for this reason. The best choice was to use a quantum dot solution (5 mg/ml PbS Core EviDots in toluol, ED-P20-TOL-0850, Evident Technologies), as proposed by Masich *et al.* (Masich et al., 2006). The quantum dots were diluted 1/50 with isopentane (2-Methylbutane; Carl Roth) to a final concentration of

2%. The quantum dot dilution stays liquid down to a temperature of -145°C . However, because it freezes at lower temperatures, this temperature was chosen for the labelling process. The grid was shaken for 30 s in the quantum dot dilution and washed for at least 2.5 min in liquid ethane. Any excess of liquid ethane was absorbed by a pre-cooled filter paper. After the grid completely drained, it was put back in the storage box.

Before imaging at the TEM, the grids needed to be prepared to be used with the autoloader of the Titan Krios (FEI). The Titan Krios makes use of a special sample cartridge and the so-called autoloader, which is able to load and unload samples automatically. To be handled by the autoloader, the grids need further support. Therefore, each grid was placed inside a metal ring (autogrid; FEI) and fixed with a metal spring (C-clip; FEI).

2.11. Cryo-electron microscopy and tomography

Light microscopy comes to its fundamental limits when you want to analyse intracellular details. Synaptic transport or sensing processes remain exclusive to the experimenters eye because they are much smaller than the resolution limit of light microscopy. According to Abbe's equation, with visible light only details down to approximately 200 nm are resolvable.

$$d = \lambda/2NA \quad (2.1)$$

The diffraction limit d is defined by the ratio of the wavelength (λ) to twice the numerical aperture ($2NA$). NA itself is defined by the product of the refractive index (n) and the sinus of the angle (δ).

$$NA = n\sin\delta \quad (2.2)$$

Because the wavelength of electrons is shorter than of visual light a higher resolution is achievable using a microscope with an electron source.

Ernst Ruska's and Max Knoll's groundbreaking work on the first electron lens in 1931 set the base for the invention of the first electron microscope (Ruska, 1934).

An electron microscope (EM) is operated with high energy. Electrons, released from a cathode, are accelerated by the Wehnelt cylinder. In the simplest case, a cathode could be a thermionic cathode. In the EMs used in this study, a Shottky emitter serves as electron source. Shottky emitters are a special type of field emission guns - a high voltage is used that electrons are tunnelling out of an emitter made out of tungsten - this process is aided by heating.

An electron microscope principally consists of similar parts compared to a light microscope: After emission, the light passes several lenses, condenser and objective lenses, until it is detected. In contrast to the light microscope, EM lenses are electromagnetic or electrostatic. Furthermore, the detector is a fluorescent screen, coupled with a scintillator, or a photographic plate.

Earlier in the development of EMs it was necessary to use a fluorescent screen, positioned within the EM, to monitor EM images. This screen is still in use, nowadays - an internal camera captures these images, which are then digitally displayed on the experimenters computer screen. However, high-precision EM images are detected with an additional detector using CCD (Charge Coupled Device; line-readout) or CMOS (Complementary metal-oxide-semiconductor; single-pixel reading) chip. A direct detector like the Falcon II (FEI, Hillsboro, USA) as it is used in the Titan Krios is coupled to a CMOS chip. In contrast to CCD chips, a CMOS chip has a greater performance at higher energies of, for example, 300 keV as necessary for tomography of biological samples. A CMOS chip is determined by a greater DQE (detective quantum efficiency), the square of the output (SNR_o) to input (SNR_i) signal-to-noise ratio (McMullan et al., 2014).

$$DQE = SNR_o^2 / SNR_i^2 \quad (2.3)$$

Direct detectors do not contain scintillators, anymore. Scintillators are made of materials that are able to scintillate, when excited by radiation like the electron beam in the electron microscope. Scintillators may reduce the DQE and thereby the possible resolution (Meyer and Kirkland, 1998). Furthermore the falcon II is back-thinned. According to FEI, this increases the spatial resolution of the acquired images further.

2.11.1. Transmission electron microscope

Grids prepared via sectioning or thinning with the FIB are transferred to the electron microscope, the Titan Krios, and imaged. Because of combining ultrathin sectioning and electron microscopy, the technique is also called cryo-electron microscopy of vitrified sections (CEMOVIS). Grids, already mounted into autogrids, were inserted into the Titan Krios (FEI, Hillsboro, USA) sample cartridge. These cartridges have 12 sample slots. The transfer was done using the transfer box of the Titan Krios, which diminishes ice contamination, if used properly. The Titan Krios cartridge is loaded into the NanoCap – a small sample dewar for transfer to the TEM – and, subsequently, into the autoloader of the Krios. The TEM is capable of the automatic recognition of the grids inside the sample slots of the cartridge. The Titan Krios TEM (FEI, Eindhoven, Netherlands) was operated at 300 kV. The microscope was aligned and calibrated using a crossgrating sample (Plano, Wetzlar). This was regularly done during instrument service by Dr Stephan Irsen. The Titan Krios was equipped with the direct electron detector Falcon II (FEI). Chip and image size are 4k x 4k. The Falcon II was located behind the Gatan imaging filter (GIF), the Titan Krios is equipped, as well. Low magnification images were recorded for scanning for regions of interest (ROIs). Some prerequisite are necessary for tomogram acquisition. Cryo-sections need to be fully attached to avoid sample movement. After finding a suitable ROI for tomogram acquisition, the sample was tilt in

every direction up -65° and $+65^\circ$ to assure this is a putative good position. However, as this is only a prediction - the sections may move later on during tomogram acquisition. Tomograms then were discarded.

Image acquisition was done with tomo4 (FEI) and SerialEM (Mastronarde, 2005). The defocus was set to -4 or $-5 \mu\text{m}$. Magnifications of 14,000-18,000 were chosen. Gatan energy filter (GIF) was not used. An electron dose of $80\text{-}100 e^-/\text{\AA}^2$ for one single tomogram was set. During tomogram acquisition, the sample stage was tilted from $-60\text{-}65^\circ$ to $+60\text{-}65^\circ$ as illustrated in Fig. 2.9a. A so-called continuous tilt-scheme was used (Hagen, Wan, and Briggs, 2017). Tilt increments of 2° were chosen.

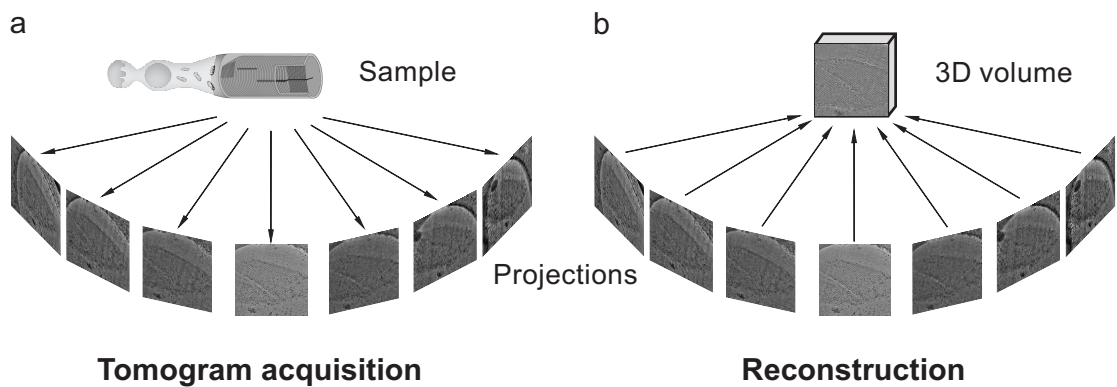


Figure 2.9.: **Workflow of cryo-electron tomography**

(a) Acquisition of a tomogram from a ROS. The illustration of the ROS is taken from Gunkel (2013). The sample is tilted from $-60\text{-}65^\circ$ to $+60\text{-}65^\circ$ with 2° -increments during acquisition. Single projection images are exemplified. (b) Subsequently, a 3D volume can be reconstructed via combining and aligning the single projection images. Further processing may involve subtomogram-averaging (Al-Amoudi and Frangakis, 2013), as well.

The illustration of tomography was inspired from Lučić, Förster, and Baumeister (2005).

2.11.2. Dual-axis tomography

With every tomography, not all tilt angles are covered and corresponding projections recorded. Due to the construction limits of every electron microscope, the experimenter loses about 30% of information – depending on the tilt range with which tomography is done (Lučić, Förster, and Baumeister, 2005). This lost information is called the *missing wedge*. The amount of missing information can be reduced by performing dual-axis tomography. The Titan Krios is able to rotate the sample stage for 90° horizontally. The rotated stage can also be tilted from -60-65° to +60-65° – that means dual-axis tomography can be performed.

For doing dual-axis tomography, first a normal tomogram was recorded. However, instead of using 69-100 $e^-/\text{Å}^2$ for one single tomogram, here only 40-50 $e^-/\text{Å}^2$ were used for the recording of one axis. That means for every dual-axis dataset, in total the same beam intensity was used. For the dual-axis tomography, sections of 40-100 nm thickness were prepared. Acquisition was done manually with SerialEM. This is done, because the FEI software, without the ATLAS tool, could not be used to find back the rotated position. Otherwise, SerialEM is not able to record a batch of tomograms automatically. Magnifications of 8,700-15,000 were chosen. Gatan energy filter (GIF) was used.

2.12. Data-processing

Data obtained via tomography or simulations needed to be processed further.

During data processing, the single projections (images from every stage tilt) are recombined to the full 3D volume – the tomogram is reconstructed (see also Fig. 2.9b). Reconstruction was carried out with IMOD 4.7.15 (Mastronarde, 1997). In the following,

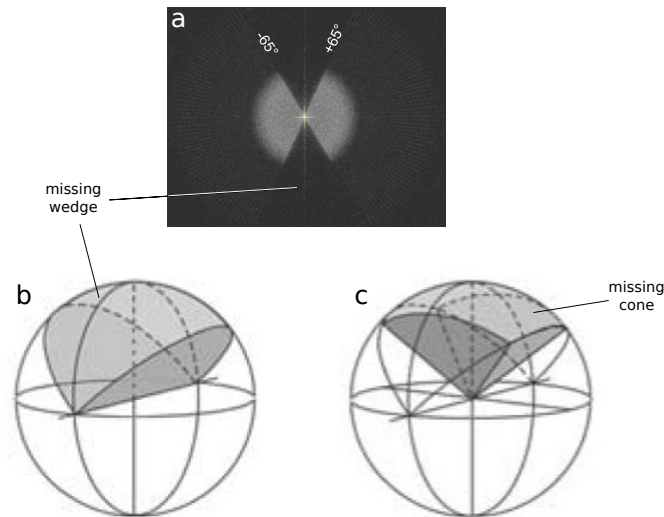


Figure 2.10.: **Diffraction pattern, missing wedge and missing cone – a comparison of single- vs. dual-axis tomography**

A) The diffraction pattern from one tomogram calculated via the Fourier transformation. Diffraction patterns can be used to estimate the resolution of the EM images. The largest diffraction is given by the smallest distances. With this diffraction image, one can see the acquisition limits. Clearly visible is the missing information in triangular shape above and below. Each radial 'line' represents one tilting angle of the acquisition. Every 2 degrees a micrograph was recorded. Here, the tomogram was recorded from -65° to $+65^\circ$. B) In Fourier space the information gathered via normal (i.e. single-axis) tomography is shaped like a wedge – the *missing wedge*. Due to the limited tilting range, these informations cover about 67% of the sample, if it is tilted from -60° to $+60^\circ$ (adapted from Lučić, Förster, and Baumeister (2005)). C) Using dual-axis tomography, more information of the sample can be recorded. After acquisition of the first single-axis tomogram, the sample is rotated 90° in beam direction before the second single-axis tomogram is recorded. In Fourier space a *missing cone* or *pyramid* results from the lost information. Both tomograms combined result in the dual-axis tomogram. It gathered about 84% sample information, if the tilting range is $\pm 60^\circ$ (adapted from Lučić, Förster, and Baumeister (2005)).

the reconstruction methods of the full volumes are discussed. The manual and numerous publications can be consulted, additionally.

During reconstruction as many as possible steps were done automatically using IMOD. The attempt was to adjust as little as possible manually to maintain objectivity of the result. Raw data of tomogram were loaded into IMOD. Single- or Dual-axis has to be chosen according to the tomogram type. Frame type was set to single frame. The header of the tomogram metadata was scanned. A fiducial diameter of 10 nm was set. Com scripts were created. Removal of X rays is not necessary, because data are recorded using a CMOS instead of a CCD chip. During pre-processing, a fixed stack was created and used. For Coarse alignment, a cross-correlation was calculated. The binning for coarse alignment was set to 1 to avoid loss of data. The new stack was converted to bytes and the option *float intensities to mean* was used. Additionally, the storage mode was kept the same as in the input file. After coarse alignment, the fiducial model was generated either by marking of fiducials (*seed model*), if fiducial markers were applied earlier onto the sample, or by patch tracking of internal features. Marks of fiducials could either be set automatically by the beadtracker of etomo or manually by the experimenter. The beadtracker was set to refine the center of the found fiducial with the Sobel filter ($\sigma = 1.5$ for gaussian filtering). When using the seed model, it was taken care that contours cover the full volume in all three dimensions (20–30 contours). Size of patches during the patch tracking method was chosen to be 250 px in x and y . At least two tracking iterations were performed to enhance accuracy. Additionally, contours were broke into overlapping pieces (e.g. 4).

Data obtained via simulation of 3D volumes were reconstructed *fiducialless* – no fiducials were marked and refined.

Any containing fiducial seed or patch were refined during the fine alignment step. Contours and single points were discarded, if necessary (usually with 75% contour points per contour stay or were recentered). After fine alignment, the tomogram needs to be

positioned correctly. Therefore, a tomogram thickness of 800 px was assumed and a tomogram with binning 4 created. Within this coarse tomogram a boundary model needs to be prepared. For this reason, image was flipped to view the volume in Z view. Three positions in Z view were chosen to cover all sample signals. The correct tomogram positioning helps to center the volume to reconstruct within the original full volume (e.g. noise at the border of the full volume is removed). Subsequently Z shift and pitch angles were computed and the final alignment created. For the final alignment, binning was set to 1. The tomogram got generated with back-projection and by parallel processing on three CPUs.

For preparation of this manuscript, single projections were summed up using IMOD and binned two times (if necessary) to enhance contrast.

Segmentation and averaging of sub-volumes (sub-tomograms) can be done to enhance contrast and resolution. This was carried out by Dr Ashraf Al-Amoudi. Segmentation and averaging of tomograms recorded during this study failed.

2.13. Simulation of ROS volume

For setting up the simulated ROS volume we were guided by simulation done by Rullgård et al. (2011), who simulated TEM images of tobacco mosaic virus (TMV) virions. Whereas, Palczewski et al. (2000) published the structure of rhodopsin (PDB: 1F88) in 2000 already, the crystal structure of Okada et al. (2004) was used as a basis for the simulation experiments, because of its increased resolution.

To assess the quality of single-axis and dual-axis tomograms, an artificial volume of three ROS disks, containing two tracks of rhodopsin each, was generated. The program-

ming language used was python. The aim was to transform the crystal structure of rhodopsin (PDB: 1U19; Okada et al. (2004)) - the “perfect sample” - into the “perfect tomogram” - our ideal data set. This the crystal structure was taken as a basic model to build two rhodopsin tracks (resolution 3 Å, dimensions taken from Gunkel et al. (2015)). Figure 2.11 exemplifies the progress. The modelled rhodopsin track is integrated into a membrane patch. This membrane patch was tripled and arranged like a small stack of disks. With the help of Stephan Irsen, EMAN2 was used to generate a tomogram on the basis of this stack. Grey values were normalized (pixel range 0-10,000) and thereby adapted to real data.



Figure 2.11.: **Generation of rhodopsin tracks and integration into membrane**

a) Two rhodopsin tracks are modelled with the crystal structure of rhodopsin. b) Surface representation of the modelled rhodopsin tracks. c) Rhodopsin tracks are embedded into a model of a lipid bilayer. One track of rhodopsin is peeking out of the membrane. Subsequently, it was shifted to be arranged properly fit into the membrane patch.

This “perfect data set” got processed further just like a real recorded tomogram. Figure 2.12 shows the generated tomograms and the reconstruction of the noised simulated tomogram.

For reconstruction see section 2.12 (fiducialless reconstruction). The perfect, simulated data set was integrated into a real data set and compared. In the next step, the perfect

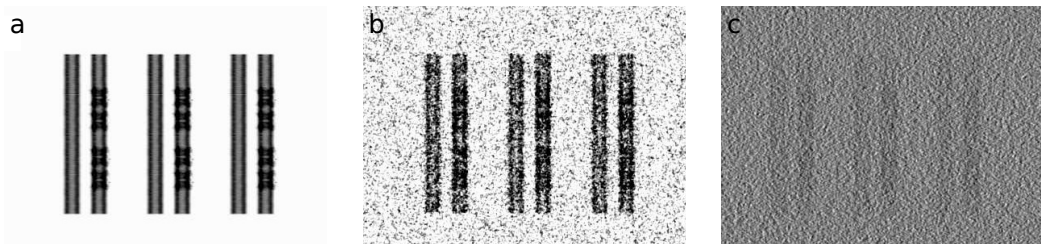


Figure 2.12.: **Generation of simulated tomograms and reconstruction**

a) Generated tomogram without noise. b) Generated tomogram with added Gaussian noise. c) Reconstruction of the noised simulated tomogram.

data set was noised with 5000-fold Gaussian noise, blurred (0.75x), and compared again. Of reconstructed simulated tomograms plot profiles were taken. Therefore, the tomograms were flipped by 90° and 10 slices were summed up via 3dmod (IMOD). A line was drawn with 10 px linewidth via Fiji (ImageJ). Plot profiles along the line were extracted and fitted with PeakFit. As for the analysis of rhodopsin spectra, the auto function *peak autoplacement for local maxima and residuals* was used. Savitzky-Golay smoothing was set to 9.7%, Peak widths were automatically set, and no baseline was chosen. Two iterative fits were done.

2.14. Freeze-fracture and scanning-electron microscopy

An alternative method to gain some insights into the cellular environment is a technique called freeze-fracture, first used by Steere in 1957 (Steere, 1957). A frozen specimen, rapidly ruptured with a sharp knife, breaks preferably along the membranes (Moor and Mühlethaler, 1963). Frozen samples rather act as brittle objects and tend to fracture. Then, they are sectioned by the fracturing knife. Subsequently, the specimen can be further processed by etching and/or shadowing. During etching, the fractured sample is temporarily heated up to -100°C to reveal membrane surfaces. Shadowing means, metal ions (typically from Pt or Au) are applied onto the specimen to decrease charging of the sample during the later imaging. Furthermore, a replica can be produced from

the fractured sample. By sputtering of carbon and metal ions, the specimen surface is completely covered (replicated). The replica can be imaged at room temperature. Severs gives a recommendable overview about the corresponding methods (Severs, 2007). Like Roof and Heuser, we chose to apply the technique on ROS (Roof and Heuser, 1982). However, in contrast to them, we wanted to keep the sample fully vitrified, instead of replicating it. Only full vitrification keeps the sample as native as possible – how we want it to be analysed.

Retina samples, designated for freeze-fracture experiments, were frozen differently as samples, intended to be sectioned. Furthermore, for freeze-fracture experiments, only dark-adapted samples were used. Fig. 2.13 illustrates how the freeze-fracture samples have been prepared as well as the outcome of the freeze-fracture.

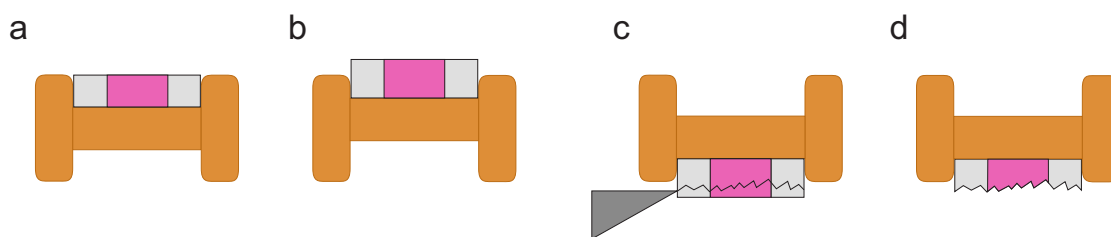


Figure 2.13.: **Schematic illustration of the freeze-fracture**

(a) Carrier frozen for cryo-sectioning. The retina (pink) completely lays inside the 150 µm-indentation of the carrier (type 665; golden), surrounded by cryoprotectant (light-grey). (b) Carrier frozen for freeze-fracture experiments. The retina piece was put into the 100 µm-indentation of the carrier (type 662). For freezing, the carrier was closed with another 100 µm-indentation facing the retina. After removal of the upper carrier (cover), 100 µm of the sample are exposed. (c) During freeze-fracture, the knife (dark-grey) approaches the sample very fast. The sample fractures at the site where the freeze-fracture knife touches the sample. (d) Freeze-fractured sample.

The FF carriers were mounted into the cryo-sample holder within the cryo loading stage (Leica) and transferred using the EM VCT100 (Leica) to the freeze-fracture unit of the coating system MED020 (Bal-Tec). The MED020 was equipped additionally with the multi control system MCS010 and the quartz filter thickness monitor QSG100 to measure

the depth sputtered. The retina sample was ruptured and sputtered with gold at 60 mA.

The fractured sample was imaged under cryo conditions at the Focused-ion beam (FIB, 1540XB, Zeiss) using the implemented scanning electron microscope (SEM). Parameters for imaging were the following: Electron high tension (EHT) was set to 5 kV. The specimen stage was tilted for 54°. The sample was located 3.2 mm away from the electron column (working distance) and imaged at a magnification of 447x. The FIB probe was operated at 30kV:20pA.

2.15. Focused-ion beam

Sectioning artifacts affect the yield of sections suitable for tomography. Furthermore, the yield is decreased additionally by the fact that the sectioned ROS within the tissue need to be oriented in a proper way for acquiring a tomogram. If they are too close to a grid bar or if they are bended within the section, regions must be excluded for tomography or tomograms were not further processed.

An alternative method to produce TEM specimens can be achieved by using a focused-ion beam (FIB). Even if you can plunge-freeze cellular suspensions and directly image them, the samples still might be not thin enough to carry out EM studies. Unless the experimenter is not analysing isolated particles, but whole intact cells, the sample has a thickness in the μm range. A FIB can be used to further thin the sample. In Schaffer et al. (2017), a nice overview over the workflow of sample preparation is given. The FIB (1540XB, Zeiss) consists of two major parts, the FIB itself and a SEM to image the sample during processing. Fig. 2.14 shows simplified setup of the FIB. Along with the SEM comes an electron source. The FIB harbours a gallium ion source to mill trapezoidal windows into sample blocks or, as in our case, a thin lamella into vitrified ice. The material is removed from the milled surface by sputtering. The FIB and SEM column

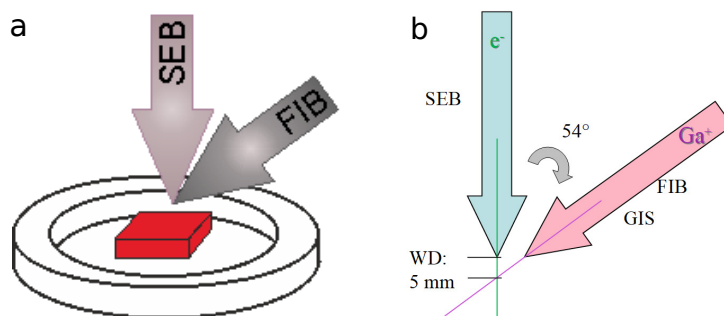


Figure 2.14.: **Schematic setup of the FIB**

a) A schematic image of a sample carrier used for thinning via FIB. b) The SEM beam (SEB) consists of electrons, whereas the FIB emits Ga^+ ions. The angle between the two beams is 54° .

e^- : Electrons; FIB: Focused-ion beam; GIS: Gallium ion source; SEB: SEM beam; SEM: Scanning electron microscope; WD: working distance

meet in an angle of 54° .

Grids with plunge-frozen ROS were inserted into a custom modified cryo-sample holder using the cryo loading stage (Leica). Subsequently, the shuttle of the EM VCT100 (Leica) was evacuated at the MED020 (Bal-Tec) and inserted at the FIB 1540XB (Zeiss) for milling and imaging.

A cellular region in the middle of the grid was chosen. This works best for the required shallow milling angles. Two milling patterns are applied: One is located above the intended lamella region; the second one below that region. A lamella of about $1\ \mu\text{m}$ thickness was obtained by the first (coarse) milling with comparable high current. Subsequently, two additional milling patterns were applied to obtain a lamella of about $200\ \text{nm}$ (fine milling; medium currents of $100\ \text{pA}$). The milling session ended with a fine polishing (at low currents) of the lamella to remove milling artifacts and to gain a smooth lamella surface.

For imaging purposes the following settings (Tab.2.8) were set.

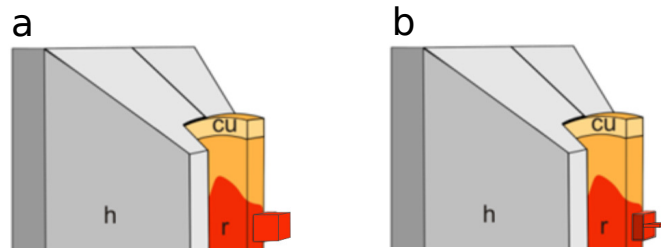


Figure 2.15.: **Produktion of TEM samples via thinning via FIB (adapted from Gunkel (2013))**

a) A sample carrier is trimmed via cryo-sectioning. It does not matter whether this HPF sample contains retina tissue or a frozen cell suspension. b) Via thinning a thin lamella is unveiled. This sample is now thin enough to be imaged via tomography. *cu*: copper carrier; *h*: holder (for cryo-sectioning); *r*: retina

Table 2.8.: Typical settings for imaging or thinning of ROS samples

Parameter	FIB	SEM
Modus	Mill + SEM	SEM
FIB probe	30 kV; 50-100 pA	30 kV; 20 pA
EHT	2-5 kV	5 kV
tilt angle	36°	20/54°
Magnification	1.5-3 kx	
WD	4.9 mm	2.8-3.2 mm

2.16. AFM on isolated ROS disk membranes

AFM measurement of ROS disks was performed by Dr Christoph Brenker.

A highly recommended review of atomic force microscopy (AFM) can be found in Muller (2008).

Isolated ROS disk membranes (section 2.8) were layered on freshly cleaved mica and incubated for 30 min. Before imaging at the AFM, the sample has been washed three

times with PBS and directly used for examining with the JPK AFM (fast scanning mode). For reference see Whited and Park (2015).

3. Results

This chapter will guide you through the experimental work performed within this study starting with the solubilization of the mouse retina and whose optimization. Then, the bleaching of the retina was quantified – a subject dealt with in section 3.1.2. Section 3.2 represents the limits of CEMOVIS, whereas section 3.3 provides alternative strategies to identify the higher-order structure of rhodopsin - faster than possible with CEMOVIS. One of these alternative strategies discussed in section 3.3.1, was to use a more traditional way to produce EM samples – the Freeze-fracture technique. Section 3.3.2 highlights the Focused-ion beam – another EM technique – to produce TEM suitable samples. However, ROS within retina samples got affected also by the properties of the sample carriers during high-pressure freezing – an issue which was focused on in section 3.3.3. Section 3.3.4 treats the results obtained via AFM. Finally, section 3.4 concludes this chapter by introducing simulation experiments, with which we wanted to evaluate, whether we reach the technical limit by EM.

3.1. Investigation of the bleaching behaviour of rhodopsin

3.1.1. Preliminary experiments

This section will describe how solubilization of the retina within this project started and will highlight some prerequisites when handling retinal samples.

After illumination, the retina was solubilised and spectroscopically analysed. Even though illumination was carried out with the intact retina, it was necessary to solubilize the retina for quantification. Only retinal solubilizates can be measured spectroscopically. Solubilization ensures homogenous samples with sufficient volume and concentration. The first experimental approach was to illuminate the isolated retina with full-spectrum light – in this point similar to the sunlight within the natural perception of light. The initial idea was to compare the illumination settings with ambient light. The assumption seemed likely, that with increasing the amount of light during bleaching, the rhodopsin peak within the absorbance spectrum gradually decreases and the MII peak increases to the same extent. It was shown in chapter 1.2.3 and especially Figure 1.2, how the individual pigments are connected within the visual cycle. In the process of handling of crude retinal extracts, numerous obstacles appeared that could not be expected beforehand. Peaks in the absorbance spectrum were showing up, which were not expected before (hemoglobin, see also section 3.1.2). Even after a long illumination of even a minute of high-energy light, it seemed that there was still a lot of remaining rhodopsin. Furthermore, our seeming rhodopsin peak was blue-shifted ($\lambda_{max} = 480 \text{ nm}$). Last but not least, the spectroscopic measurements were quite not reproducible – the reason why the data were not shown. Thorough analyses of almost all aspects of the experimental setup were necessary and led to substantial improvements, that eliminated the aforementioned problems. In the following, they will be illustrated.

First of all, gentle suction was applied to flatten the freshly isolated retina prior to illumination. This ensures to equally bleach the whole retina.

Sonification was necessary to completely solubilise the retina (see also chapter 2.6). Fig. 3.1 serves as a control for the solubilization process (including sonification). Different sonification times (ranging between 15 s and 120 s) were used to find the optimal sonification length of time. At each timepoint, aliquots were taken for the SDS-PAGEs.

Without any sonification (t_0) almost no protein, especially no rhodopsin, is detectable on either the SDS-PAGE or the Western Blot. The amount of protein solubilised within the second run of the solubilization and sonification process was clearly reduced. To ensure a fully solubilized state, the solubilization steps were carried out twice for each sample in every experiment.

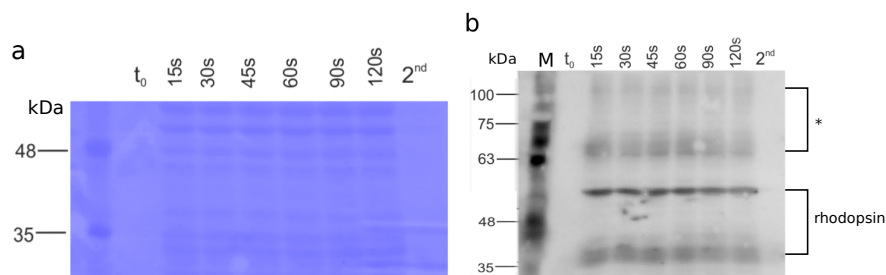


Figure 3.1.: Different sonification times of dissected retina

During optimization of the experimental protocol for the solubilization of ROS, crude retinal extracts were sonified for two minutes in total. At different timepoints (ranging between 15 and 120 s), aliquots were taken. Controls before sonification and with an additional solubilization step were taken, as well. These aliquots were loaded on a SDS-PAGE and either stained with Coomassie-Blue (a) or transferred onto a PVDF membrane and immunolabelled with $rb\alpha$ Rhodopsin (b). a) The SDS-PAGE showed bands over the entire run length of the gel - the various contained proteins typical for crude protein extracts. Only a section of the SDS-PAGE is shown, since more than 100 proteins are typical for a mouse retinal lysate (Cavusoglu et al., 2003). b) Bands appear on the Western Blot at approximately 40 kDa, 50 kDa and above 70 kDa and 100 kDa (*, glycosylated forms or oligomers) - typical for an immunostaining with polyclonal anti-rhodopsin antibody (H-300, Santa Cruz).

N=3; M: Marker (10-245 kDa)

Second, by disruption of the equilibrium (between MI and MII) using hydroxylamine, as described in section 1.2.3, no substantial amount of MI remains, and no MIII is formed and can hinder the spectroscopic measurement. The third change affected the lamp used for illumination itself. To cover the absorbance range of rhodopsin it is sufficient to use a green lamp. This ensures to avoid the potential photolysis of MII by blue light (Bartl, Ritter, and Hofmann, 2001; Ernst and Bartl, 2002). By initially using a white lamp, which did emit light below 420 nm, a photolysis of MII, which was proposed by Bartl *et al.* and

Ernst and Bartl, is in retrospect likely.

Without hydroxylamine and with light with a wavelength below 420 nm, the spectroscopically measured peak at 500 nm (normally the rhodopsin peak) would not adequately decrease upon bleaching. A signal would still be detected in this wavelength region – a blue-shifted peak (originating from MIII; 480 nm) would falsely indicate an amount of unbleached rhodopsin. See also Fig. 1.2. This is the reason, why long illumination times did not lead to a proper decrease of absorbance values of these initial experiments and why this peak was blue-shifted. Subsequent experiments were carried out with the use of hydroxylamine and a green light LED, which does not emit light below 420 nm.

3.1.2. Quantification of the bleaching of Rh within the intact retina

The following section provides details about the quantification of the rhodopsin bleaching. The aim was to bleach the rhodopsin still embedded within the intact retina. For quantification of the bleaching, it was necessary to solubilize the retina subsequently. *N*-Dodecyl- β -*D*-maltoside (DDM) was used to solubilize the retinas, because rhodopsin liberation is more effective with this detergent than with others. Preliminary experiments with digitonin and Triton X-100 showed that the experimental set-up (including solubilization, illumination, and spectroscopic quantification) is indeed promising. However, data are not shown, because they were less suitable than obtained with DDM.

The main reason to change the lamp for illumination was that – as mentioned above – white light is not feasible for bleaching experiments *in vitro* because of the photolysis of MII and the formation of MIII (see also sections 3.1.1 and 1.2.3). Therefore, green light was used for the bleaching of rhodopsin instead of natural or white light to diminish the photolytic conversion of MII. Another reason to change the lamp was that the natural light or ambient light was considered too weak to fully bleach the retina in a comparable short time. This is because the bleaching experiments were run with a high power LED.

Retinas were prepared and solubilized according to chapters 2.5 and 2.6. Illumination lengths ranging from 20 ms to 26 s were chosen on the basis of the preliminary experiments. The results are displayed in Fig. 3.2 and 3.3.

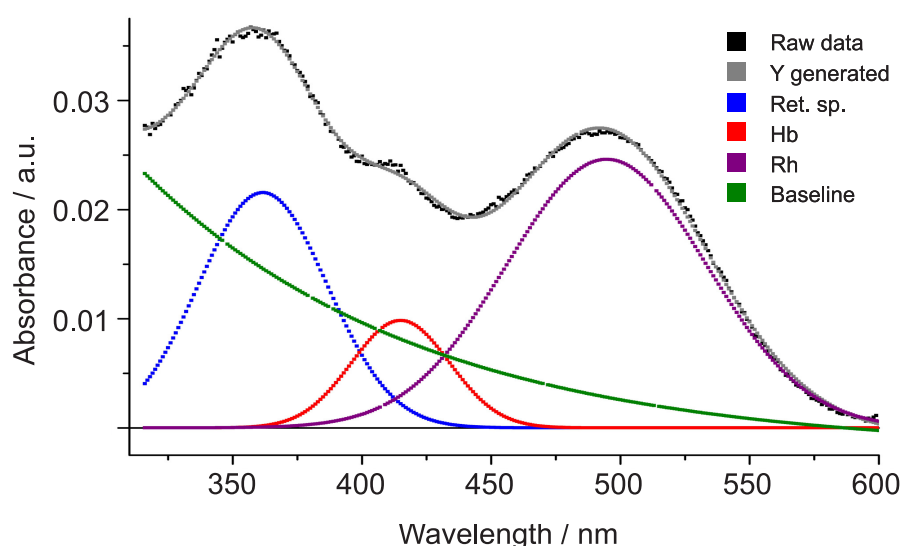


Figure 3.2.: Deconvolution and peak identification

Exemplified processing of the measured raw absorbance spectra of the retinal extracts. Raw (black dotted line), deconvoluted, and fitted (grey) spectra of crude retina extracts. Here, the mean of the dark-adapted retina samples is shown. Peak fitting was done with PeakFit. For experimental details see section 2.6 and especially subsection 2.6.5. The exponentially fitted baseline is shown in green. Additional peaks beside the rhodopsin absorbance peak are visible. The first Peak (blue) has its origin in various retinaldehydes and esters (Grip, Daemen, and Bonting, 1980) contained within the crude extract. The second peak (red) was identified as hemoglobin ($\lambda_{max}=415$ nm, Knowles, McDonald, and Gibson (1975) and Poincelot et al. (1970)). The third Peak (purple) comes from rhodopsin ($\lambda_{max}=500$ nm, Wald and Brown (1953)).

Hb: hemoglobin; *Ret. sp.*: retinal species; *Rh*: rhodopsin

The software PeakFIT was used to identify and deconvolute the absorbance spectra of the solubilised retinal extracts. This was necessary because the baseline was heavily inclined. See also Fig. 2.6. The three peaks, PeakFIT could identify, had the dominant wavelengths of 362 nm, 415 nm, and 500 nm (see Fig. 3.2). Only minor variances from

one data set to another have been measured.

The first peak with λ_{max} around 365 nm could be identified as coming from various retinaldehydes, esters, and oximes (Grip, Daemen, and Bonting, 1980). The second peak with its absorption at 415 nm has its source in hemoglobin (Knowles, McDonald, and Gibson, 1975; Poincelot et al., 1970), originating from several blood vessels within the retina. During solubilization hemoglobin got extracted, as well as all other retinal proteins. A subsequent purification could have removed this contaminant, but was not done in order to keep the processing time of the retinal extracts as short as possible. Keeping the preparation time short has the advantage that the risk of an artificial degradation of rhodopsin is diminished. Amounts of hemoglobin within the extracts were accepted. The third peak is the pure rhodopsin signal (Wald and Brown, 1953).

Taking a detailed look on Fig. 3.3a, comparing the peak maximum of the remaining rhodopsin between the different illuminated samples, it is also notable that the peak maximum of Rh shifts slightly about a few nm. Rhodopsin bleaching starts fast and slowed down quickly. The graph alone would indicate a full bleaching of rhodopsin with an illumination of about 18 s. However, data needed to be processed further to make a statement about bleaching dynamics. Statistical analyses of the peak maxima displayed in Fig. 3.3a lead to realization that bleaching must occur exponentially (Fig. 3.3b). Function and R^2 are listed in Fig. 3.3b, as well. The half-life of rhodopsin's absorbance was calculated as 33,56 ms. The base line of this function can be regarded as full-bleaching. The values were read in Fig. 3.3b. As an example, with a flash illumination of 20 ms, a rhodopsin fraction of 31% is bleached. The results may be summarized as follows (Tab. 3.1).

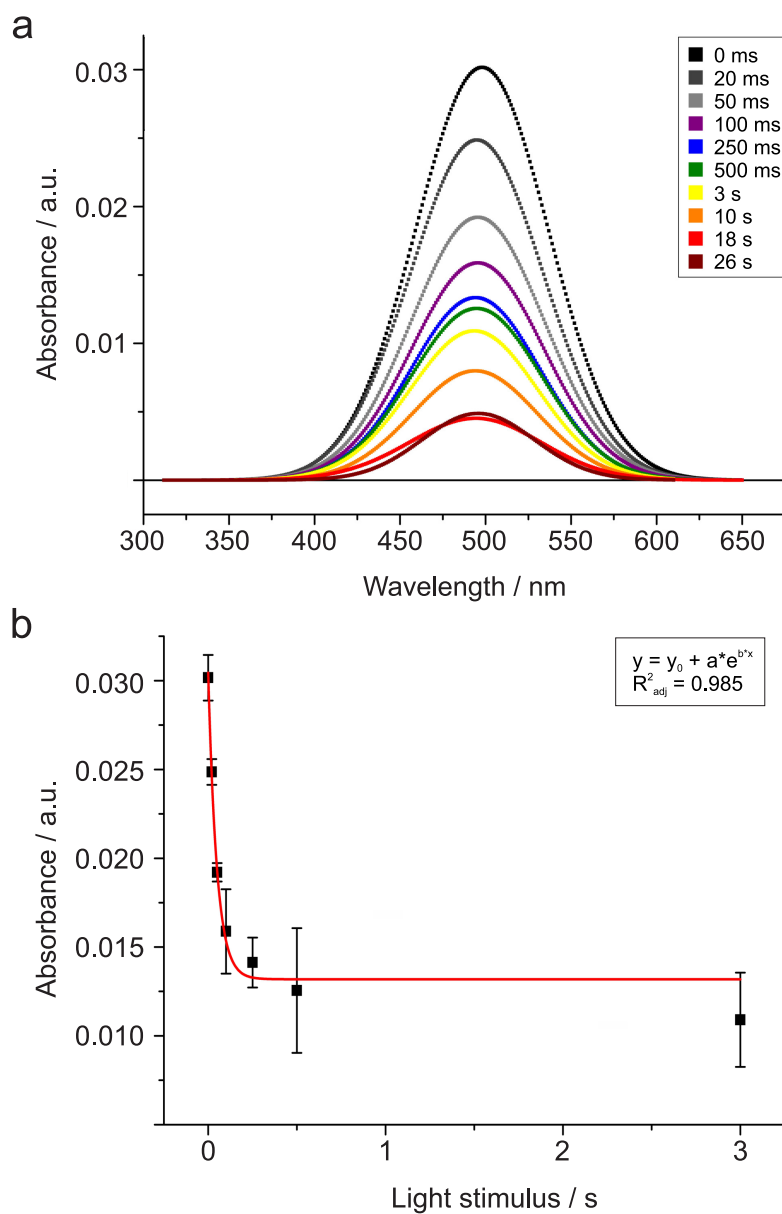


Figure 3.3.: **Quantification of the rhodopsin bleaching**

(a) Rhodopsin absorbance upon various illumination conditions. Rhodopsin absorption decreases with elongation of illumination durations. (b) Bleaching curve of rhodopsin. Rhodopsin bleaching occurs exponentially within the short time scale. Longer illumination times were excluded as long-time processes were of minor interest.

Table 3.1.: Which illumination time corresponds to which bleaching state of rhodopsin?

Illumination time	State	Bleaching
0 ms	dark-adapted	$0 \pm 4.1\%$
20 ms	mixed	$31.2 \pm 2.8\%$
50 ms	mixed	$64.4 \pm 2.5\%$
100 ms	mixed	$84.3 \pm 15.2\%$
250 ms	mixed	$94.1 \pm 9.5\%$
500 ms	fully-bleached	$103.6 \pm 27.8\%$
3 s	fully-bleached	$112.2 \pm 24.5\%$
10 s	fully-bleached	100%

3.2. Cryo-electron microscopy of vitreous sections (CEMOVIS)

Gunkel et al. could show the tracks of rhodopsin within dark-adapted mouse retina samples using CEMOVIS (Gunkel et al., 2015). However, CEMOVIS is on the one hand an advantageous technique but can have some drawbacks on the other hand, which are focused on in detail in the following section.

3.2.1. Cryo ultramicrotomy

To analyse the supramolecular structure of rhodopsin, cross and longitudinal sections of ROS were prepared.

During high-pressure freezing, retinal samples got vitrified. Samples which passed the quality check (homogenous appearance, no milky areas, and no holes in tissue or cryoprotectant) are further processed via cryo ultramicrotomy. A fraction of samples got discarded during ultramicrotomy due to fractures or the lack of adequate sectioning. Sectioning artifacts, which reduce the output further, include crevasses (caused

by friction on the knife surface), chatter (slice thickness variations), or knife marks (see also Al-Amoudi, Studer, and Dubochet (2005)). Longitudinal sectioning is rather simple compared to cross sectioning. Cross sections suffer from artifacts in a larger extent than longitudinal sections.

In perfectly oriented cross sections, the disk surface is accessible for imaging. Supramolecular structures of rhodopsin must be visible within the disk membranes directly. However, to get nice cross sectioned samples of the retina which survive all experimental obstacles mentioned above is even less likely. This is because the sectioning procedure for cross sections is more harsh than for longitudinal sections. The sample mounted in the ultramicrotome has less support due to the orientation than for longitudinal sectioning. As a consequence, the samples are less stabilized and more fragile. To cut a ROS perfectly cross oriented is rather unlikely. The average disk thickness is about 19 nm (Gunkel, 2013). The space in between two disks is 16 nm (Gunkel, 2013). As a consequence, there only fit a maximum of two disks in a typical cryo section of a thickness of 40 to 50 nm. Unfortunately there is no possibility to check the orientation of sectioning in between. The orientation is only observable during tomography.

3.2.2. Single-axis cryo electron tomography

First will be discussed, that cross sections should enable a view on the disk surface. Second, longitudinal sections can also be used to clarify rhodopsin's supramolecular state. The reason is, that the volume can digitally be flipped. However, this is again limited by the sample thickness of about 40-50 nm.

Cryo electron tomography of cross sections

Perfectly oriented, artefact-free, and cross sections are almost impossible to obtain. During preparation the ROS may be distorted or bended by compression (most likely during

HPF). ROS are then not sectioned in cross orientation, but oblique. Cross sections are more prone to artifacts than longitudinal sections. However, if the area of interest shows crevasses, chatter, or even knife marks, these artifacts can mask features of the disk membrane. Furthermore, the contrast of cross sections within the TEM is lower than for longitudinal sections. This is why identifying regions of interest becomes more difficult.

Table 3.2.: Overview of tomograms of cross sectioned samples

Sample	Recorded tomograms	Quality
1	19	discarded, not cross oriented
2	34	discarded, not cross oriented section movements during acquisition
3	2	discarded, RIS
4	11	discarded, not cross oriented burnings, movements during acquisition
5	7	discarded, not cross oriented
6	2	discarded, not cross oriented
7	30	discarded, not cross oriented
8	7	discarded, not cross oriented
Σ	112	

From 112 raw tomograms, 15 looked promising at the beginning and were processed further. At alignment during tomogram reconstruction it was most often noticed that the sections were not cross but rather oblique or even longitudinal. At this point also slight movements of the retinal section were observed. These movements hinder a successful alignment.

Cryo electron tomography of longitudinal sections

Even in longitudinal sections, it is possible to access the disk surface. Therefore, the views (projections at a single stage tilt) are summed up to enhance the contrast using the IMOD tool *slicer*. The XYZ tool is adjusted to reach a computational cross section. As a

prerequisite the longitudinal sections need to be of superior quality. Even though 120 tomograms were recorded, they all were discarded during the extensive data-processing. The reasons for that were that sometimes the section started to move during tomogram acquisition. This movement is not always obvious before or during acquisition. It may be slight and appears only during alignment. Some tomograms showed ROS distortions (disks were heavily bended, zigzag-shaped, showed reduced or wide interdisk distances). Some tomograms failed to be properly aligned during reconstruction. This can be caused by a lack of fiducials or fiducial clustering in the raw tomogram.

Fig. 3.4 shows exemplarily two images from tomograms from longitudinally sectioned retina samples.

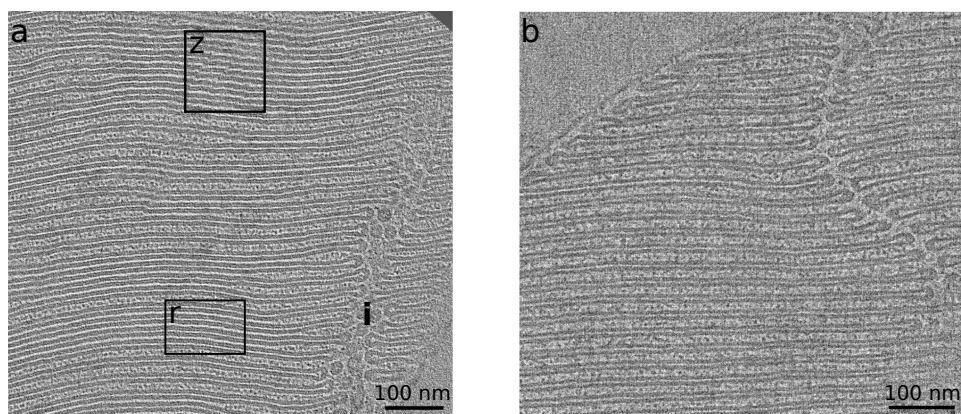


Figure 3.4.: Example images of tomograms of longitudinal retinal sections
a) and b) Tomograms of 50 nm-sections of longitudinally sectioned retina samples. Image quality was not good enough to proceed with data processing.
i: incisure; r: reduced interdisk distance ; z: zigzagged disks

Unfortunately, image quality was not good enough. Boxes in Fig. 3.4 a indicate regions, where disks are zigzag-shaped or show greatly reduced interdisk distance. Here, the interdisk distance was reduced from 16 nm (Gunkel, 2013) to 4 nm. Outside of the box the interdisk distance was reduced to 10 nm. CEMOVIS therefore seems to be a time-consuming and less effective technique. Furthermore, the most interesting issue, to

analyze putative changes in the supramolecular structure upon different illumination conditions, remains unachievable with this technique. It was coming clear that the experimental approach, I was following, is not suitable to investigate the higher-order structure of rhodopsin in a row within different illumination settings. We had to think about some alternative experimental approaches which are depicted in the following sections.

3.2.3. Dual-axis electron tomography

As already discussed, one can also make use of longitudinal sections to get information of the disk membrane. For this purpose, projections are summed up and rotated digitally (etomo slicer, XYZ-view) to gain a computational cross section. However, a 40 nm thin section is not sufficient for this purpose. Paired rhodopsin molecules may be visible, but if the rhodopsin tracks found by Gunkel et al. (2015) are altered in form, frequency, or length will stay exclusive to the experimenters eye. Analyzing thick sections (100-150 nm) would circumvent this problem.

To improve the useable volume in the tomogram cryo sections with a thickness of 100-150 nm were prepared and analyzed. For tomography of thick sections energy-filtered images are necessary, because of the increased ice thickness. In our lab, this can be achieved with the Gatan imaging filter (GIF) which is mounted in the Titan Krios. Because, the GIF unit is filtering inelastically scattered electrons, also image intensity of the recorded tomogram is reduced. Due to the missing wedge, the information loss in thick sections is normally too high to achieve a resolution of 4-6 nm, which is needed for the proper identification of a higher-order structure of rhodopsin. Therefore dual-axis tomography experiments were made to improve the data quality. The amount of information lost during acquisition is reduced compared to use only one axis for tilting of the stage. The Titan Krios at caesar was equipped with a 90° in-plane rotation stage

for dual-axis experiments. See section 2.11.2 for more details!

One cannot tilt the sample for 360° to get a full view of the sample – the enormous ice thickness at full tilt of 180° would make imaging impossible. Tilting from -60° to $+60^\circ$, 67% of information is collected with normal (i.e. single-axis) tomography. That's why one always loses information of the sample during tomography. The shape of the information lost during acquisition of a single-axis tomogram is a wedge – therefore, it is called the *missing wedge*. With dual-axis tomography 84% information would be kept (Lučić, Förster, and Baumeister, 2005). The information lost of dual-axis tomograms is shaped like a cone and thereby called a *missing cone*.

Preliminary experiments

Unfortunately, the 90° in-plane rotation stage of the Titan Krios had no built-in algorithm for lateral compensation after 90° rotation. Why is it necessary to accurately find again the ROI after rotation? For acquisition of a typical electron tomogram one needs to apply a dose of 69 to $100 e^-/\text{Å}^2$. For acquisition of a dual-axis tomogram this dose needs to be split up for both axes. Every image, which is necessary to be acquired to find back the ROI, may lead to an overexposed tomogram (burnings) or the dose for tomogram acquisition needs to be reduced. Therefore it is necessary to find back the accurate position without excessive imaging.

Due to a lack of an algorithm for axis rotation, a tilt series was recorded to calculate a correction matrix with which it will be possible to compensate for the lateral shift on the sample. This was realized with Microsoft Excel. Sample position (XY) at 0° was entered and the rotated position X'Y' after 90° rotation was calculated. With this set-up it was possible to determine the rotated ROI with an accuracy of 1-2 μm .

Dual-axis cryo electron tomography of thick sections

After setting up the correction matrix it was possible to record dual-axis tomograms. For dual-axis tomography, thin (40 nm) and thick (100-150 nm) sectioned samples were used. Fig. 3.5 shows images of two dual-axis tomograms.

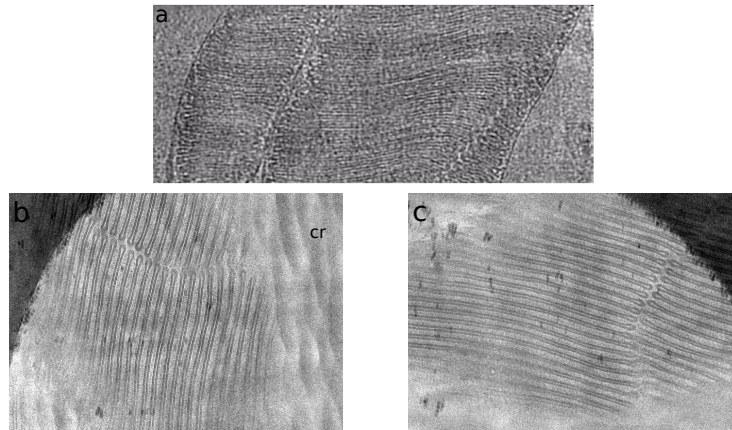


Figure 3.5.: Example images of a dual-axis tomograms

a) Tomogram image of a 50 nm-section of longitudinally sectioned retina sample. Tomogram could be reconstructed, but shows poor data quality. b) and c) Tomogram images of 100 nm-thick section of longitudinally sectioned retina sample corresponding to the two axes with which tomograms were recorded. Sectioning artifacts (crevasses) were indicated. Tomograms of both axes could not successfully reconstructed and combined.

cr: crevasses

Thin sections (thickness: 40-50 nm) were burned during acquisition easily. Thick sections suffer from low contrast and a high amount of sectioning artifacts. Even though 41 dual-axis tomograms were recorded, none of these was sufficient to identify the higher-order structure of rhodopsin.

In fact, the contrast of a dual-axis tomogram in general is lower, because you have to divide the electron dose applied onto the region of interest (ROI) by 2. This makes post-processing more difficult and time consuming. Alignment during reconstruction is more difficult and prone to fail. More often tomograms had to be discarded, even before

data processing, because data were not sufficient compared to single-axis tomography. The alignment of the single projections had to be refined extensively. Compared with single-axis tomography, the gain of information by dual-axis tomography could not outweigh the efforts for preparation and analysis. This is why, I stopped doing dual-axis tomography.

3.2.4. Cryo electron tomography of isolated ROS

We followed the CEMOVIS protocol for isolated ROS suspensions in order to reduce dimensionality of the frozen sample. ROS were prepared as described in section 2.7, and subsequently high-pressure frozen, sectioned, and imaged in the TEM. An example image can be found in Fig. 3.6.

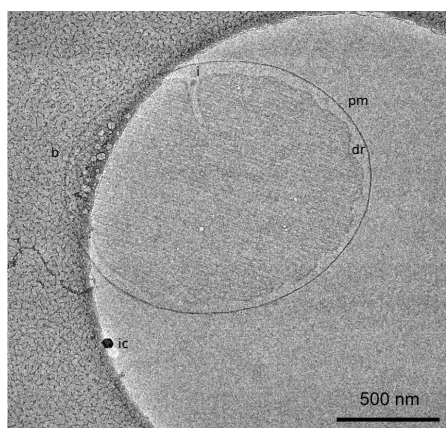


Figure 3.6.: Example image of a putative cross section of HPF ROS

Tomogram of 50 nm-section of a high-pressure frozen ROS sample. Features of the ROS are highlighted. However, even though ROS section looks sectioned in cross direction, image quality does not allow further processing as image was overexposed and shows burnings.

b: burnings; *dr*: disk rim; *l*: incisure; *ic*: ice crystal; *pm*: plasma membrane

Searching ROIs during tomography turned out to be very time consuming. Depending on the sample it takes several days. 11 tomograms were recorded, of which the example above was the most promising result. However, even this ROS was not a real cross

section and the higher-order structure of rhodopsin could not be resolved. ROS concentrations need to be re-evaluated and increased to make this procedure a valid alternative technique for imaging the supramolecular architecture of rhodopsin.

3.3. Alternative approaches for investigation of rhodopsin's higher-order structure

From hundreds of recorded tomograms, only some were suitable to be processed further. We, therefore, thought about some alternatives to speed up the identification of the rhodopsin superstructure. These alternatives are pictured in the following section. To circumvent CEMOVIS artifacts, we planned to do freeze-fracture of frozen retinas, alternatively (see section 3.3.1). We planned to prepare tomography on lamellas prepared with the FIB (section 3.3.2). In section 3.3.3 the surface of sample carriers is referred to as one source of implications. Additionally, the AFM was used to analyze isolated ROS disks (section 3.3.4).

3.3.1. Freeze fracture

Frozen samples are inherently temperature sensitive and fragile. The freeze-fracture technique takes advantage of this fragility. This is the subject dealt with in the following section.

For freeze fracture experiments, the retina sample is frozen with high-pressure freezing and hit by a knife (see also Fig. 2.13). The sample breaks along its most fragile site. A fracture along disk membranes within the ROS seems to be achievable, if one can manage to hit the retina sample in the region of ROS. Fig. 3.7 shows exemplarily the result of a freeze-fracture experiment with high-pressure frozen retina.

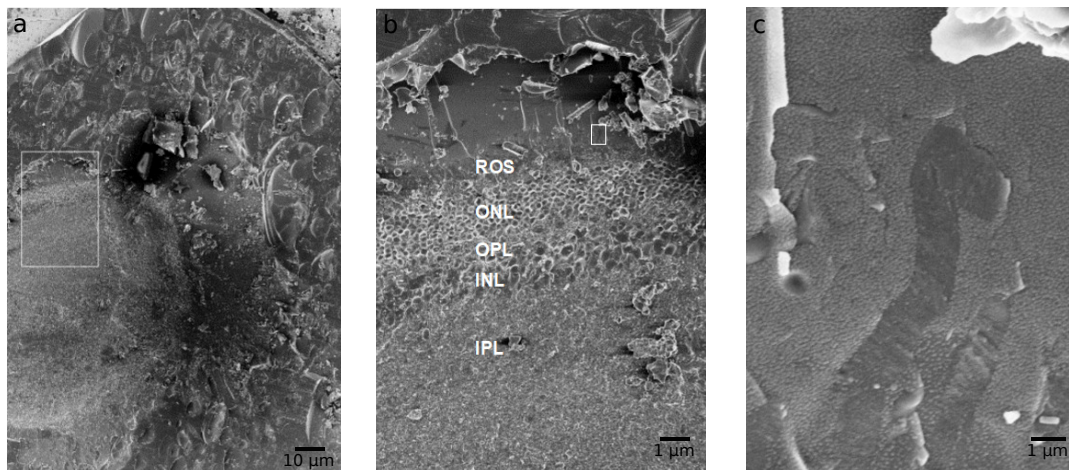


Figure 3.7.: Freeze-fractured retina

Freeze-fractured retina HPF sample at 44 x magnification (a), 447 x magnification (b), and 1000 x magnification (c). The assigned inner cellular layers of the retina are labelled.

INL: inner nuclear layer; *IPL*: inner plexiform layer; *ONL*: outer nuclear layer; *OPL*: outer plexiform layer; *ROS*: rod outer segments.

All inner layers of the retina were found, implicating that the retina was frozen unintentional in a bended state. If the sample got processed further (either via sectioning or thinning with the FIB), for tomography only tilting angles of about 30° would have resulted. Which would not be sufficient. This is the reason why samples with such bended ROS were not processed further.

3.3.2. Production of TEM specimens using FIB

FIB lamellas can alternatively serve as TEM specimens. Their perfect orientation and complete absence of sectioning artifacts make them advantageous.

One way to obtain a sample suited for the FIB, is to plunge-freeze isolated ROS (see also section 2.9.2). This way was followed by Schaffer et al. (2017) und Noble et al. (2018).

Another source of specimen for thinning via FIB is the HPF. In specially designed or custom-built FIB holders, HPF carriers can be mounted. A custom-built holder was

manufactured by the in-house workshop. However, as sample carriers lead to artifacts during freezing - a topic which will be dealt with in the next section (section 3.3.3) - this path of production was not pursued further.

In detail, we will focus on the use of plunge frozen specimens for the thinning. ROS have a length of about 24 μm and a diameter of about 1.3 μm (Nickell et al., 2007). Due to the forces applied during the plunge-freezing process, the ROS will be aligned lengthwise on the grid. Ice thickness varies between several hundred nm and 1 μm . With this sample thickness, one can hardly acquire tomograms. The FIB can be used to thin the whole sample or to mill an acquisition window at a specific area in the sample block, just big enough for doing tomography - as shown in Fig. 3.8.

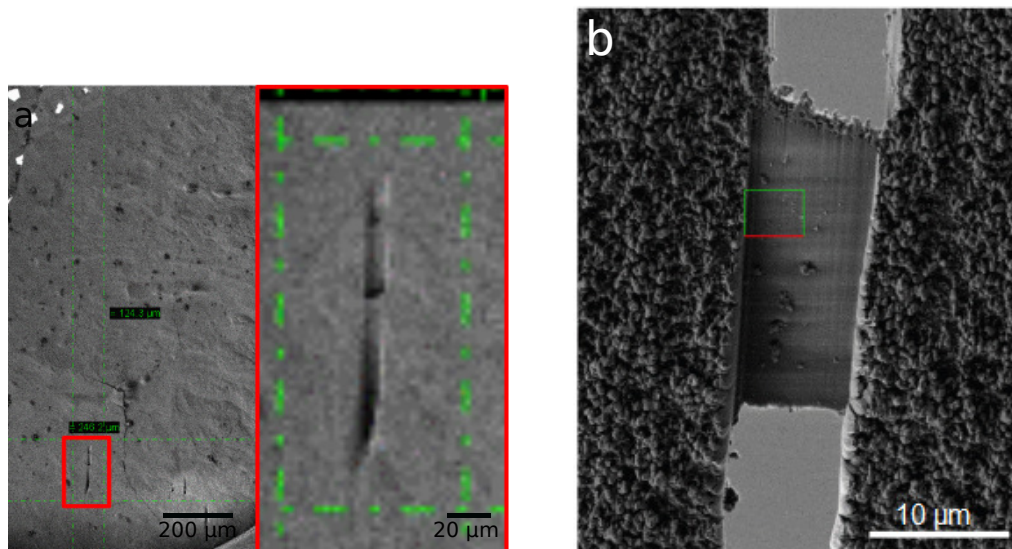


Figure 3.8.: **Production of FIB lamella**

a) Lamella preparation via FIB of plunge-frozen ROS. In low magnification (70x) the milled lamella is visible. Insert shows a zoom-in into this area. b) Lamella ready for transfer into Krios for imaging.

In thick ice samples, ROS are not easy to find. The search of suitable areas is very time-consuming as is blind milling of big areas. Both strategies take 24 hours (excluding imaging time at the TEM) and are thereby not feasible. The ice thickness first had to be

optimized, before milling via the FIB is advantageous for our purpose.

3.3.3. Influence of HPF carrier surface morphology on sample quality

The prior experiments were depicted in the previous chapters regarding their usefulness for the aim of this study - the analysis of the higher-order structure of rhodopsin. However, what is crucial for the parallel and thereby proper alignment of the ROS? The answer is: the sample carrier where the retina is frozen in. These sample carriers – or their surface properties to be precise – we will investigate during this section. HPF carriers were used during this study to freeze retinal tissue, as well as ROS suspensions. These HPF carriers then got used for CEMOVIS or thinning via FIB.

According to Sandberg et al. (2005) the retina has a thickness of 218 μm . Giving the prerequisite of ripping away the RPE during dissection of the retina, the ROS region is the outermost retinal layer. Frozen within the normal sample carriers with an indentation of 150 μm they are slightly bended via high-pressure freezing. The ROS should ideally be aligned parallel to each other and transverse to the carrier surface. However if they are bended (even if slightly), the alignment might be distorted. Sample carriers with an indentation of 200 μm cannot be used, because vitrification is less effective and the reject rate (non-useable samples) is higher (Sartori, Richter, and Dubochet, 1993), again. The empty sample carriers were examined with the AFM and showed small but distinct and regular surface patterns on the basis of the carrier indentation and also on the “flat” cover carriers (Fig. 3.9). This pattern is production-related. Concerning the high pressure during high-pressure freezing, the production-related distortion seems to be amplified. A sample with a negative imprint of this carrier pattern is depicted in Fig. 3.10. Fig. 3.10 also shows distorted ROS as a putative result of imperfectly frozen samples.

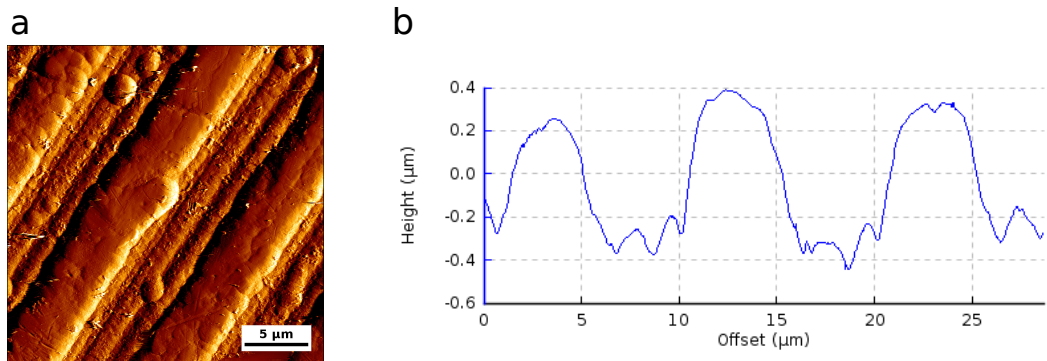


Figure 3.9.: Surface indentations on carrier surface measured with AFM
 Blank carrier surfaces were analysed via AFM. A) shows the deflection image of the carrier surface. B) shows the corresponding height profile. AFM probe deflections reveal indentation depths of about $0.8 \mu\text{m}$. Giving that the length of one rod is about $1 \mu\text{m}$, one can easily understand why a perfect orthogonal orientation of the rods facing this carrier surface is hard to obtain. The effect of this uneven surface is maybe not limited to the outer layer, but transferred to the inner layer of the sample, which has to be frozen by high-pressure freezing. This effect even may be intensified by the high pressures during freezing.

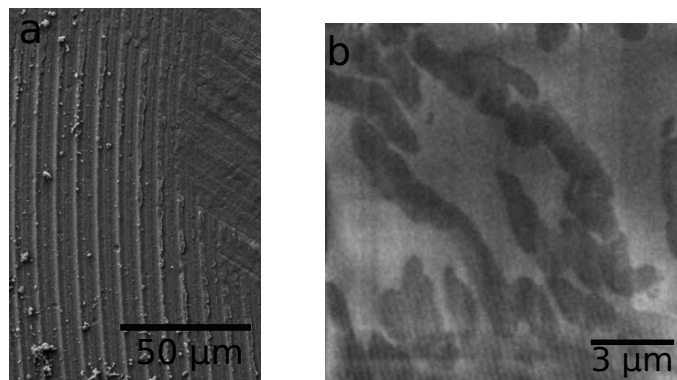


Figure 3.10.: Negative imprint of carrier surface indentations on on high-pressure frozen specimen and distorted ROS

a) Sample frozen by high-pressure freezing. Top carrier removed with intention to perform FIB milling and thereby production of TEM samples. A negative imprint of the surface indentation of the top sample carrier is still visible on the surface of the sample. Ice chunks are transfer ice resulting from transport of the sample from the ultramicrotome to the FIB. b) ROS are distorted and not suitable for subsequent FIB milling.

As a result, we subsequently have tried to polish at least the covering carriers to

diminish the distortion. The cells of these samples – frozen with these polished carriers and further processed for TEM specimens – were not distorted and aligned parallel to each other (see Fig. 3.11). Nevertheless, they were also merely not intact any more

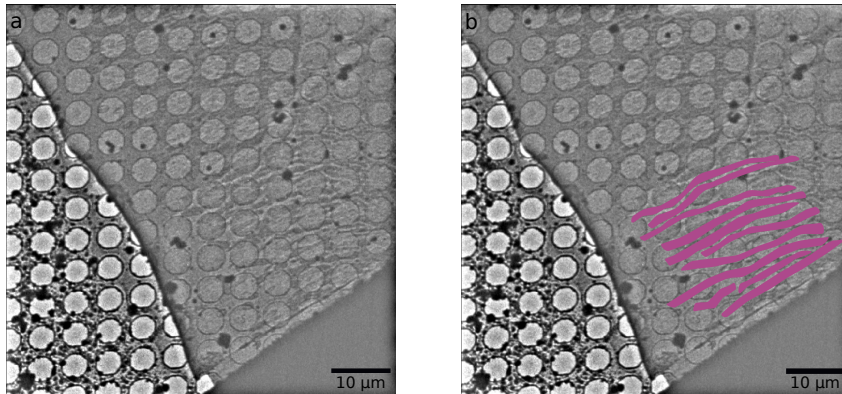


Figure 3.11.: **ROS aligned parallel after polishing of sample carriers**
a) Low-magnification image of a ribbon of cryo-sections. ROS found parallel aligned to each other by using polished carriers for HPF. b) ROS were highlighted with pink to facilitate identification.

and showed a lot of artifacts. None of the recorded tomograms could be processed further. We think, this is because of cytotoxic effects of the copper layer revealed during polishing. A subsequent gold application onto the polished carriers (via sputtering) turned out to be non-sufficient to compensate for these cytotoxic effects.

3.3.4. Atomic-force microscopy

ROS disks were prepared as described in chapter 2.8 and used for imaging with AFM (chapter 2.16). In this preliminary AFM experiment three samples of the same ROS disk preparation were examined. Fig. 3.12 shows one example. An ordered structure is visible - putatively of rhodopsin tracks.

These tracks show some similarities with the results obtained by Fotiadis et al. (2003), Liang et al. (2003), and Filipek et al. (2004). Unfortunately, it was not possible to repeat this experiment. This alternative approach is the most promising experiment to identify the higher-order structure of rhodopsin. Nevertheless, at least one repetition would be

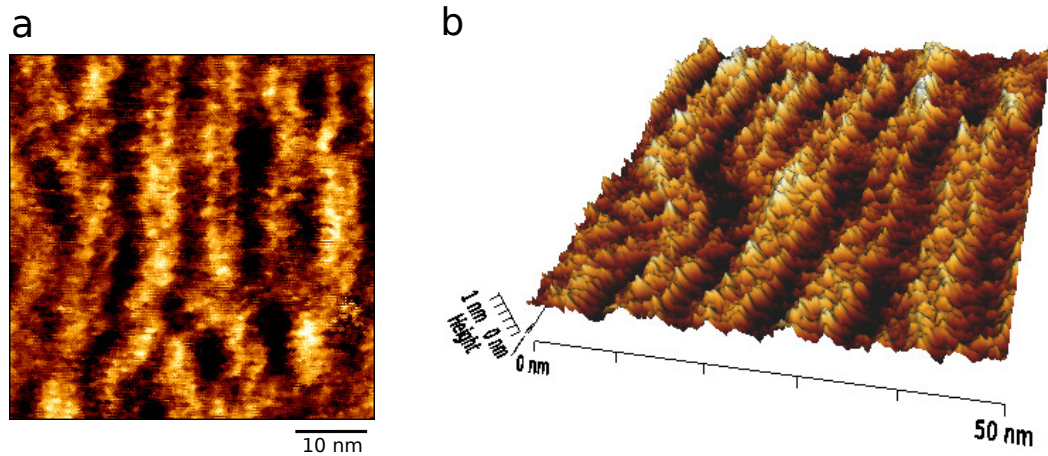


Figure 3.12.: **ROS disks examined with AFM**

A) Deflection image of ROS disks. B) Height trace of ROS disks showing a regular pattern.

necessary. If this result will be confirmed, even preparations with different illumination conditions can be performed.

3.4. Simulation of a cryo electron tomogram

The technical obstacles and artifacts lead us to think about the perfect data set - a simulated tomogram. For technicals details see section 2.13. Fig. 3.13 shows how a simulated tomogram can be integrated into a recorded tomogram. This serves as a control of dimensions and grey values.

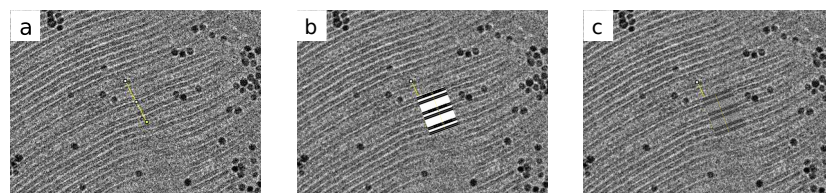


Figure 3.13.: **The simulated tomogram can easily be inserted into a real tomogram**

a) Original tomogram of longitudinally sectioned ROS. b) Simulated tomogram without noise integrated. c) Simulated tomogram with noise integrated.

If a tomogram of a longitudinally sectioned ROS is flipped digitally, the 40 to 50 nm wide disk surface is accessible via imaging. The same can be done for simulated tomograms, as well. Fig. 3.14a and b show digitally flipped tomograms.

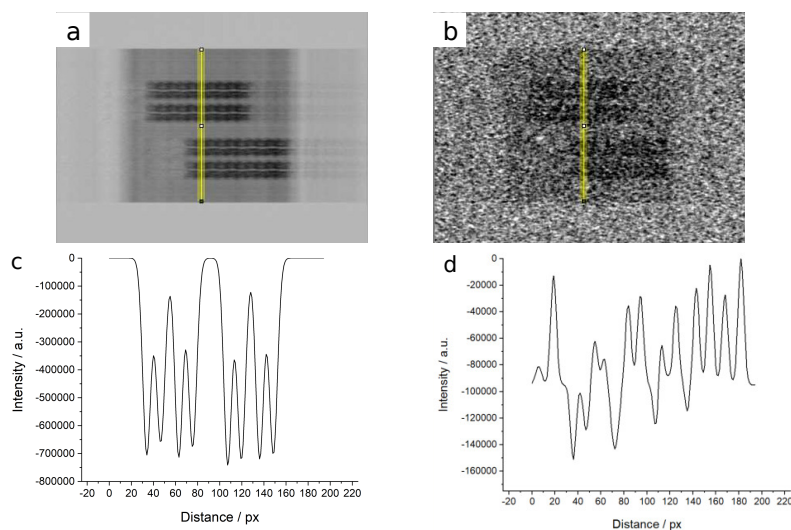


Figure 3.14.: Plot profiles of simulated tomogram without and with noise
a) Reconstruction of a simulated tomogram without noise. b) Reconstruction of a simulated tomogram with noise. c) Fitted plot profile of simulated tomogram without noise (yellow line in (a)). Eight distinct peaks indicate the identification of rhodopsin molecules. Two peaks belong to one track. Here two tracks are visible. d) Fitted plot profile of simulated tomogram with noise (yellow line in (b)). In contrast to the reconstruction without noise, the plot does not show clear rhodopsin peaks at the same distances as in (c).

Here, disk surface is partially visible. One can clearly see the two modelled rhodopsin tracks. The simulated tomogram without noise serves as a positive control. Here, the contrast is perfect. Rhodopsin molecules are easily distinguishable. A plot profile (Fig. 3.14c) shows eight peaks showing the presence of rhodopsin. The plot profile for the noised tomogram (Fig. 3.14d) cannot reveal all rhodopsin peaks.

4. Discussion

The final chapter of this study will summarize findings and will highlight experimental ideas which could be followed in future. After a discussion of the illumination of rhodopsin (section 4.1), the drawbacks of CEMOVIS will be detailed in section 4.2. Sections 4.3 to 4.4 discuss obstacles FIB, freeze-fracture and HPF sample carriers. Additionally, ROS suspensions are discussed as a possible solution. Results obtained via AFM are dealt with in section 4.6. Artifacts are the main topic of section 4.7, here also the perfect data set – obtained by simulations – is discussed. Section 4.8 sheds light on possible consequences of illumination on the higher-order structure of rhodopsin. Alternative techniques will be discussed in section 4.9.

4.1. Rhodopsin's bleaching behaviour - a prerequisite to analyze illuminated retinas

A protocol could be established to successfully illuminate the intact retina, followed by a subsequent solubilization to quantify the bleaching effect. Solubilization involves the use of detergents and sonification. As seen in Fig. 3.1, solubilization with the established protocol can be considered as complete. It was further possible to measure the absorbances of a range of differently illuminated retinas. Fig. 3.2 shows how an absorbance spectrum of a dark-adapted sample looks like after deconvolution of the raw absorbances. The contained peaks of the different pigments could be identified as

a mixture of retinaldehydes, esters, and oximes (peak at 362 nm), hemoglobin (peak at 415 nm), and rhodopsin (peak at 500 nm). In Fig. 3.3a the rhodopsin peaks of the different analyzed illumination conditions are summarized. Fig. 3.3b presents how fast rhodopsin bleaches. It was possible to determine a function for rhodopsin bleaching ($y = y_0 + a * e^{b*x}$). According to that, full-bleaching can be reached with an illumination of 500 ms. Rhodopsin bleaches exponentially, which is in line with Berry et al. (2016). Nevertheless, Berry et al. (2016) goes into more detail. As phosphorylation of rhodopsin by rhodopsin kinases (GRK1) and arrestin binding is responsible for the shut-off of the activated rhodopsin (receptor desensitization), subsequent dephosphorylation is necessary for recovery of rhodopsin. The effect of the inhibition of rhodopsin's dephosphorylation on dark adaptation in mouse rods and subsequently altered kinetics are shown in Berry et al. (2016).

Initial experiments were carried out with digitonin and Triton X-100, but both turned out to be suboptimal. Solubilization of rhodopsin is in fact possible with digitonin, but less effective (Fong et al., 1982). Triton X-100, on the other hand, is more effective. However, this detergent is rather harsh – aggregates can form (Fong et al., 1982). DDM was chosen, because it is more feasible: DDM is not stabilizing rhodopsin in solution, but is less destabilizing the MII state (Seddon, Curnow, and Booth, 2004). Furthermore, if DDM concentration is not chosen too low (below 0.05%), MIII formation is less (Ramon et al., 2003). A publication of Eps et al. (2017) compared rhodopsin purified in DDM and in nanodisks. Interestingly they found that rhodopsin within nanodisks is present in various substates, whereas rhodopsin solubilized with DDM prefers one single – the inactive – conformation (Eps et al., 2017). This strengthens the assumption, that none of the detergents used (digitonin, Triton X-100, and DDM) is the best choice detergent for the solubilization of rhodopsin and its investigations. Within this study, DDM was used as a component of the solubilization buffer. For the quantification of rhodopsin's

bleaching, the conformational substrates should not affect the bleaching result, as illumination preceded the solubilization. However because of the findings of Eps et al. (2017), one should consider another detergent, if imaging experiments with solubilized retinal extracts, ROS suspensions, or disk suspensions will be proceeded.

Interestingly, there is a remaining peak at 500 nm even if the sample is totally bleached (Fig. 3.3a). How can this be? Several photopigments within the visual cycle after MII formation may also interfere, here. Bartl, Ernst, and co-workers could find a photolytic pathway, in which blue ($\lambda < 420 \text{ nm}$) or green light induces a conversion from MII to P500 and back to MII, respectively (Bartl, Ritter, and Hofmann, 2001; Ernst and Bartl, 2002). The converted photoproduct P500 absorbs light at a wavelength of 500 nm. It would can falsely indicated that there is still a fraction of rhodopsin which has not been bleached already. This could be an explanation why there is still an amount of measured pigments at 500 nm in Fig. 3.3a for 18 and 26 s. The quantification of the bleaching of rhodopsin still in its native environment is a prerequisite for to analyze the higher-order structure of rhodopsin with various illumination conditions. Because CEMOVIS as the method of (first) choice turned out to be too time consuming to manage to analyze different illumination conditions, we tried to find an experimental path which is less time consuming and will lead to structural results earlier and more effectively. Therefore, different techniques were compared – a prerequisite for the analysis of illuminated retinas.

However, before illuminated retinal samples can be examined the first step within this project is to repeat the protocol Gunkel et al. established (Gunkel, 2013 and Gunkel et al., 2015). Here we faced the problem, that the technique of CEMOVIS was less productive and reproducible than expected. Different other techniques were considered, too, from which the most promising was to work with ROS solutions instead of the whole retina. The following sections contain thoughts, hypotheses, and ideas for alternative experi-

mental approaches that arose from throughout analysis of the aforementioned work and its difficulties.

4.2. CEMOVIS is less effective and error-prone

The single steps of CEMOVIS – the vitrification of the retina sample via HPF, the sectioning, and the subsequent processing are all time-consuming techniques. For details, please see chapters 2.9.1 and 2.10 to 2.11.1. Section 3.2 deals with tomograms resulting the classical CEMOVIS protocol. Figure 3.4 shows two tomograms of longitudinally sectioned ROS. One can see at first sight that these are not the perfect tomograms. The ROS was not perfectly cut in the middle. The incisures are at the border of the ROS or inclined and bended. Even one can see some densities in between the disk membranes, the quality was not good enough to compare with the results from Gilliam et al. (2012) or Pöge et al. (2021). The distances between the disks are sometimes reduced. Interdisk distances were reduced to 10 or even 4 nm. The experimental details from Gunkel (2013) were intensively compared and repeated. However, the reason for this reduction could not be identified.

Furthermore, the operator loses a lot of samples on this way – due to improper freezing, sectioning artifacts, or just because of the fact that the sectioned sample is really fragile. Even if a sample could be transferred to the TEM safely, it may not be possible to acquire tomograms. How is that? The fragile carbon film of the EM grids used in this study is supported by the grid bars. Whereas the carbon film appears transparent in the electron beam, the metal grid bars are electron dense and appear as big black areas. If the region of interest is in the vicinity of the grid bar, tilting and imaging is not possible there.

Crinkles of the sections or the film itself must be avoided, as well as fissures or fractures. Otherwise, the sensitive section will be melted or burned. Another consequence of acquiring images in the vicinity of a damaged section area could be that the section or the film will be rolled up and then a bigger area of the section might not be accessible for acquisition, anymore. Furthermore, not every tomogram is suitable for subsequent data analysis. The tomograms were reconstructed using IMOD (Mastronarde, 1997) or Inspect3D (FEI). The samples were labelled with quantum dots (small electron dense particles) to facilitate the alignment of the single projections. This is done during the tracking of fiducials with the corresponding reconstruction software. Shifts between the projections, which are still left after tracking, are removed during the refining step. The amount of quantum dots dispersed on the samples is not always homogeneous or big enough to do automated tracking/refining. These are the reasons why many tomograms got excluded from the data processing step.

The first idea to change the classical CEMOVIS procedure was to acquire dual-axis tomograms. Section 2.11.2 gives insight about the technical aspects of dual-axis tomography, whereas section 3.2.3 treats the results. Whereas thin sections (Figure 3.5a) suffer from poor resolution and contrast, thick sections (Figure 3.5b and c) suffer from sectioning artifacts, which are more pronounced for thick sections. Additionally, sometimes the sections moved during tomogram acquisition. This is because, the attachment of the retinal section was partially suboptimal. We considered the dual-axis tomography as too inaccurate and lengthy procedure. In the evaluation between splitting the dose and a possible gain of resolution, dual-axis tomography is not worth the effort. In fact, in the newer generations of the Titan Krios the dual axis stage is no longer supported. Due to these reasons, dual-axis tomography was considered to be not a good alternative for the classical CEMOVIS, which Gunkel et al. used (Gunkel et al., 2015).

4.3. Using ROS solutions reduces dimensionality

When one tries to accelerate the experimental set-up and speeding the identification of rhodopsin's supramolecular structure, one clearly comes to the point where a reduction of complexity is wanted. If it is almost impossible to gain an effective way to analyse the higher-order structure by tomography of frozen and sectioned retinas in a reasonable time, one clearly considers the only part of the retina which is most interesting for ones aim - the rod outer segment itself. Therefore, retinas got dissected and ROS liberated out of the tissue. ROS solutions had the advantage that they can be vitrified by high-pressure freezing and plunge-freezing, as well. An example of a high-pressure frozen ROS can be found in Figure 3.6. This is a very rare example of a ROS, because the concentration of ROS within the cryo-protectant made the search ROIs within the sections difficult. Several experiments were performed. The ROS concentration was increased, but still the search for ROIs was taking a whole acquisition day. From the tomograms recorded, this was the most promising result. It looks sectioned in cross direction and did not suffer from sectioning artifacts. However, it was burned during tomography and needed to be discarded, as well. Maybe the concentration may be increased in future experiments.

Plunge-frozen cellular solutions may also be thinned via the FIB to gain TEM samples – on which section 4.5 focuses on.

4.4. Freeze-fracture experiments were stopped due to misorientation of ROS

An experiment which also looked promising at the beginning was the freeze-fracture experiment. The aim was to fracture the frozen retina in the area of ROS. The basic idea was that thereby the ROS would break along the disk membranes. Disk membranes

were considered as breaking points. Results are shown in Figure 3.7. It was indeed possible to find the ROS fractured. Nevertheless, the retinas analysed have been bended within the sample carrier and thus every retinal cell layer was visible within the fracture. For the freeze fracture experiments, the retinas were placed into the 100- μm indentation of a sample carrier – closed by another 100- μm indentation carrier. Because of the type of carriers used, a bending effect on the retinas cannot be diminished. This is because of the fact that the retina has a thickness of 218 μm (Sandberg et al., 2005) and was slightly compressed by using two 100- μm indentation sample carriers. One has to additionally take into account that the sample carriers for high-pressure-freezing are not flat, but show a production-related surface indentation (see Figures 3.9 and 3.10). If the surface of the carrier is not perfectly flat, indentations like these grooves can cause tremendous distortions during high-pressure freezing. The surface of HPF specimen support carriers is thus further implicating the flatness of the tissue. Attempts were made to reduce these grooves at the carrier surface. This led to nicely conserved ROS parallel to each other (see Fig. 3.11). However, as ROS looked defect, cytotoxic effects of the revealed copper surfaces were considered. As an application of a gold layer (via sputtering) did not cope with this, experiments with polished sample carriers were stopped.

The intention to proceed with cryo-sectioning or thinning with the use of a FIB of freeze-fractured samples (and subsequent tomography) was not pursued further, as the adequate ROS orientation cannot be guaranteed.

4.5. Impact of ROS sample concentration on FIB-assisted thinning

The technique of thinning vitrified samples for subsequent tomography, established by Engel et al. (2015) and Schaffer et al. (2017), was successfully applied on *Chlamydomonas* chloroplasts and *Rhodobacter sphaeroides*, a phototrophic bacterium. The aim of both

was to visualize and to analyze the native architecture, the morphology of containing chromatophores and vesicular structures carrying out photosynthesis. This alternative technique to gain samples for tomography by combining vitrification and thinning would also be useful to analyze rhodopsin's supramolecular structure. Indeed, first approaches looked promising. The production of TEM specimen via FIB is shown in Figure 3.8.

During thinning of vitrified samples via FIB, we faced the problem that plunge-freezing often led to grids with a broken ice layer or grids, where the ice thickness is very thin and where no particles are enclosed (data not shown). These were discarded. On the other hand, grids with an homogenous cell layer could be obtained, as well. Fig. 3.8 shows exemplarily a production of a lamella for TEM. Here, it was not possible to find ROS in low magnification images due to the thick ice layer. One had to perform coarse milling to find ROIs. As the whole milling procedure for a single position already took 24 hours, the search for ROIs via coarse milling prolongs this preparation time even more. Even though cell concentrations of $5 - 6 \times 10^5 \text{ ROS}/\mu\text{l}$ could be reached via ROS isolation, this concentration may not be sufficient for plunge freezing and subsequent thinning via FIB. It would make sense to follow this route to produce suitable samples in future experiments. Worth trying would be to optimize the ROS concentration and ice thickness.

4.6. Pattern on disk surface detected by AFM

If we reduce the dimensionality of the sample further, we end up with purified ROS disks (see section 2.8). And if we also want to circumvent the obstacles of cryo-sectioning or thinning, we have the possibility to analyze the samples via AFM (see sections 2.16 and 3.3.4). Although we do not do the investigation in a close-to-native state, we found promising results in comparable short time. As Fig. 3.12 demonstrates, we saw a regular

pattern on the surface of the disk membranes - similar to those found by Fotiadis et al. (2003), Liang et al. (2003), and Filipek et al. (2004). It seems reasonable to suppose that this regular pattern is caused by rhodopsin tracks. Further repetitions and investigations are necessary, because this was only a preliminary experiment.

4.7. Tackling the problem of artifacts: possible approaches

A substantial amount of tomograms from longitudinally sectioned retinas showed disk membranes which were locally impaired by artifacts about which an explanation could not be found. A possible angle of attacking this problem would be to compare different preparation temperatures for the dissection of retinas. I dissected and prepared the retina samples at room temperature before solubilization or high pressure freezing (see also chapter 2.5 and 2.6). However, at lower temperatures oligomers may form or are more stabilized and tend less to dissolve. On the other hand, one has to be careful choosing the preparation temperature: working at low temperatures and at high temperatures, both 'extremes' are not optimal for handling retinal or ROS samples because they either cause lipid separation or artificial aggregation of rhodopsin (Koch and Dell'Orco, 2015). Nevertheless, it may be worth to compare samples made at room temperature, at 4°C, and at 37°C.

Also the usage of trypsin during ROS preparation is worth a further investigation. The enzyme trypsin is well known and widely used during passaging of adherent cells within cell culture labs. The function of trypsin is to help removing the adherent cells from cell culture flasks. One could therefore think of not doing the ROS liberation during retina solubilization in an hypotonic manner but with the help of trypsin. The efficiency may be enhanced that way without being too harsh. Oligomers may be kept intact.

artifacts are also observed in biochemical experiments. During experiments where the bleaching of rhodopsin was quantified, one could identify a slight blue shift of the fitted rhodopsin peak. This could be either a real shift caused by some isochromic species of rhodopsin or simply caused by the baseline fitting via PeakFit. However, the raw data can easily be overlaid without any sideways shift of the rhodopsin peak. This indicates that the baseline correction is causing the observed shift. This means further, the artefact of a blue-shifted rhodopsin peak can be neglected. The correction was maintained even though it might slightly shift the rhodopsin peak, because we wanted to fit the raw data with as little interventions as possible in order not to bias the result.

4.7.1. Do we reach the technical limit?

In the following chapter, we will have a look on the technical side of the project and how it impacts gaining results.

The small size of rhodopsin makes it difficult to identify rhodopsin structures within the tomograms. Due to the resolution, rhodopsin cannot be distinguished as monomers. Only higher-order structures would be detectable (personal communication with Dr Al-Amoudi). However, this is very unlikely in raw data. The question arises, how good the data quality must be ideally. To solve this question, a perfect sample was built via simulation (see sections 2.13 and 3.4). A tomogram was created with this “perfect data set” and processed just like the real data. The simulated data set was integrated into and thereby compared to a real data set (see Fig. 3.13). In the next step, the “perfect data set” was noised to look like the real data set to have an idea, how bad the situation in real life is.

The plot profiles from the simulation experiment showed that not every rhodopsin molecule within the tracks could be identified anymore for the noised tomogram (Fig. 3.14). Due to the fact that the noised tomogram was adapted to real data, we

can summarize, indeed, we are at the technical limit.

As we saw in the retrospect, that image quality was not good enough, the problem may not have been the sample, but the acquisition method. When acquiring a tomogram within this study, the stage was tilted from $-60-65^\circ$ to $+60-65^\circ$. As Hagen, Wan, and Briggs (2017) stated the best resolution is gained if the projections at low tilt angles are recorded early within the tilt series. This was not the case for tomograms recorded in this study. In tomograms recorded within this study, a bidirectional tilt-scheme was used (Hagen, Wan, and Briggs, 2017). Furthermore, Hagen et al. presented a dose-symmetric tilt-scheme and the corresponding macro for implementation into SerialEM (Hagen, Wan, and Briggs, 2017). With this tilt scheme the tomogram acquisition starts at 0° and proceeds with a stage tilt to $+3^\circ$, followed by -3° , -6° , $+6^\circ$ and so forth (3° increments; Hagen, Wan, and Briggs (2017)). In addition, the usage of a phase plate, like the Volta phase plate (Danev et al., 2014), may enhance the resolution and thereby image quality further. The *in silico* experiments with the simulated ROS volume could show that the tomogram acquisition of the real cryo-sections was not ideal. The recorded tomograms do not obtain enough information for subsequent data processing and refinement of higher-order structures. If data acquisition delivers better data, investigations of retinal cryo-sections may be worth, again. Using the technique Hagen, Wan, and Briggs (2017) proposed to apply a dose-symmetric tilt-scheme sounds promising. Maybe this acquisition technique would already be the solution to gain a better resolution.

Another EM technique worth thinking about is the array tomography. On conventionally fixed zebrafish samples (Wacker et al., 2015) or *Arabidopsis thaliana* roots sections (Wacker et al., 2016), Wacker et al. performed array tomography to obtain whole cell reconstructions. The authors could successfully create organelle inventories of zebrafish immune cells. The system Atlas 5 Array Tomography platform was applied for these

purposes (Wacker et al., 2015; Wacker et al., 2016). The implementation of the Atlas 5 Array Tomography platform is also possible at the electron microscopy facility used for this study. Recently, there was installed a multibeam scanning electron microscope, with which such analyses on conventionally fixed retinal samples are possible. Günther et al. (2021) could successfully map the cells of the inner and outer plexiform layer, including photoreceptors and bipolar cells, over a square of 140 by 148 μm . The authors could successfully identify double-cones by this method. It could therefore be worth to skip the cryo-approach and the close-to-native-state and step back to conventionally fixed samples (with the risk of artifacts) in order to gain exact reconstructions by addition of multiple tomograms.

4.8. What happens with rhodopsin's higher-order structure upon illumination?

The results obtained via AFM on isolated ROS disk membranes was the most promising technique to accelerate the identification of rhodopsin's higher-order structure compared to CEMOVIS. With this method it would be possible to analyze different illumination conditions. The question arises what might happen with rhodopsins organization once illuminated. The affinity of activated rhodopsin molecules to other rhodopsin molecules might be decreased.

As Gunkel et al. could not detect the supramolecular structure of rhodopsin upon illumination, anymore, one can assume that rhodopsin dissociates out of the well-aligned tracks in slightly illuminated rod disk membranes (Gunkel, 2013).

Figure 4.1 shows our hypotheses for the dissociation of rhodopsin upon illumination. According to our assumption that rhodopsin dissociates out of the well-aligned tracks

in slightly illuminated rod disk membranes one could further speculate that rhodopsin is released as a monomer (b), a dimer (c), or that the whole row (d) in which single bleached rhodopsin molecules were embedded dissociates.

Furthermore this process could be the molecular basis for the translocation of transducin, arrestin, and recoverin upon illumination, Calvert et al. proposed (Calvert et al., 2006).

Using very low light conditions prior to the cryo-preservation, the discovery of the mechanism of light-induced rhodopsin dissociation comes within reach. This assumption is in line with the previous studies performed by Cone in 1972 and Liebman and Entine in 1974 although this is not apparently obvious. Their results support our assumption because Cone, Entine, and Liebman used light in all of those absorption measuring experiments. We think that the higher-order structures of dark-adapted rhodopsin, Gunkel et al. previously identified with CEMOVIS, might already be released at this point of their spectroscopic measurements. Cone, Liebman, and Entine may therefore not have measured absorbances of dark- but light-adapted ROS.

For the dissociation of rhodopsin out of the well-aligned rows and tracks, we hypothesize that either rhodopsin dissociates as a monomer or dimer. We speculate further that the whole row containing the activated rhodopsin molecule falls apart.

What might be the advantage of the dissociation of rhodopsin rows? The illumination-induced dissociation of these rows may have an important role for the redistribution of phototransduction proteins. Calvert et al. reviewed the light-driven translocation of three main factors in phototransduction, transducin, arrestin, and recoverin (Calvert et al., 2006). According to them, redistribution of these factors is driven by diffusion. In the following, we will have a closer look onto these redistributions (Calvert et al., 2006). Upon illumination, transducin translocates from the ROS to the RIS, while arrestin redistributes in the opposite direction. The redistribution of arrestin is reliable

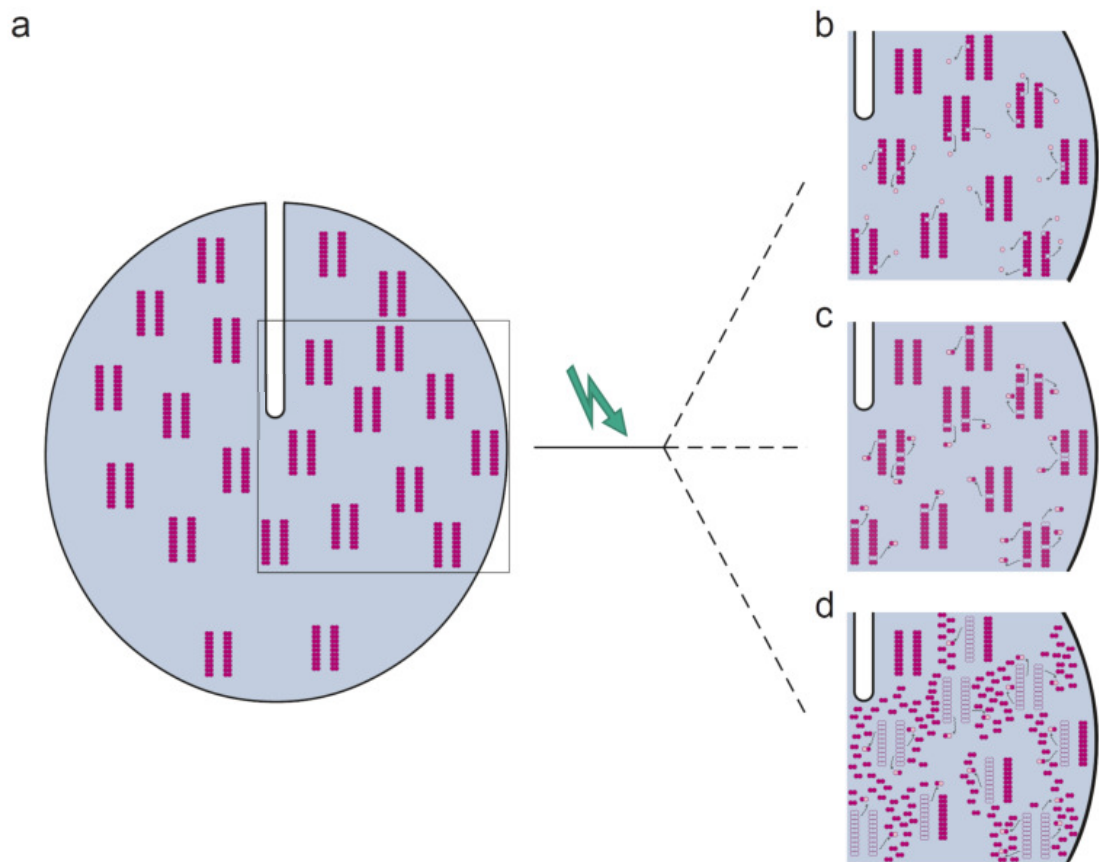


Figure 4.1.: Model of organization of rhodopsin in illuminated retinas

(a) Rhodopsin organization in dark-adapted ROS (Gunkel et al., 2015). Rhodopsin is organized in rows. These rhodopsin rows come in pairs and are aligned parallel to the incisure of the ROS disk. Initial experiments with retinas prepared under ambient light indicate that the organization of rhodopsin, we found in the dark-adapted state, might change tremendously. We, therefore, suggest that the rhodopsin organization is falling apart upon illumination. Rhodopsin could be released from these rows either as monomers (b) or dimers (c) but it is also possible that the whole row, in which at least one rhodopsin molecule was bleached, falls apart (d). Green arrow indicates illumination with green light as described in the chapters 2.6 and 3.1.1 to 3.1.2.

because, after phosphorylation of metarhodopsin II by the rhodopsin kinase, it binds and blocks further transducin activation. The distribution of recoverin which has a role in the regulation of rhodopsin phosphorylation does not change that dramatically. Nevertheless, the dissociation of oligomeric rhodopsin structures may be necessary prior to these redistributions.

4.9. Alternative techniques - worth to be performed

In the following, alternative techniques will be mentioned, with which the identification of the supramolecular architecture of rhodopsin may be facilitated, as well.

4.9.1. Localization of transducin bound to dark-state rhodopsin

In the following section, the possible advantages of the use of antibodies when addressing the question of supramolecular structures of rhodopsin and interactions with downstream signaling molecules in the dark-adapted state are summarized. Antibodies can help to identify proteins. Immunoreactions as used in FRET/BRET experiments make interactions more clear (see also 1.3.1). Immunostaining of cryo samples directly prior to TEM imaging would substantially decrease experimental obstacles. However, Cryo samples are not feasible for immunoaffinity labelling. It is impossible to rinse a cryo sample with an *per se* aqueous solution of antibodies. The cryo sample would be thawed or the antibody no longer intact. It is either not possible to infuse the whole retina with an antibody solution with gaining an effective immunostain. If one wants to make use of antibodies, anyway, one has three options, which I want to detail in the following. First I would like to mention these briefly. First, one can conventionally fix retina samples right at the beginning of the experiment. Secondly, one can leave cryo conditions in between the experiment. Thirdly, one could cryo-fix the immunostained sample.

Conventionally fixed retina samples

With the Correlative Light Electron Microscopy (CLEM) experiment one can detect immunolabels with high resolution with which it would be possible to determine the stoichiometry of the formation of rhodopsin transducin-complexes. Rhodopsin and transducin antibodies would be applied to the dehydrated and fixed retina specimen and detected by addition of gold-labelled secondary antibodies for the subsequent electron microscopy. After a successful initial approach with conventionally fixed retina samples, one can even think of to adapt this experiment for cryo-conditions.

Immunostaining of ROS

Whereas it is not possible to infuse the whole retina with antibodies to immunolabel transducins or other downstream signaling proteins, maybe it is for single cells or cellular compartments. And this is where trypsin solubilized retinas comes in, again. If trypsin solubilization proves to work out, ROS and maybe even ROS disks would be liberated as mentioned in section 4.7. The next step would be to cryo-fix trypsin-solubilized retinas together with anti-rhodopsin antibodies by high-pressure freezing or plunge freezing. This would likely allow to image higher-order complexes of rhodopsin associated with transducins or downstream signaling molecules.

4.9.2. Light microscopy as an upcoming alternative technique

Now, as light microscopy is breaking the border of resolution with newly emerged techniques like mirror-enhanced dSTORM (Heil et al., 2018), light microscopy would also be a possible technique to inspect protein rearrangements at isolated disk membranes. Heil et al. were examining nuclear-pore complexes (NPCs) and CD45 receptors and could further push the resolution limit. They could even reconstruct the full 3D architecture of

microtubular networks. To perform mirror-enhanced dSTORM (also called *meSTORM*), rod disks could be isolated as described in chapter 2.8 and settled on coverslips. To be able to measure specific fluorescence signals, rhodopsin molecules need to be genetically modified or immunolabeled with anti-rhodopsin antibodies after isolation. The localization precision and thereby the high resolution of the NPCs analyzed by Heil et al. , was reached by combining dSTORM, nanocoating (mirror enhancement), and post-processing of fluorescence images (Heil et al., 2018). According to Heil et al. , post-processing involved Fourier ring correlation. The authors could thereby reach localization precision of below 10 nm. As the authors state, for mirror-enhancement, the coverslips need to be coated with a metal-dielectric substrate prior to sample placement. Due to their size, it may not be possible to distinguish single rhodopsin molecules. However, the higher-order structure of rhodopsin – rhodopsin tracks spreading the disk membrane in a well-aligned manner – should be visible by mirror-enhanced dSTORM. Maybe even precoupling with interaction partners would be possible. A basic prerequisite, which would have to be verified first, is that these rhodopsin tracks are not disassembled by the fluorescence microscopy.

4.10. Outlook

As it becomes clear in the detailed discussion of the course and the outcome of this study, there are numerous ways in which further investigations of the higher-order structure of rhodopsin can be directed. Naturally every alternative investigation has its own obstacles, which were discussed in the previous section. Possible future extensions of the experiments include the optimization of the production of TEM samples via FIB-assisted thinning of isolated, plunge-frozen ROS and imaging with either AFM or *meSTORM* - a high-resolution yielding light microscopy technique.

List of Figures

1.1. Inter-disk densities	4
1.2. The visual cycle	6
1.3. Effect of hydroxylamine	7
1.4. Previous studies using Atomic-force microscopy	16
1.5. Dynamic scaffolding mechanism	23
1.6. Model for rhodopsin organization	26
1.7. Model for rhodopsin organization and transducin interactions	27
2.1. Experimental overview	35
2.2. Emission spectra of dissection lamps	36
2.3. Flattened retina as a prerequisite for illumination	39
2.4. LED emission spectrum and rhodopsin absorbance spectrum	43
2.5. Experimental setup for illumination with high-power LED and high-speed timer	44
2.6. Deconvolution and peak separation with PeakFit	46
2.7. Counting of ROS after isolation	47
2.8. Freezing parameters during HPF	50
2.9. Workflow of cryo-electron tomography	58
2.10. Diffraction pattern, <i>missing wedge</i> and <i>missing cone</i> (Lučić, Förster, and Baumeister, 2005)	60
2.11. Generation of rhodopsin tracks and integration into membrane	63

2.12. Generation of simulated tomograms and reconstruction	64
2.13. Schematic illustration of the freeze-fracture	65
2.14. Schematic setup of the FIB	67
2.15. Produktion of TEM samples via thinning via FIB	68
3.1. Different sonification times of dissected retina	73
3.2. Deconvolution and peak identification	75
3.3. Quantification of the rhodopsin bleaching	77
3.4. Example images of tomograms of longitudinal retinal sections	81
3.5. Example images of a dual-axis tomograms	84
3.6. Example image of a putative cross section of HPF ROS	85
3.7. Freeze-fractured retina	87
3.8. Production of FIB lamella	88
3.9. Surface indentations on carrier surface measured with AFM	90
3.10. Negative imprint on high-pressure frozen specimen and distorted ROS .	90
3.11. ROS aligned parallel after polishing of carriers	91
3.12. ROS disks examined with AFM	92
3.13. The simulated tomogram can easily be inserted into a real tomogram . .	92
3.14. Plot profiles of simulated tomogram without and with noise	93
4.1. Model of rhodopsin organization	108

List of Tables

2.1. Software programs used in this study	34
2.2. Content of the phosphate-buffered saline (PBS)	37
2.3. Content of the Ringer's buffer	38
2.4. Illumination times used to quantify the bleaching of rhodopsin	40
2.5. Content of the solubilization buffer	41
2.6. Typical settings for plunge-freezing ROS	51
2.7. Typical settings for plunge-freezing ROS disks	53
2.8. Typical settings for imaging or thinning of ROS samples	68
3.1. Which illumination time corresponds to which bleaching state of rhodopsin?	78
3.2. Overview of tomograms of cross sectioned samples	80

Bibliography

- Adrian, M. et al. (1984). "Cryo-electron microscopy of viruses". In: Nature 308.5954, pp. 32–36. DOI: 10.1038/308032a0.
- Al-Amoudi, A., J. Dubochet, and D. Studer (2002). "Amorphous solid water produced by cryosectioning of crystalline ice at 113 K". In: Journal of Microscopy 207.2, pp. 146–153. DOI: 10.1046/j.1365-2818.2002.01051.x. URL: <http://dx.doi.org/10.1046/j.1365-2818.2002.01051.x>.
- Al-Amoudi, A. and A. S. Frangakis (2013). "Three-dimensional visualization of the molecular architecture of cell-cell junctions in situ by cryo-electron tomography of vitreous sections." eng. In: Methods Mol Biol 961, pp. 97–117. DOI: 10.1007/978-1-62703-227-8_4. URL: http://dx.doi.org/10.1007/978-1-62703-227-8_4.
- Al-Amoudi, A., D. Studer, and J. Dubochet (2005). "Cutting artefacts and cutting process in vitreous sections for cryo-electron microscopy". In: Journal of Structural Biology 150.1, pp. 109–121. DOI: 10.1016/j.jsb.2005.01.003. URL: <http://dx.doi.org/10.1016/j.jsb.2005.01.003>.
- Alves, I. D. et al. (2005). "Phosphatidylethanolamine enhances rhodopsin photoactivation and transducin binding in a solid supported lipid bilayer as determined using plasmon-waveguide resonance spectroscopy". In: Biophys J 88, pp. 198–210. DOI: 10.1529/biophysj.104.046722.

- Bader, C. R., P. R. MacLeish, and E. A. Schwartz (1978). "Responses to light of solitary rod photoreceptors isolated from tiger salamander retina." In: Proceedings of the National Academy of Sciences 75.7, pp. 3507–3511. DOI: 10.1073/pnas.75.7.3507.
- Bartl, F. J., E. Ritter, and K. P. Hofmann (2001). "Signaling States of Rhodopsin: ABSORPTION OF LIGHT IN ACTIVE METARHODOPSIN II GENERATES AN ALL-TRANS-RETINAL BOUND INACTIVE STATE". In: Journal of Biological Chemistry 276.32, pp. 30161–30166. DOI: 10.1074/jbc.m101506200. URL: <https://doi.org/10.1074%2Fjbc.m101506200>.
- Basith, Shaherin et al. (2018). "Exploring G Protein-Coupled Receptors (GPCRs) Ligand Space via Cheminformatics Approaches: Impact on Rational Drug Design". In: Frontiers in Pharmacology 9. DOI: 10.3389/fphar.2018.00128.
- Bayburt, T. H. et al. (2007). "Transducin Activation by Nanoscale Lipid Bilayers Containing One and Two Rhodopsins". In: Journal of Biological Chemistry 282.20, pp. 14875–14881. DOI: 10.1074/jbc.m701433200.
- Bayburt, T. H. et al. (2010). "Monomeric Rhodopsin Is Sufficient for Normal Rhodopsin Kinase (GRK1) Phosphorylation and Arrestin-1 Binding". In: Journal of Biological Chemistry 286.2, pp. 1420–1428. DOI: 10.1074/jbc.m110.151043.
- Becirovic, E. et al. (2014). "Peripherin-2 couples rhodopsin to the CNG channel in outer segments of rod photoreceptors". In: Human Molecular Genetics 23.22, pp. 5989–5997. DOI: 10.1093/hmg/ddu323.
- Berry, J. et al. (2016). "Effect of Rhodopsin Phosphorylation on Dark Adaptation in Mouse Rods". In: Journal of Neuroscience 36.26, pp. 6973–6987. DOI: 10.1523/jneurosci.3544-15.2016. URL: <https://doi.org/10.1523%2Fjneurosci.3544-15.2016>.

-
- Blankenship, E. and D. T. Lodowski (2015). "Rhodopsin Purification from Dark-Adapted Bovine Retina". In: Methods in Molecular Biology. Springer New York, pp. 21–38. DOI: 10.1007/978-1-4939-2330-4_2.
- Bosshart, P. D., A. Engel, and D. Fotiadis (2015). "High-Resolution Atomic Force Microscopy Imaging of Rhodopsin in Rod Outer Segment Disk Membranes". In: Methods in Molecular Biology. Springer New York, pp. 189–203. DOI: 10.1007/978-1-4939-2330-4_13.
- Botelho, A. Vitória et al. (2006). "Curvature and Hydrophobic Forces Drive Oligomerization and Modulate Activity of Rhodopsin in Membranes". In: Biophysical Journal 91.12, pp. 4464–4477. DOI: 10.1529/biophysj.106.082776. URL: <http://dx.doi.org/10.1529/biophysj.106.082776>.
- Buzhynskyy, N., C. Salesse, and S. Scheuring (2011). "Rhodopsin is spatially heterogeneously distributed in rod outer segment disk membranes". In: J Mol Recognit 24, pp. 483–489. DOI: 10.1002/jmr.1086.
- Calvert, P. D. et al. (2006). "Light-driven translocation of signaling proteins in vertebrate photoreceptors". In: Trends Cell Biol 16, pp. 560–568. DOI: 10.1016/j.tcb.2006.09.001.
- Cavusoglu, Nukhet et al. (2003). "Differential proteomic analysis of the mouse retina: the induction of crystallin proteins by retinal degeneration in the rd1 mouse". In: Molecular & Cellular Proteomics 2.8, pp. 494–505.
- Chabre, M. and J. Breton (1979). "The Orientation of the Chromophore of Vertebrate Rhodopsin in the "Meta" Intermediate States and the Reversibility of the Meta II-Meta III Transition". In: Vision Research. DOI: 10.1016/0042-6989(79)90226-8.
- Chabre, M. and M. le Maire (2005). "Monomeric G-protein-coupled receptor as a functional unit". In: Biochemistry 44, pp. 9395–9403. DOI: 10.1021/bi050720o.

- Chen, Qiuyan et al. (July 2021). "Structures of rhodopsin in complex with G-protein-coupled receptor kinase 1." In: Nature 595 (7868), pp. 600–605. ISSN: 1476-4687. DOI: 10.1038/s41586-021-03721-x.
- Comar, W. D. et al. (2014). "Time-Resolved Fluorescence Spectroscopy Measures Clustering and Mobility of a G Protein-Coupled Receptor Opsin in Live Cell Membranes". In: Journal of the American Chemical Society 136.23, pp. 8342–8349. DOI: 10.1021/ja501948w.
- Cone, R. A. (1972). "Rotational diffusion of rhodopsin in the visual receptor membrane". In: Nat New Biol 236, pp. 39–43. DOI: 10.1038/newbio236039a0.
- Daibani, Amal El and Tao Che (2021). "Nanobodies as sensors of GPCR activation and signaling". In: Biomolecular Interactions Part A. Elsevier, pp. 161–177. DOI: 10.1016/bs.mcb.2021.06.008.
- Danev, Radostin et al. (2014). "Volta potential phase plate for in-focus phase contrast transmission electron microscopy". In: Proceedings of the National Academy of Sciences 111.44, pp. 15635–15640. DOI: 10.1073/pnas.1418377111.
- Davenport, Anthony P. et al. (2013). "International Union of Basic and Clinical Pharmacology. LXXXVIII. G Protein-Coupled Receptor List: Recommendations for New Pairings with Cognate Ligands". In: Pharmacological Reviews 65.3. Ed. by Eliot H. Ohlstein, pp. 967–986. DOI: 10.1124/pr.112.007179.
- De Lean, A., J. M. Stadel, and R. J. Lefkowitz (1980). "A Ternary Complex Model Explains the Agonist-specific Binding Properties of the Adenylate Cyclase-coupled β -Adrenergic Receptor". In: J Biol Chem 255, pp. 7108–7117.
- Dell'Orco, D. and K. W. Koch (2011). "A dynamic scaffolding mechanism for rhodopsin and transducin interaction in vertebrate vision The Induction of Crystallin Proteins by Retinal Degeneration in the rd1 Mouse*". In: Biochem J 440, pp. 263–271. DOI: 10.1042/BJ20110871.

- Downer, N. W. (1985). "Cross-linking of dark-adapted frog photoreceptor disk membranes. Evidence for monomeric rhodopsin". In: Biophysical Journal 47.3, pp. 285–293. DOI: 10.1016/s0006-3495(85)83918-7.
- Dubochet, J. et al. (1988). "Cryo-electron microscopy of vitrified specimens." eng. In: Q Rev Biophys 21.2, pp. 129–228. DOI: 10.1017/S0033583500004297.
- Edrington, T. C., M. Bennett, and A. D. Albert (2008). "Calorimetric Studies of Bovine Rod Outer Segment Disk Membranes Support a Monomeric Unit for Both Rhodopsin and Opsin". In: Biophysical Journal 95.6, pp. 2859–2866. DOI: 10.1529/biophysj.108.128868.
- Eidne, K. A., K. M. Kroeger, and A. C. Hanyaloglu (2002). "Applications of novel resonance energy transfer techniques to study dynamic hormone receptor interactions in living cells". In: Trends Endocrinol Metab 13, pp. 415–421. DOI: 10.1016/S1043-2760(02)00669-0.
- Engel, Benjamin D et al. (2015). "Native architecture of the Chlamydomonas chloroplast revealed by in situ cryo-electron tomography". In: eLife 4. DOI: 10.7554/elife.04889.
- Eps, Ned Van et al. (2017). "Conformational equilibria of light-activated rhodopsin in nanodiscs". In: Proceedings of the National Academy of Sciences 114.16, E3268–E3275. DOI: 10.1073/pnas.1620405114.
- Ernst, O. P. and F. J. Bartl (2002). "Active States of Rhodopsin". In: ChemBioChem 3.10, pp. 968–974. DOI: 10.1002/1439-7633(20021004)3:10<968::AID-CBIC968>3.0.CO;2-Q.
- Ernst, O. P. et al. (2007). "Monomeric G protein-coupled receptor rhodopsin in solution activates its G protein transducin at the diffusion limit". In: Proceedings of the National Academy of Sciences 104.26, pp. 10859–10864. DOI: 10.1073/pnas.0701967104.

- Ernst, O. P. et al. (2014). "Microbial and Animal Rhodopsins: Structures, Functions, and Molecular Mechanisms". In: Chemical Reviews 114.1, pp. 126–163. DOI: 10.1021/cr4003769. URL: <https://doi.org/10.1021%2Fcr4003769>.
- Filipek, S. et al. (2004). "A concept for G protein activation by G protein-coupled receptor dimers: the transducin/rhodopsin interface". In: Photochemical & Photobiological Sciences 3.6, p. 628. DOI: 10.1039/b315661c.
- Fong, S.-L. et al. (1982). "Detergents for Extraction of Visual Pigments: Types, Solubilization, and Stability". In: Methods in Enzymology, pp. 133–140. DOI: 10.1016/S0076-6879(82)81022-7.
- Fotiadis, D. et al. (2003). "Atomic-force microscopy: Rhodopsin dimers in native disc membranes". In: Nature 421, pp. 127–128. DOI: 10.1038/421127a..
- Fredriksson, R. et al. (2003). "Seven evolutionarily conserved human rhodopsin G protein-coupled receptors lacking close relatives". In: FEBS Lett 554, pp. 381–388. DOI: 10.1016/s0014-5793(03)01196-7.
- Gales, C. et al. (2006). "Probing the activation-promoted structural rearrangements in preassembled receptor-G protein complexes". In: Nat Struct Mol Biol 13, pp. 778–786.
- Gao, Yang et al. (2019). "Structures of the Rhodopsin-Transducin Complex: Insights into G-Protein Activation". In: Molecular Cell 75.4, 781–790.e3. DOI: 10.1016/j.molcel.2019.06.007.
- Gilliam, J. C. et al. (2012). "Three-dimensional architecture of the rod sensory cilium and its disruption in retinal neurodegeneration". In: Cell 151, pp. 1029–1041.
- Govardovskii, V. I. et al. (2009). "Lateral diffusion of rhodopsin in photoreceptor membrane: a reappraisal". In: Mol Vis 15, pp. 1717–1729.
- Grip, W. J. De, F. J. M. Daemen, and S. L. Bonting (1980). "Isolation and Purification of Bovine Rhodopsin". In: Methods in Enzymology. DOI: 10.1016/S0076-6879(80)67038-4.

-
- Gu, Y. Z. and A. Schonbrunn (1997). "Coupling specificity between somatostatin receptor sst2A and G proteins: isolation of the receptor-G protein complex with a receptor antibody". In: Mol Endocrinol 11, pp. 527–537.
- Gunkel, M. (2013). "Supramolecular architecture of intact mouse photoreceptors and sea urchin flagella". PhD thesis. Dissertation: Rheinische Friedrich-Wilhelms-Universität Bonn.
- Gunkel, M. et al. (2015). "Higher-Order Architecture of Rhodopsin in Intact Photoreceptors and Its Implication for Phototransduction Kinetics". In: Structure 23.4, pp. 628–638. DOI: 10.1016/j.str.2015.01.015. URL: <http://dx.doi.org/10.1016/j.str.2015.01.015>.
- Günther, Anja et al. (2021). "Double Cones and the Diverse Connectivity of Photoreceptors and Bipolar Cells in an Avian Retina". In: The Journal of Neuroscience 41.23, pp. 5015–5028. DOI: 10.1523/jneurosci.2495-20.2021.
- Hagen, Wim J.H., William Wan, and John A.G. Briggs (2017). "Implementation of a cryo-electron tomography tilt-scheme optimized for high resolution subtomogram averaging". In: Journal of Structural Biology 197.2, pp. 191–198. DOI: 10.1016/j.jsb.2016.06.007.
- Heil, H. S. et al. (2018). "Sharpening emitter localization in front of a tuned mirror". In: Light: Science & Applications 7.1. DOI: 10.1038/s41377-018-0104-z.
- Hein, P. and M. Bünemann (2009). "Coupling mode of receptors and G proteins". In: Naunyn Schmiedebergs Arch Pharmacol 379, pp. 435–443.
- Hermanson, G. T. (July 25, 2013). Bioconjugate Techniques. Elsevier Science. 1200 Seiten. URL: http://www.ebook.de/de/product/21128120/greg_t_hermanson_bioconjugate_techniques.html.
- Hubbell, W. L. (1975). "Characterization of rhodopsin in synthetic systems". In: Accounts of Chemical Research 8.3, pp. 85–91. DOI: 10.1021/ar50087a002.

- Ianoul, A. et al. (2005). "Imaging nanometer domains of β -adrenergic receptor complexes on the surface of cardiac myocytes". In: Nature Chemical Biology 1.4, pp. 196–202. DOI: 10.1038/nchembio726. URL: <http://dx.doi.org/10.1038/nchembio726>.
- Jaqaman, K. et al. (2011). "Cytoskeletal control of CD36 diffusion promotes its receptor and signaling function". In: Cell 146, pp. 593–606.
- Jastrzebska, B. et al. (2004). "Functional Characterization of Rhodopsin Monomers and Dimers in Detergents". In: J Biol Chem 279.52, 54663–54675.
- Jastrzebska, B. et al. (2006). "Functional and structural characterization of rhodopsin oligomers". In: J Biol Chem 281, pp. 11917–11922.
- Jastrzebska, B. et al. (2015). "Disruption of Rhodopsin Dimerization with Synthetic Peptides Targeting an Interaction Interface". In: Journal of Biological Chemistry 290.42, pp. 25728–25744. DOI: 10.1074/jbc.m115.662684.
- Katayama, K., Y. Furutani, and H. Kandori (2010). "FTIR Study of the Photoreaction of Bovine Rhodopsin in the Presence of Hydroxylamine". In: The Journal of Physical Chemistry B 114.27, pp. 9039–9046. DOI: 10.1021/jp102288c. URL: <https://doi.org/10.1021%2Fjp102288c>.
- Knowles, F. C., M. J. McDonald, and Q. H. Gibson (1975). "The Origin of the Adams-Schuster Difference Spectrum of Oxyhemoglobin". In: Biochemical and Biophysical Research Communications 66.2, pp. 556–563.
- Koch, K.-W. and D. Dell'Orco (2015). "Protein and Signaling Networks in Vertebrate Photoreceptor Cells". In: Frontiers in Molecular Neuroscience 8. DOI: 10.3389/fnmol.2015.00067.
- Kota, P. et al. (2006). "Opsin is present as dimers in COS1 cells: Identification of amino acids at the dimeric interface". In: Proceedings of the National Academy of Sciences 103.9, pp. 3054–3059. DOI: 10.1073/pnas.0510982103.
- Kumar, Sandeep et al. (2018). "Disruption of Rhodopsin Dimerization in Mouse Rod Photoreceptors by Synthetic Peptides Targeting Dimer Interface". In:

-
- Methods in Molecular Biology*. Springer New York, pp. 115–128. DOI: 10.1007/978-1-4939-7720-8_8.
- Lachance, M. et al. (1999). “Stable association of G proteins with β_2 AR is independent of the state of receptor activation”. In: *Cell Signal* 11, pp. 523–533.
- Liang, Y. et al. (2003). “Organization of the G Protein-coupled Receptors Rhodopsin and Opsin in Native Membranes”. In: *Journal of Biological Chemistry* 278.24, pp. 21655–21662. DOI: 10.1074/jbc.m302536200.
- Liang, Yan et al. (2004). “Rhodopsin Signaling and Organization in Heterozygote Rhodopsin Knockout Mice”. In: *Journal of Biological Chemistry* 279.46, pp. 48189–48196. DOI: 10.1074/jbc.m408362200.
- Liebman, P. A. and G. Entine (1974). “Lateral diffusion of visual pigment in photoreceptor disk membranes”. In: *Science* 185, pp. 457–459.
- Lučić, V., F. Förster, and W. Baumeister (2005). “STRUCTURAL STUDIES BY ELECTRON TOMOGRAPHY: From Cells to Molecules”. In: *Annual Review of Biochemistry* 74.1, pp. 833–865. DOI: 10.1146/annurev.biochem.73.011303.074112. URL: <https://doi.org/10.1146%2Fannurev.biochem.73.011303.074112>.
- Lučić, V., A. Rigort, and W. Baumeister (2013). “Cryo-electron tomography: The challenge of doing structural biology in situ”. In: *J Cell Biol* 202.3, pp. 407–419. DOI: 10.1083/jcb.201304193. URL: <http://dx.doi.org/10.1083/jcb.201304193>.
- Mallory, D. Paul et al. (2018). “The Retinitis Pigmentosa-Linked Mutations in Transmembrane Helix 5 of Rhodopsin Disrupt Cellular Trafficking Regardless of Oligomerization State”. In: *Biochemistry* 57.35, pp. 5188–5201. DOI: 10.1021/acs.biochem.8b00403.
- Masich, S. et al. (2006). “A procedure to deposit fiducial markers on vitreous cryosections for cellular tomography”. In: *Journal of Structural Biology* 156.3, pp. 461–468. DOI: 10.1016/j.jsb.2006.05.010. URL: <http://dx.doi.org/10.1016/j.jsb.2006.05.010>.

- Mastrorarde, D. N. (1997). "Dual-Axis Tomography: An Approach with Alignment Methods That Preserve Resolution". In: Journal of Structural Biology 120.3, pp. 343–352. DOI: 10.1006/jsbi.1997.3919. URL: <http://dx.doi.org/10.1006/jsbi.1997.3919>.
- (2005). "Automated electron microscope tomography using robust prediction of specimen movements". In: Journal of Structural Biology 152.1, pp. 36–51. DOI: 10.1016/j.jsb.2005.07.007. URL: <http://dx.doi.org/10.1016/j.jsb.2005.07.007>.
- Maurel, D. et al. (2008). "Cell-surface protein-protein interaction analysis with time-resolved FRET and snap-tag technologies: application to GPCR oligomerization". In: Nat Methods 5, pp. 561–567.
- McDowall, A. W. et al. (1983). "Electron microscopy of frozen hydrated sections of vitreous ice and vitrified biological samples". In: Journal of microscopy 131.1, pp. 1–9.
- McMullan, G. et al. (2014). "Comparison of optimal performance at 300keV of three direct electron detectors for use in low dose electron microscopy". In: Ultramicroscopy 147, pp. 156–163. DOI: 10.1016/j.ultramic.2014.08.002. URL: <https://doi.org/10.1016%2Fj.ultramic.2014.08.002>.
- Medina, R., D. Perdomo, and J. Bubis (2004). "The Hydrodynamic Properties of Dark- and Light-activated States of n-Dodecyl β -D-Maltoside-solubilized Bovine Rhodopsin Support the Dimeric Structure of Both Conformations". In: Journal of Biological Chemistry 279.38, pp. 39565–39573. DOI: 10.1074/jbc.M402446200.
- Meyer, Rüdiger R. and Angus Kirkland (1998). "The effects of electron and photon scattering on signal and noise transfer properties of scintillators in CCD cameras used for electron detection". In: Ultramicroscopy 75.1, pp. 23–33. DOI: 10.1016/S0304-3991(98)00051-5.

-
- Mishra, Ashish K. et al. (2016). "Quaternary structures of opsin in live cells revealed by FRET spectrometry". In: Biochemical Journal 473.21, pp. 3819–3836. DOI: 10.1042/bcj20160422.
- Mitchell, D. R. G. and B. Schaffer (2005). "Scripting-customised microscopy tools for Digital Micrograph™". In: Ultramicroscopy 103.4, pp. 319–332. DOI: 10.1016/j.ultramicro.2005.02.003. URL: <https://doi.org/10.1016%2Fj.ultramicro.2005.02.003>.
- Moor, H. and M. Hoehli (1970). "The influence of high-pressure freezing on living cells". In: Microscopie électronique, pp. 445–446.
- Moor, H. and K. Mühlethaler (1963). "FINE STRUCTURE IN FROZEN-ETCHED YEAST CELLS." eng. In: J Cell Biol 17.3, pp. 609–628.
- Moor, H. et al. (1980). "The influence of high pressure freezing on mammalian nerve tissue." eng. In: Cell Tissue Res 209.2, pp. 201–216.
- Müller, B. K. et al. (2005). "Pulsed Interleaved Excitation". In: Biophysical Journal 89.5, pp. 3508–3522. DOI: 10.1529/biophysj.105.064766.
- Muller, D. J. (2008). "AFM: A Nanotool in Membrane Biology". In: Biochemistry 47.31, pp. 7986–7998. DOI: 10.1021/bi800753x.
- Nickell, S. et al. (2007). "Three-dimensional architecture of murine rod outer segments determined by cryoelectron tomography". In: J Cell Biol 177, pp. 917–925.
- Noble, J. M. et al. (2018). "Connectivity of centermost chromatophores in *Rhodospira rubra* bacteria". In: Molecular Microbiology 109.6, pp. 812–825. DOI: 10.1111/mmi.14077.
- Okada, T. et al. (2004). Crystal Structure of Bovine Rhodopsin at 2.2 Angstroms Resolution. DOI: 10.2210/pdb1u19/pdb.
- Oldham, W. M. and H. E. Hamm (2008). "Heterotrimeric G protein activation by G-protein-coupled receptors". In: Nature Reviews Molecular Cell Biology 9.1, pp. 60–71. DOI: 10.1038/nrm2299.

- Palczewski, K. (2006). "G protein-coupled receptor rhodopsin". In: Annu Rev Biochem 75, pp. 743–767.
- Palczewski, K. et al. (2000). "Crystal structure of rhodopsin: A G protein-coupled receptor". In: Science 289, pp. 739–745.
- Pettersen, Eric F. et al. (2004). "UCSF Chimera?A visualization system for exploratory research and analysis". In: Journal of Computational Chemistry 25.13, pp. 1605–1612. DOI: 10.1002/jcc.20084.
- Pöge, Matthias et al. (2021). "Determinants shaping the nanoscale architecture of the mouse rod outer segment". In: eLife 10. DOI: 10.7554/elife.72817.
- Poincelot, R. P. et al. (1970). "Determination of the Chromophoric Binding Site in Native Bovine Rhodopsin". In: Biochemistry 9.8, pp. 1809–1816.
- Poo, M. and R. A. Cone (1974). "Lateral diffusion of rhodopsin in the photoreceptor membrane". In: Nature 247, pp. 438–441.
- Pugh, E. N. and T. D. Lamb (2000). "Chapter 5 Phototransduction in vertebrate rods and cones: Molecular mechanisms of amplification, recovery and light adaptation". In: Handbook of Biological Physics. Elsevier, pp. 183–255. DOI: 10.1016/s1383-8121(00)80008-1.
- Rakshit, Tatini and Paul S.-H. Park (2015). "Impact of Reduced Rhodopsin Expression on the Structure of Rod Outer Segment Disc Membranes". In: Biochemistry 54.18, pp. 2885–2894. DOI: 10.1021/acs.biochem.5b00003.
- Ramirez, Samuel A. and Chad Leidy (2018). "Effect of the Organization of Rhodopsin on the Association between Transducin and a Photoactivated Receptor". In: The Journal of Physical Chemistry B 122.38, pp. 8872–8879. DOI: 10.1021/acs.jpcc.8b07401.
- Ramon, E. et al. (2003). "Effect of dodecyl maltoside detergent on rhodopsin stability and function". In: Vision Research 43.28, pp. 3055–3061. DOI: 10.1016/j.visres.2003.08.009. URL: <https://doi.org/10.1016%2Fj.visres.2003.08.009>.

-
- Rando, R. R. (1996). "Polyenes and vision". In: Chemistry & Biology 3.4, pp. 255–262.
- Rasmussen, S. G. et al. (2011). "Crystal structure of the β_2 adrenergic receptor-Gs protein complex". In: Nature 477, pp. 549–555.
- Rigort, A. et al. (2012). "Integrative Approaches for Cellular Cryo-electron Tomography: Correlative Imaging and Focused Ion Beam Micromachining". In: Methods in cell biology 111, p. 259.
- Ritchie, Ken et al. (2003). "The fence and picket structure of the plasma membrane of live cells as revealed by single molecule techniques". In: Molecular membrane biology 20.1, pp. 13–18.
- RN Lolley RH Lee, DG Chase and E Racz (Mar. 1986). "Rod photoreceptor cells dissociated from mature mice retinas." In: Investigative Ophthalmology & Visual Science 27.3.
- Roof, D. J. and J. E. Heuser (1982). "Surfaces of rod photoreceptor disk membranes: integral membrane components." eng. In: J Cell Biol 95.2 Pt 1, pp. 487–500.
- Rullgård, H. et al. (2011). "Simulation of transmission electron microscope images of biological specimens". In: Journal of Microscopy 243.3, pp. 234–256. DOI: 10.1111/j.1365-2818.2011.03497.x.
- Ruska, E. (1934). "Über Fortschritte im Bau und in der Leistung des magnetischen Elektronenmikroskops". In: Zeitschrift für Physik A Hadrons and Nuclei 87.9, pp. 580–602.
- Sandberg, Michael A. et al. (2005). "The Association between Visual Acuity and Central Retinal Thickness in Retinitis Pigmentosa". In: Investigative Ophthalmology & Visual Science 46.9, p. 3349. DOI: 10.1167/iovs.04-1383.
- Sander, Christopher L. et al. (2022). "Structural evidence for visual arrestin priming via complexation of phosphoinositols". In: Structure 30.2, 263–277.e5. DOI: 10.1016/j.str.2021.10.002.

- Sartori, N., K. Richter, and J. Dubochet (1993). "Vitrification depth can be increased more than 10-fold by high-pressure freezing". In: Journal of microscopy 172.1, pp. 55–61.
- Schaffer, M. et al. (2017). "Optimized cryo-focused ion beam sample preparation aimed at in situ structural studies of membrane proteins". In: Journal of Structural Biology 197.2, pp. 73–82. DOI: 10.1016/j.jsb.2016.07.010.
- Sechrest, Emily R. et al. (2020). "Loss of PRCD alters number and packaging density of rhodopsin in rod photoreceptor disc membranes". In: Scientific Reports 10.1. DOI: 10.1038/s41598-020-74628-2.
- Seddon, A. M., P. Curnow, and P. J. Booth (2004). "Membrane proteins, lipids and detergents: not just a soap opera". In: Biochimica et Biophysica Acta (BBA) - Biomembranes 1666.1-2, pp. 105–117. DOI: 10.1016/j.bbamem.2004.04.011. URL: <https://doi.org/10.1016%2Fj.bbamem.2004.04.011>.
- Senapati, Subhadip and Paul S.-H. Park (2018). "Investigating the Nanodomain Organization of Rhodopsin in Native Membranes by Atomic Force Microscopy". In: Methods in Molecular Biology. Springer New York, pp. 61–74. DOI: 10.1007/978-1-4939-8894-5_4.
- Senapati, Subhadip et al. (2018). "Effect of dietary docosahexaenoic acid on rhodopsin content and packing in photoreceptor cell membranes". In: Biochimica et Biophysica Acta (BBA) - Biomembranes 1860.6, pp. 1403–1413. DOI: 10.1016/j.bbamem.2018.03.030.
- Senapati, Subhadip et al. (2019). "Differentiating between Inactive and Active States of Rhodopsin by Atomic Force Microscopy in Native Membranes". In: Analytical Chemistry 91.11, pp. 7226–7235. DOI: 10.1021/acs.analchem.9b00546.

-
- Severs, N. J. (2007). "Freeze-fracture electron microscopy". In: Nat Protoc 2.3, pp. 547–576. DOI: 10.1038/nprot.2007.55. URL: <http://dx.doi.org/10.1038/nprot.2007.55>.
- Steere, R. L. (1957). "Electron microscopy of structural detail in frozen biological specimens." eng. In: J Biophys Biochem Cytol 3.1, pp. 45–60.
- Studer, D., M. Michel, and M. Müller (1989). "High pressure freezing comes of age." eng. In: Scanning Microsc Suppl 3, 253–68; discussion 268–9.
- Suda et al. (2004). "The supramolecular structure of the GPCR rhodopsin in solution and native disc membranes". In: Molecular Aspects of Medicine Membrane Biology 21.6, 435–446.
- Tang, Guang et al. (Jan. 2007). "EMAN2: an extensible image processing suite for electron microscopy." In: Journal of structural biology 157 (1), pp. 38–46. ISSN: 1047-8477. DOI: 10.1016/j.jsb.2006.05.009. ppublish.
- Wacker, I. et al. (2015). "Array tomography: characterizing FAC-sorted populations of zebrafish immune cells by their 3D ultrastructure". In: Journal of Microscopy 259.2, pp. 105–113. DOI: 10.1111/jmi.12223.
- Wacker, Irene et al. (2016). "Hierarchical imaging: a new concept for targeted imaging of large volumes from cells to tissues". In: BMC Cell Biology 17.1. DOI: 10.1186/s12860-016-0122-8.
- Wald, G. and P. K. Brown (1953). "The molar extinction of rhodopsin". In: The Journal of general physiology 37.2, pp. 189–200.
- Whited, A. M. and P. S.-H. Park (2015). "Nanodomain organization of rhodopsin in native human and murine rod outer segment disc membranes". In: Biochimica et Biophysica Acta (BBA) - Biomembranes 1848.1, pp. 26–34. DOI: 10.1016/j.bbamem.2014.10.007.

Yang, Dehua et al. (Jan. 2021). "G protein-coupled receptors: structure- and function-based drug discovery." In: Signal transduction and targeted therapy 6 (1), p. 7. ISSN: 2059-3635. DOI: 10.1038/s41392-020-00435-w.

Zhao, Dorothy Yanling et al. (2019). "Cryo-EM structure of the native rhodopsin dimer in nanodiscs". In: Journal of Biological Chemistry 294.39, pp. 14215–14230. DOI: 10.1074/jbc.ra119.010089.

A. Danksagung

Herrn Prof. Dr. Elmar Behrmann danke ich für die Übernahme des Erstgutachtens und für wertvolle Unterstützung, insbesondere in den letzten Monaten. Mein Dank geht an Frau Prof. Dr. Stephanie Kath-Schorr für die Übernahme des Vorsitzes der Prüfungskommission und Herrn Prof. Dr. Ulrich Baumann für die Erstellung des Zweitgutachtens. Ein besonderer Dank geht auch an Herrn Dr. Stephan Irsen für die unermüdliche Hilfe im Rahmen der Elektronenmikroskopie und allen sonstigen Belangen. Herrn Dr. Ashraf Al-Amoudi und seinem Team (Frau Dr. Sandra Knabe, Herrn Dr. Olivier Le-Bihan, Herrn Dr. Weaam Alkhaldi) danke ich für den regelmäßigen Austausch. Mein Dank gilt Herrn Prof. Dr. Guido Lüchters für die Hilfe bei der Statistik. Dr. H. Körschen, Frau Anna Bücker, Herrn Norbert Brenner und Herrn Dr. René Pascal möchte ich für die Unterstützung im Labor und Frau Heike Krause für die administrative Unterstützung danken. Für kollegiales Zusammensein danke ich Frau Dr. Sophie Schonauer, Frau Dr. Domenica Farci, Frau Dr. Zhiyang Tan, Frau Dr. Anja Günther, Frau Dr. Annukka Aho-Ritter, Frau Dr. Astrid Müller und Frau Dr. Melanie Balbach.

Meiner Familie danke ich von ganzem Herzen für die immerwährende Unterstützung ohne die die Fertigstellung dieser Arbeit nicht möglich gewesen wäre.

B. Eidesstattliche Erklärung

Ich versichere, dass ich die von mir vorgelegte Dissertation selbständig angefertigt, die benutzten Quellen und Hilfsmittel vollständig angegeben und die Stellen der Arbeit – einschließlich Tabellen, Karten und Abbildungen –, die anderen Werken im Wortlaut oder dem Sinn nach entnommen sind, in jedem Einzelfall als Entlehnung kenntlich gemacht habe; dass diese Dissertation noch keiner anderen Fakultät oder Universität zur Prüfung vorgelegen hat; dass sie – abgesehen von unten angegebenen Teilpublikationen – noch nicht veröffentlicht worden ist sowie, dass ich eine solche Veröffentlichung vor Abschluss des Promotionsverfahrens nicht vornehmen werde. Die Bestimmungen der Promotionsordnung sind mir bekannt. Die von mir vorgelegte Dissertation ist von Prof. U. B. Kaupp betreut worden.

Signed:



Date:

06.03.2022

C. Curriculum Vitae

Name: Anne Viktoria Schulze
Date of birth: 06.07.1985
Place of birth: Berlin
Nationality: German

Education and Training

Name of Institution	Degree / Date conferred	Area of Study
Dr. Notghi Academy	Jan 2019	Clinical Research & Vigilance
Freie Universität Berlin	Dipl. Biochem. / Aug 2012	Biochemistry
Apprenticeship Biological technical assistant	Jun 2007	Biology

Professional Experience

Position	Institution	Dates
Study coordinator	Helios Health Institute GmbH (formerly Berlin Cancer Institute GmbH)	since Mar 2019
Guest scientist	Center of advanced european studies and research (caesar Bonn)	Jul 2017 – Dec 2019
PhD student	Center of advanced european studies and research (caesar Bonn)	Jan 2013 – Jun 2017
Scientist	Humboldt Universität zu Berlin	Oct 2012 – Nov 2012
Student assistant	Humboldt Universität zu Berlin	Oct 2010 – Sep 2012
Biological technical assistant	Max Delbrück Center for Molecular Medicine Berlin	Jun 2007 – Sep 2007

Anne Schulze

Berlin, 06.03.2022